UNIVERSITY OF CALGARY

A Theoretical Framework for Seismic Time-lapse Difference AVO Analysis with Validation on Physical Modelling and Field Data

by

Shahin Jabbari

A THESIS

SUBMITTED TO THE FACULTY OF GRADUATE STUDIES

IN PARTIAL FULFILLMENT OF THE REQUIREMENTS FOR THE

DEGREE OF DOCTOR OF PHILOSOPHY

DEPARTMENT OF GEOSCIENCE

CALGARY, ALBERTA

April, 2016

UNIVERSITY OF CALGARY

FACULTY OF GRADUATE STUDIES

The undersigned certify that they have read, and recommend to the Faculty of Graduate Studies for acceptance, a thesis entitled "A Theoretical Framework for Seismic Time-lapse Difference AVO Analysis with Validation on Physical Modelling and Field Data" submitted by Shahin Jabbari in partial fulfillment of the requirements for the degree of DOCTOR OF PHILOSOPHY.

Supervisor, Dr Kristopher A. Innanen
Department of Geoscience

Dr Edward Stephen Krebes
Department of Geoscience

Dr Laurence R Lines
Department of Geoscience

Dr Michael Wieser
Department of Physics and Astronomy

External Examiner , Dr Alison E. Malcolm
Department of Earth Sciences
Memorial University of Newfoundland

Date

Abstract

Perturbation theory has been used widely in many applications in seismology, more recently for time-lapse studies. Time-lapse studies are cost-effective approaches for monitoring changes in a reservoir due to production or enhanced oil recovery techniques to restore formation pressure and improve the fluid flow over a period of time in a reservoir. By monitoring these changes, time-lapse studies facilitate management of a reservoir and extend the useful life of an oilfield.

Perturbation or, scattering theory is used as a framework to model these difference data in a time lapse study. The baseline survey (before changes) is set as a background medium which undergoes a range of perturbations by the time of the monitor survey (after changes). The study in this thesis focuses on applying the perturbation theory in time-lapse problems to describe the difference data from a baseline survey to a monitor survey in a reservoir. Changes in the pressure or fluid saturation in a reservoir cause changes in seismic parameters such as P-wave and S- wave velocities and density. These changes give rise to difference data between the baseline survey data and monitor survey data. The perturbation quantifies the changes in P-wave and S-wave velocity and density from the time of the baseline relative to the time of the monitor survey.

Time-lapse amplitude variation with offset (AVO) methods are applied to analyze changes in the seismic parameters. A scheme for modelling linear and nonlinear elastic time-lapse difference AVO data for P-P sections (an incident P-wave with reflected P-wave) is formulated. This framework is expressed as perturbation in P-wave and S-wave velocities and density. The perturbations in these parameters are defined such that they can account for the changes in the baseline survey for the wave entering from the cap rock (layer above the reservoir) into the reservoir, and the time-lapse changes in the reservoir. The difference data then, are described as an expansion in orders of both baseline interface properties and

time-lapse changes from the time of the baseline survey to the time of the monitor survey. I have also examined this formulation with the numerical data used in the literature for real time-lapse data. To first order the framework for time-lapse difference data is in agreement with Landrø's linear approximation. The higher order terms represent corrections appropriate for large P-wave and S-wave velocity and density contrasts in the reservoir from the time of the baseline survey to the time of the monitor survey. This framework is then expanded to describe the difference data for shear waves and converted waves.

A physical modeling data set is acquired, simulating a time-lapse problem, to validate the theoretical results for P-P data. Physical modelling of geophysical data provides physical property distributions of the Earth which are invariably simpler than the real Earth, and the degree of simplification depends upon the geometry used for the data acquisition. 3D seismic surveys resembling the baseline and monitor surveys are modeled with The University of Calgary Seismic Physical Modelling Facility. Plexiglas, Polyvinyl chloride (PVC), and phenolic slabs are used as proxy materials to simulate the cap rock and reservoir at the time of baseline and monitor survey, respectively. Reflected amplitudes are picked at plexiglas-PVC and plexiglas-phenolic (along the direction of the isotropic plane for phenolic) interfaces and are corrected for geometrical spreading, emergence angle, free surface, transmission loss, and radiation patterns. Results indicate that higher order expansion terms, involving products of elastic time-lapse perturbation and baseline medium perturbation, match laboratory data with significantly reduced error in comparison to linearized forms. We conclude that in many plausible time-lapse scenarios the increase in accuracy associated with higher order corrections demonstrated in this thesis enhances time-lapse modeling.

In the last part of the study, in conjunction with Talisman Energy Inc. part of Repsol Group, a multicomponent time-lapse seismic data set, which was acquired during hydraulic fracturing of two horizontal wells in the unconventional Montney Reservoir at Pouce Coupe Field in the Peace River area, has been used to compare our theoretical results for P-P data.

These real data are analyzed to validate derived linear and nonlinear theoretical results for the time-lapse AVO difference during the change in a reservoir from the baseline survey relative to the monitor survey. A well tie has been generated to determine the location of the reservoir on the seismic data at the Montney Formation. Synthetic logs for P-wave and S-wave velocities and density are then generated for the monitor survey. Analyzing the baseline and monitor surveys shows that the nonlinear components of the difference data interpretation scheme do not contribute significantly to estimate time-lapse AVO difference. This is consistent with the fact that the Pouce Coupe data set has a low baseline contrast between the layer above the reservoir and reservoir and a low time-lapse contrast from the baseline survey to the time of the monitor survey. Expanding the field data component of this research, to provide field case studies validating the nonlinear portion of the theory in addition to the linear portion, is a matter of ongoing research which will confirm after this thesis.

Acknowledgements

I would like to first thank my supervisor, Dr. Kristopher Innanen for all his constant support, encouragement, guidance and most importantly for giving me the chance and opportunity for improving my academic abilities and fulfilling my dreams. Special thanks is made to my distinguished supervisory and examiner committee members (Dr. Edward Krebes, Dr. Laurence Lines, Dr. Michael Wieser, and Dr. Alison Malcolm) for their guidance and direction with my thesis corrections . Also, I would like to express my gratitude to Dr. Joe Wong for his wonderful help in acquiring the physical model data, his advice and many helpful and knowledgeable discussions throughout physical modeling study.

I would like to add my grateful thanks to the CREWES (Consortium for Research in Elastic Wave Exploration Seismology) community, staff and students, specially to Laura Baird for her distinguished assistant during this research, Kevin Hall and Kevin Bertram for their help when it came to any technical computing issues, and David Henley for applying his radial trace filtering in PROMAX to seismic gathers in physical modeling data.

I greatly appreciate Talisman Energy Inc. part of Repsol Group and David D'Amico for providing the Pouce Coupe data set for this study, Sensor Geophysical particularly Dr. Jeff Grossman for all the processing efforts, and CGG Hampson Russell software for AVO analyzing of data.

A special thanks to Andreas Cordsen and Dr. Helen Isaac for their time and efforts in editing this thesis, and critical discussion about seismic acquisition and seismic processing.

I would like to acknowledge CREWES industrial sponsors and NSERC (Natural Science and Engineering Research Council of Canada) through the grant CRDPJ 461179-13, Society of Exploration Geophysicists (SEG) Foundation/Apache Scholarship, and Queen Elizabeth II Graduate (Doctoral) scholarship for funding this research.

Most importantly, I must thank my parents for their constant love and support, and

letting me spread my wings in whatever direction I wanted to pursue my dreams. Last but not the least I would like to express my appreciation to my husband, Michael Clegg, for his support, patience, and faith in my abilities and also editing this thesis.

Dedication

To Isaac Newton who is my inspiration to follow my first love - physics,

To Naser Jabbari, my beloved brother who left this world well before his time and before accomplishing his life goals,

Finally to my husband, Michael Clegg, who lightens my life with his love, care, warmth, understanding and support.

Table of Contents

List of Tables

List of Figures

List of Symbols and Abbreviations

Symbol	Definition
AGC	Automatical Gain Control
AVAZ	Amplitude variation with azimuth
AVO	Amplitude variation with offset
CMP	Common Mid Point
CREWES	Consortium for Research in Elastic Wave Exploration Seismology
NMO	Normal-Move-Out
CMP	Common Mid-Point
θ	P-wave incidence angle
ϕ	S-wave incidence angle
3C	Three-component
1D	One-dimension
2D	Two-dimension
3D	Three-dimension
4D	Four-dimension
P-wave	Compressional wave
S-wave	Shear wave
c_0	Reference velocity
c	Perturbed velocity
V	Velocity
α	Perturbation in velocity
V_P	P-wave or compressional velocity
V_S	S-wave or Shear velocity

R	Reflection coefficient
T	Transmission coefficient
R_{PP}	Amplitude of reflected P-wave from an incident P-wave
R_{SS}	Amplitude of reflected S-wave from an incident S-wave
R_{PS}	Amplitude of reflected S-wave from an incident P-wave
R_{SP}	Amplitude of reflected P-wave from an incident S-wave
ΔR_{PP}	Time lapse difference data P-P data reflectivity
ΔR_{SS}	Time lapse difference data shear wave reflectivity
ΔR_{PS}	Time lapse difference data converted wave reflectivity
ΔR_{SP}	Time lapse difference data converted wave reflectivity
ρ	Density
C_2O	Carbon dioxide
P	Matrix representation of P-wave Zoeppritz equations elements
S	Matrix representation of S-wave Zoeppritz equations elements
b_P	Vector representation of P-wave Zoeppritz equations elements
C_S	Vector representation of S-wave Zoeppritz equations elements
I	Identity operator
L	Differential operator
t	Travel time
ω	Angular frequency
λ	Wavelength
k	Wave number

∇	Divergence operator
$\mathbf{V}$	Perturbation operator
a(t)	Source distribution with extent in time,
$\xi(\mathbf{r})$	Source distribution with extent in space
$A(\omega)$	Source distribution with extent in frequency
$\mathbf{G}_0$	Unperturbed Green's function
$\mathbf{G}$	Green's function
$\mathbf{\Psi}$	A scalar representing the pressure at point $\mathbf{r}$ and time t
$P(\mathbf{r}, t)$	The scattered wavefield
$\Xi(\mathbf{r}, t)$	a source presenting mixtures of impulsive sources in time and space
δ	Source disturbance
Δ	Difference
PVC	Polyvinyl chloride
EOR	Enhanced oil recovery
FWI	Full waveform inversion
m	Meters
Kg	Kilograms
S	Seconds
ms	milliseconds
Hz	Hertz
MHz	Megahertz
$\sum$	Summation symbol
$\int$	Integral
Z	Depth
PSTM	Prestack time migrated

H	Step function
SEG-Y	Seismic data format developed by Society of Exploration Geophysicists
f-k filter	Frequency-wavenumber filter
RADAR	Receiver azimuth detection and rotation

Chapter 1

Introduction

1.1 Statement of the problem

In oil and gas development, exploration and production companies have developed and utilized geophysical techniques and methods to enhance oil and gas recoveries. Fields of study such as geology, petrophysics, geophysics, and reservoir engineering have been integrated to optimise exploration and development of hydrocarbon resources. The role of geophysics and seismic data in the exploration and development of hydrocarbons onshore and offshore has been proven to be important (Bjørlykke, 2010). Seismic monitoring of changes in reservoir parameters over time, or time-lapse seismic methods, have become a fundamental element of reservoir development plans. Time-lapse seismic data analysis is applied to monitor hydrocarbon/steam migration within reservoirs and can be linked to enhanced production. 4D time-lapse seismic data are also capable of monitoring underground storage of CO_2 gas and monitoring geohazards (Landrø, 2010). In 4D seismic data, a survey before production, the baseline survey, is compared with another survey after production, or monitoring survey. The difference data are the differences between the baseline survey data and the following monitor survey data (Greaves and Fulp, 1987; Lumley, 2001).

Changes in reservoir parameters such as fluid saturation and pressure can be related to changes in seismic parameters such as compressional and shear wave velocities (P-wave and S-wave velocities respectively), and density of a reservoir. The amplitudes of seismic arrivals or events vary with the distance between the source and receiver or offset. Amplitude variation with offset (AVO) methods can be used to determine thickness, porosity, density, velocity, lithology and fluid content of rocks as the amplitude of a reflection wave changes at the boundary between rocks (Castagna and Backus, 1994; Aki and Richards, 2002). Time-

lapse AVO signatures can be used to estimate fluid and pressure related changes in a reservoir because of their sensitivity to the changes in P-wave and S-wave velocities and density (Tura and Lumley, 1998; Landrø et al., 1999). Landrø (2001) expressed the relationship between changes in seismic parameters with fluid saturation and pressure changes. He obtained (with the assumption that cap rock seismic property stays the same for both baseline and monitor surveys) a linear approximation for the change in reflectivity for P-wave velocity of the difference data which occurs when the fluid saturation and pressure change in a reservoir (Landrø, 2001):

$$\Delta R_{PP}(\theta) = \frac{1}{2}\left(\frac{\Delta\rho}{\rho} + \frac{\Delta V_P}{V_P}\right) - 2\frac{V_S^2}{V_P^2}\left(\frac{\Delta\rho}{\rho} + 2\frac{\Delta V_S}{V_S}\right)\sin^2\theta + \frac{\Delta V_P}{2V_P}\tan^2\theta, \tag{1.1}$$

where ΔR_{PP} is the difference data reflection coefficient, ΔV_P, ΔV_S, and $\Delta\rho$ are time-lapse changes in P-wave and S-wave velocities and density, respectively. V_P, V_S, and ρ are the average P-wave, S- wave, and density between the cap rock and reservoir at the time of the baseline survey. The applicability of Landrø's linear equation for difference time-lapse data is dependent on the degree of the contrast between cap rock and reservoir in the baseline survey and also changes in the reservoir parameters from the time of the baseline survey relative to the time of the monitor survey. When these contrasts are relatively large, which is plausible in time-lapse scenarios, as shown by Landrø (2001), the accuracy of the linear approximation diminishes. This suggests that the nonlinearity of the difference data and time-lapse changes should be accounted for. Therefore, obtaining higher-order terms of relative changes in P-wave and S-wave velocities and density for time-lapse difference data is a high priority, especially when a higher contrast in the reservoir between the baseline and monitor surveys is suspected (Landrø, 2001; Thore and Hubans, 2012). Trani et al. (2011) showed that the linear approximation of changes in gradient reflectivity can cause biased estimates of changes in saturation and the leakage between estimated pressure and saturation changes. These effects can be reduced by including higher order terms into description of changes in gradient reflectivity (Trani et al., 2011). Also Landrø initially provided second-

order approximation terms for time-lapse reflectivity change by adapting the linear equations (Landrø, 2001).

With this research, we concern ourselves with the nonlinearity in the relationship between changes in the reflectivity of time-lapse difference data and the relative changes in the elastic properties of the target, and accuracy issues which may arise from its linearization. Within the nonlinear terms we note and analyze the important role played by coupling between baseline properties and time-lapse changes in determining reflectivity changes. This coupling, discussed in the acoustic limit by Innanen et al. (2014), is being studied in the elastic time-lapse context for the first time in this thesis.

1.2 Seismic time-lapse monitoring

Reservoir properties change over time due to production or the employment of enhanced oil recovery techniques (EOR). These techniques such as water flooding, gas injection, steam flooding, and hydraulic fracturing are implemented to enhance the reservoir recovery operation by restoring formation pressure and improving the fluid flow (Speight, 2013). Both production and EOR techniques can change fluid saturation, pressure and temperature in a reservoir, and this will cause changes in elastic parameters. Time-lapse studies monitor these changes in the reservoir over time and help to optimize the efficiency of the production. In the time-lapse monitoring process, a baseline survey is acquired prior to onset of production for a given reservoir. This is followed by one or more seismic surveys (monitor surveys) over a particular interval of time during which geological/geophysical characteristics of a reservoir are expected to change. Comparison of repeated seismic surveys over months, years, or decades adds the dimension of calendar time to our data analysis capability. Subtracting the baseline survey data from the monitor survey data forms time-lapse seismic difference data (Lumley, 2001; Arts et al., 2004; Greaves and Fulp, 1987).

Time-lapse difference data in principle reflect changes occurring in the reservoir from the

onset time of the baseline survey relative to the time of the monitor survey. For this to be true, both baseline and monitor images must be independent of the acquisition geometry. The quality of time-lapse seismic difference data, therefore depends on the repeatability between the baseline and monitor surveys. Many factors such as noise, change in source wavelet, weather, sea currents (for marine surveys) and any other survey conditions diminish the repeatability. Developments in seismic acquisition and processing have improved the quality of time-lapse data and repeatability, which improve the time-lapse interpretation (Nguyen et al., 2015; Vedanti et al., 2009; Eastwood et al., 1999; Johnston, 1997).

Time-lapse seismic data captures dynamic behaviours of the reservoir which are not predicted by static reservoir modelling, and are typically characterized by simulation models. Major oil companies now use time-lapse seismic data in reservoir management (Johnston, 2013; De Waal and Calvert, 2003; Tura, 2003).

Changes in properties of a reservoir produce corresponding changes in P-wave and S-wave velocities and density. The 4D time-lapse signal is sensitive to the changes of impedance and interval parameters in the reservoir, which lead to measurable changes in seismic amplitude and travel time of the seismic traces. An example of this is a noticeable phase-shift (Thore and Hubans, 2012). Changes in seismic arrival time in the monitor survey in comparison with the baseline survey, or time-shift analysis, provide information about the vertical distribution of changes in a reservoir due to production (Landrø, 2001; Trani et al., 2011; Ghaderi and Landrø, 2009; Thore and Hubans, 2012; Yang et al., 2014). Time-shifts may be due to the physical displacement of the reservoir boundaries or a velocity change above the reservoir. Yang et.al. presented a time-lapse image domain wavefield tomography (IDWT) method to monitor time-shift caused by time-lapse velocity changes.

A model-based inversion method has been developed by Thore and Hubans (2012) to estimate the changes in the elastic properties of a reservoir due to production. They suggested a formula relating the difference between the baseline trace and the monitor trace to the

changes in the P-wave velocity and the density (Thore and Hubans, 2012; Williamson et al., 2007). Thore and Hubans (2012) and Williamson (2007) make use of a model based formula which takes into account time-shifts of events of interest which occur because of time-lapse changes in the P-wave velocity of the overburden. This formula, which is not derived but simply intuited, is highly nonlinear, since the shift of a $\Delta V_P/V_P$ interface is given by the sum of $\Delta V_P/V_P$ itself from the surface to the interface. The role of nonlinearity between time-lapse medium property changes and time-lapse difference data is a key theme in this thesis.

Time-lapse changes also induce amplitude changes in the seismic data, wherein nonlinearity may play a significant role. Innanen et al. (2014) investigated a mathematical description of production or gas/fluid injection induced changes in the reservoir and the associated variation in AVO and travel time signature. Their work was limited to acoustic and absorptive-acoustic cases, however (Innanen et al., 2014). In this thesis a full elastic account of linear and nonlinear difference reflection data amplitudes is provided . AVO analysis of the 4D time-lapse signal during the production period is investigated by building a theoretical framework to model these changes.

1.3 Expected changes in elastic properties due to change in reservoir parameters

4D time-lapse monitoring links reservoir parameters such as fluid saturation and pressure to seismic parameters such as P-wave and S-wave velocities, and density. This link is theoretically founded on physics models such as the Gassmann model (Landrø, 2010). Time-lapse changes can be characterized by changes in fluid saturation and pore pressure. However, the pressure effect on the 4D seismic data is not the same as fluid saturation effect. Of the two, saturation changes have typically larger effect on seismic parameters than pressure but counterexamples do exist (Landrø, 2001). Time-lapse AVO methods discriminate be-

tween changes in the pore pressure and saturations in the reservoir (Veire et al., 2006). Tura and Lumley (1998) and Landrø et al. (1999) separately developed methods to discriminate between pore pressure and saturation changes, based on the idea that S-wave velocity is not sensitive to fluid saturation, whereas P-wave velocity and density vary relative to both pressure and fluid saturation changes (Tura, 2003).

The relationships between seismic parameters and fluid saturation and pore pressure is approximated linearly by Landrø (2001). Bhakta and Landrø (2014) estimated more realistic saturation and pressure changes for shallow reservoir with high V_P/V_S ratio, where Landrø's linear approximation is not accurate. They used a method based on stepwise linear approximations to the intercept and gradient reflectivity changes for a shallow reservoir. Expected changes in P-wave and S-wave velocities and density can be very significant. For example core measurements in Gullfaks 4-D seismic studies shows the average change for P-wave and S- velocities and density for 100% increase in fluid saturation are +13%, -2%, and +4% (Landrø et al., 1999).

1.4 Review of seismic technology based on scattering theory

In seismic exploration and monitoring, an active source sends an incident wave into the Earth and a group of receivers records the reflected wave, which encodes information about Earth properties (Oldham, 1906). The goal of exploration seismology is to extract information about the subsurface, such as spatial locations of the target reflectors, from the seismic data. In seismic inversion, the properties and location of the Earth subsurface layers can be obtained from measurements of reflected seismic wave, utilizing seismic processing methods and geological information from wells (Yilmaz, 2001).

Many theoretical methods have been established to predict the location of reflectors in the subsurface. Green's Theorem (Morse and H, 1953) estimates the wavefield in a medium from boundary conditions given knowledge of the physical properties of the medium such

as velocity. In some situations, such as subsalt, sub-basalt, and subvolcanics; when the medium becomes more complex, current velocity analysis techniques are not able to provide an accurate velocity model and this will affect the accurate prediction of the exact location of the reflectors (Weglein et al., 2000).

In full waveform inversion (FWI) methods (Lailly, 1983; Tarantola, 1984; Virieux and Operto, 2009), an initial model of the complex medium is defined and then numerous iterative updates are accomplished for the initial model in order to reach to least-squares minimization of the misfit between the modelled data and the actual complex medium. Building an accurate initial model, minimization criteria, and the sensitivity of the model to a frequency of the source are challenges in FWI (Virieux and Operto, 2009).

Scattering theory, or perturbation theory, can be used as a powerful theoretic approach to understand and process seismic data using the above methods. In scattering theory, the wavefield in a heterogenous medium is described as a perturbation about a known medium or a reference medium. The elastic properties of this reference medium undergo changes because of a perturbation in the medium. The difference between the actual perturbed medium and the unperturbed reference medium, is called the scattered wavefield. A forward problem is designed to characterize the wavefield emanating from a source and propagating through an Earth model by representing the wavefield in terms of a reference wavefield and a perturbation in the medium (Matson, 1996).

Scattering theory also defines an inversion process in addition to the forward problem. The basic framework is estimating the difference between the actual and reference medium through a perturbation operator. The application of inverse scattering theory in imaging and interpretation of seismic data is an ongoing research subject in exploration seismology (Weglein et al., 2002). The inverse scattering theory accounts for any difference in wave velocity in the reference medium and the actual medium. Inverse scattering series in principle can produce an image of the reflectors in depth without knowing the velocity model (Weglein

et al., 2003).

Inverse scattering theory is a direct inversion method which describes the actual complex medium including primary and multiple reflection events with transmission coefficients. Inverse scattering methods are based on the wave theory and form a complete series of terms each describing an event (Moses, 1956; Weglein et al., 1997; Carvalho et al., 1991).

Scattering theory relates the perturbation in the medium to a perturbation in the reference wavefield which is propagating into the perturbed medium. If $\mathbf{L}_0$ and $\mathbf{L}$ are the differential operators that describes wave propagation in the reference and actual (perturbed) medium, $\mathbf{G}_0$ and $\mathbf{G}$ are the corresponding Green's functions, and $\mathbf{I}$ is the identity operator (Weglein et al., 2003):

$$\begin{aligned} \mathbf{L}_0\mathbf{G}_0 &= \mathbf{I} \\ \mathbf{L}\mathbf{G} &= \mathbf{I}. \end{aligned} \tag{1.2}$$

Based on the Lippmann-Schwinger equation, $\mathbf{G}_0$ and $\mathbf{G}$ are related as

$$\mathbf{G} - \mathbf{G}_0 = \mathbf{G}_0(\mathbf{L}_0 - \mathbf{L})\mathbf{G}. \tag{1.3}$$

If we define the perturbation as $\mathbf{V} = \mathbf{L}_0 - \mathbf{L}$, iterating the Lippmann-Schwinger equation back into itself generates:

$$\mathbf{G} = \mathbf{G}_0 + \mathbf{G}_0\mathbf{V}\mathbf{G}_0 + \mathbf{G}_0\mathbf{V}\mathbf{G}_0\mathbf{V}\mathbf{G}_0 + ..., \tag{1.4}$$

$\mathbf{G}$ is the actual or perturbed wavefield, and based on this equation, can be described in terms of infinite series which are function of reference wavefield. The scattered wavefield is defined as $\mathbf{\Psi} = \mathbf{G} - \mathbf{G}_0$, we have,

$$\mathbf{\Psi} = \sum_{n=1}^{\infty} \mathbf{G}_0(\mathbf{V}\mathbf{G}_0)^n. \tag{1.5}$$

This equation describes how we can build a full waveform of propagation of the wave in the actual medium by a reference wavefield and the perturbation knowledge from the actual perturbed medium. The inverse process which is called inverse scattering theory,

can compute the perturbation parameter or actual medium properties with the recorded reflection data from the actual medium and an inverse scattering model (Innanen, 2008).

1.5 Application of scattering theory in time-lapse studies

Perturbation theory is a powerful theoretical approach to model and invert seismic data and can also be used in modelling and interpreting 4D time-lapse data. The main concept in scattering theory, as discussed earlier, is to compute a wavefield in a heterogeneous medium by using a wavefield in a reference medium, perturbed with a function which is related non-linearly to local earth properties. The scattering theory can also be applied to time-lapse studies by setting the baseline survey to be the reference or background medium, and the monitoring survey to be the perturbed medium (Zhang, 2006). The difference data, which are the difference between the baseline survey data and the monitor survey data, are considered as the scattered wavefield data. Innanen et al. (2014) have pointed out that this analysis requires a representation of difference data as an expansion in terms of both the time-lapse perturbation and the baseline medium properties in order to be self consistent. One of the main obstacles to using linear scattering theory to predict the model for the difference data in time-lapse problem is the production of spurious events and/or amplitude variations due to the complexity of the reference medium, i.e., the baseline medium. A possible solution to this problem is to calculate the higher order terms in the Born series and investigating if these events can be removed by adding higher order terms (Innanen et al., 2014). Innanen et al. (2014) showed that a full scattering formulation of time-lapse data leads to an expansion in both time-lapse perturbations and those representing baseline medium variations. This work was limited to acoustic and absorptive-acoustic cases, however. Here in this research, I will provide a full elastic accounting for time-lapse difference reflection data for P-P data, converted waves, and shear waves. Then validation of this comprehensive framework will be investigated with numerical examples, physical modelling, and real field data.

1.6 Thesis overview

In Chapter 2, a mapping method between the Earth model and seismic data by Matson (1996) is reviewed. I will show how full series terms produced by scattering theory are able to predict and interpret seismic reflection data including primary and multiple events. This can form the basis for multiple attenuation. Then the application of scattering theory in time-lapse problems by Innanen et al. (2014) will be presented. An amplitude perturbed time-lapse problem which is the focus of this thesis will be reviewed.

In Chapter 3, the time-lapse difference data are investigated for P-P data, shear waves (SS waves), and converted (PS, and SP) waves. Difference data are described as a function of two groups of perturbation parameters. The first perturbation occurs due to physical contrast in the baseline survey between the reservoir and overburden medium. The second perturbation is only considered in the reservoir due to the changes in the reservoir from the time of the baseline survey relative to the monitor survey. A framework for linear and non linear time-lapse difference reflection data in order of physical change or baseline interface contrast and time-lapse changes is formulated using amplitude variation with offset (AVO) methods. These difference data are categorized in term of the order in these perturbation parameters. The results from these frameworks then, are tested with various synthetic data scenarios.

In Chapter 4, a physical modelling study is performed to validate our theoretical framework for P-P data. The Consortium for Research in Elastic Wave Exploration Seismology (CREWES) physical modelling facility at the University of Calgary has been used to acquire and simulate a time-lapse problem to investigate the linear and nonlinear behaviour of theoretical time-lapse AVO difference data.

The framework for difference time-lapse AVO for P-P data with its validation with physical modelling study was published in Geophysics (Jabbari et al., 2015). The results for difference time-lapse AVO for shear waves and converted waves were presented at the Cana-

dian Society of Exploration Geophysicists (CSEG) GeoConvention (Jabbari and Innanen, 2015, 2016).

A multicomponent time-lapse seismic data set which has been acquired by Talisman Energy Inc. part of Repsol Group. is used to validate the theoretical framework for P-P data and will be explained in Chapter 5. This data set was acquired during hydraulic fracturing of two horizontal wells in the unconventional Montney Reservoir at Pouce Coupe Field in the Peace River area. In this chapter, we are analyzing these data to validate our linear and nonlinear theoretical results for the difference data during the change in a reservoir from the baseline survey relative to the monitor survey. Prestack time migrated common mid point gathers (PSTM CMP) for the baseline and two monitor surveys are used.

Conclusions are presented in Chapter 6

1.7 Thesis objectives

The main objective of this thesis is building a framework to express 4D time-lapse difference data in terms of linear and nonlinear changes in seismic parameters followed by validation of this framework with physical modelling study and real field data.

1.7.1 A theoretical analysis of time-lapse difference data

The objective is to develop altered versions of the second and third order nonlinear terms in addition to the first order term for P-P data, converted waves, and shear waves using scattering or perturbation theory. The goal is to build a detailed analysis of the nonlinear influence of elastic property contrasts across the reflector (e.g., cap rock over reservoir) at the time of the baseline survey, elastic property time-lapse perturbation and their coupling. Furthermore a numerical analysis will be performed using field data examples from literature to investigate the nonlinear behaviour of the obtained theoretical framework for time-lapse difference data.

1.7.2 Validation of time-lapse AVO formula using physical modelling data

Seismic physical modelling has been used for validation of wave theoretical results successfully since 1920s. Another objective of this research is to validate theoretical results for time-lapse difference data with a physical modelling data set in addition to numerical example validation.

1.7.3 Modelling of nonlinear time-lapse AVO with Pouce Coupe data set

A third objective of this thesis is to investigate the behaviour of nonlinear time-lapse AVO terms with a time-lapse field data set. The application of theoretical results in field data will be tested. For this purpose a Pouce Coupe data set has been provided by Repsol. This data set was acquired during hydraulic fracture stimulations of two horizontal wells targeting the Montney Silt Zone at Pouce Coupe, Alberta, Canada. The focus of this study is to compare higher order terms for a P-P data in the theoretical time-lapse difference data with multicomponent Pouce Coupe seismic data.

Chapter 2

Scattering or perturbation theory and its application in time-lapse problems

Scattering theory has been used widely in many applications in seismology including time-lapse problems. Up-to-date information of a reservoir provides programs to optimise the management of a reservoir and extends the useful life of an oilfield. A time-lapse survey, or 4D seismic monitoring introduces an important contribution to the production of hydrocarbons around the world and enables us to monitor the changes in the behaviour of a reservoir over time. In a time-lapse seismic survey, the baseline survey is compared with the monitoring survey. The difference data are the difference between the baseline survey and the following monitor surveys. Comparison of repeated seismic surveys over months, years, or decades adds the fourth dimension, time, to the seismic data (Greaves and Fulp, 1987; Lumley, 2001).

Scattering theory can be used as a framework to model these difference data in a time-lapse survey. Based on this theory, a wavefield in a heterogeneous medium is computed with a wavefield in a reference medium perturbed with a function which is related non-linearly to the Earth properties. This innovation is used to describe the difference data in time-lapse through resembling the baseline survey as the reference medium and the monitoring survey as the perturbed medium. The difference data are presented as the scattered wavefield data (Zhang, 2006).

We are engaged in a study of time-lapse seismic problem in the context of scattering or perturbation theory. To begin this project, we review a key theoretical antecedent, work of Matson (1996), on the Born series. Analytical calculation of the Born series shows that the higher order terms in the series alter the amplitude and adjust the velocity of the scattered

wavefield as well as describe internal multiple reflections. We will see how primary reflections are described by all of the terms in the series whereas a multiple which contains n reflections is described by the n^{th} and all higher order terms. Then we will review work done by Innanen et al. (2014) to establish a basic work to investigate the role and application of perturbation theory into time-lapse problems.

2.1 Born series- scattered field vs perturbation

Born series is an infinite series terms, describing wave propagation in the reference medium separated by different orders of perturbation or scattering interaction with a point scatterer Earth model. To form the Born series, we start with the scalar wave equation. All equations will be defined in three dimensions which can be extended to a multidimensional or can be simplified into two or one dimension.

2.1.1 Scalar wave equation

We start with three dimensional wave equation describing a scalar wave propagating in an acoustic media with constant density Innanen (2015):

$$\left[\nabla^2 - \left(\frac{1}{c^2(\mathbf{r})}\right)\left(\frac{\partial^2}{\partial t^2}\right)\right] P(\mathbf{r},t) = \Xi(\mathbf{r},t), \tag{2.1}$$

where the scalar $P(\mathbf{r},t)$ represents the pressure at point $\mathbf{r}$ and time t due to a source, $\Xi(\mathbf{r},t)$:

$$\Xi(\mathbf{r},t) = \begin{cases} \delta(t)\xi(\mathbf{r}) \\ a(t)\delta(\mathbf{r}-\mathbf{r}_s) \\ \delta(t)\delta(\mathbf{r}-\mathbf{r}_s) \\ 0 \end{cases}. \tag{2.2}$$

$\Xi(\mathbf{r},t)$ is a source distributed in time and space in a specified way. The velocity of the wave in the medium is $c(\mathbf{r})$ and ∇ is a multidimensional del operator in the 3D, 2D and 1D cases respectively:

$$\nabla = \left(\frac{\partial}{\partial x}, \frac{\partial}{\partial y}, \frac{\partial}{\partial z}\right), \quad \nabla = \left(\frac{\partial}{\partial x}, \frac{\partial}{\partial z}\right), \quad \nabla = \frac{\partial}{\partial z}. \tag{2.3}$$

Fourier transformation of equation 2.1 with respect to time leads to the wave equation in the frequency domain:

$$\left[\nabla^2 + \left(\frac{\omega^2}{c^2(\mathbf{r})}\right)\right] P(\mathbf{r},\omega) = \Xi(\mathbf{r},\omega), \tag{2.4}$$

where

$$\Xi(\mathbf{r},\omega) = \begin{cases} \xi(\mathbf{r}) \\ A(\omega)\delta(\mathbf{r}-\mathbf{r}_s) \\ \delta(\mathbf{r}-\mathbf{r}_s) \\ 0 \end{cases} . \tag{2.5}$$

The scalar equation 2.4 can also be presented in an operator form

$$\mathit{L}(\mathbf{r},\omega)P(\mathbf{r},\omega) = \Xi(\mathbf{r},\omega), \tag{2.6}$$

where

$$\mathit{L}(\mathbf{r},\omega) = \nabla^2 + \left(\frac{\omega^2}{c^2(\mathbf{r})}\right). \tag{2.7}$$

We can rewrite equation 2.4 as:

$$\left[\nabla^2 + \left(\frac{\omega^2}{c^2(\mathbf{r})}\right)\right] P(\mathbf{r},\mathbf{r}_s,k) = \delta(\mathbf{r}-\mathbf{r}_s), \tag{2.8}$$

where $k = \frac{\omega}{c_0}$ is the spatial wavenumber, ω is the temporal frequency and the source is an impulsive source happening in position $\mathbf{r}_s$ at time t_s . The velocity c($\mathbf{r}$) can be characterized by a constant reference velocity c_0 and a perturbation $\alpha(\mathbf{r})$ so that

$$\frac{1}{c^2(\mathbf{r})} = \left(\frac{1}{c_0^2}\right)[1-\alpha(\mathbf{r})].$$

This equation can be re-arranged to express the perturbation as:

$$\alpha(\mathbf{r}) = 1 - \frac{c_0^2}{c^2(\mathbf{r})}. \tag{2.9}$$

When this equation is substituted into equation 2.8, and the term in $\alpha(\mathbf{r})$ is brought to the right hand side of the equation, we obtain:

$$\left[\nabla^2 + \left(\frac{\omega^2}{c_0^2(\mathbf{r})}\right)\right] P(\mathbf{r},\mathbf{r}_s,k) = \delta(\mathbf{r}-\mathbf{r}_s) + \frac{\omega^2}{c_0^2(\mathbf{r})}\alpha(\mathbf{r})P(\mathbf{r},\mathbf{r}_s,k). \tag{2.10}$$

The first term on the right hand side is the impulsive source. The second term which includes the perturbation $\alpha(\mathbf{r})$ term, can also be considered as a kind of source. This term represents a deviation of the medium at position $\mathbf{r}$ from the reference medium property $c_0(\mathbf{r})$. This deviation causes the real wave to change its property from $c_0(\mathbf{r})$ to $c(\mathbf{r})$. This change in the field is what we see as scattering and for this reason we call the second term on the right a scattered source.

To solve equation 2.10, we will consider the reference medium as causal free space Greens's function which satisfies the equation

$$\left[\nabla^2 + k^2\right] G(\mathbf{r}, \mathbf{r}_s, k) = \delta(\mathbf{r} - \mathbf{r}_s). \tag{2.11}$$

An integral equation corresponding to equation 2.10 using Green's function as the reference wavefield and applying physical boundary conditions is (Weglein et al., 2003):

$$P(\mathbf{r}, \mathbf{r}_s, k) = G(\mathbf{r}, \mathbf{r}_s, k) + \int_{-\infty}^{\infty} G(\mathbf{r}, \mathbf{r}', k) k^2 \alpha(\mathbf{r}') P(\mathbf{r}', \mathbf{r}_s, k) d\mathbf{r}'. \tag{2.12}$$

The first and second terms in this equation, which is called the Lippmann-Schwinger equation, are the wavefield in the reference medium and the scattered field respectively. This equation represents the wavefield in a heterogeneous medium as the wavefield in a reference medium plus the scattered field due to the perturbation. The operator form of this equation (explained in section 1.4) is:

$$P = G_0 + G_0 V P, \tag{2.13}$$

where

$$V(\mathbf{r}, \mathbf{r}_s, \omega) = \alpha(r) \left(\frac{\omega^2}{c_0^2(\mathbf{r})} \right). \tag{2.14}$$

Iterating the Lippmann-Schwinger equation back into itself generates the Born series:

$$\begin{aligned} P(\mathbf{r}, \mathbf{r}_s, k) &= G(\mathbf{r}, \mathbf{r}_s, k) + \int_{-\infty}^{\infty} G(\mathbf{r}, \mathbf{r}', k) k^2 \alpha(\mathbf{r}') G(\mathbf{r}', \mathbf{r}_s, k) d\mathbf{r}' \\ &+ \int_{-\infty}^{\infty} G(\mathbf{r}, \mathbf{r}', k) k^2 \alpha(\mathbf{r}') \left[\int_{-\infty}^{\infty} G(\mathbf{r}', \mathbf{r}'', k) k^2 \alpha(\mathbf{r}'') G(\mathbf{r}'', \mathbf{r}_s, k)) d\mathbf{r}'' \right] d\mathbf{r}' \\ &+ ... = P_0 + P_1 + P_2 + ... \ . \end{aligned} \tag{2.15}$$

The terms in this series are referred here according to their order in α. For example, the zero-th order term is P_0 which is the first term in the series. Similarly, the first order term P_1 , is the second term in the series and so on for the other terms (Matson, 1996).

2.1.2 Born approximation

When the difference between the actual and reference medium is not large, the linear term in Born series can be used to approximately calculate data. This is referred as the linearized or Born approximation (Cohen and Bleistein, 1977). Truncating the Born series after the second term leads to the Born approximation. In this approximation, the measured data are linear in the model. When the perturbation is small, the higher order terms in the Born series (equation 2.15) become less important and the Born approximation is valid:

$$\begin{aligned} P(\mathbf{r}, \mathbf{r}_s, k) &\approx G(\mathbf{r}, \mathbf{r}_s, k) + \int_{-\infty}^{\infty} G(\mathbf{r}, \mathbf{r}', k) k^2 \alpha(\mathbf{r}') G(\mathbf{r}', \mathbf{r}_s, k) d\mathbf{r}' \\ &= P_0 + P_1. \end{aligned} \tag{2.16}$$

a) b)

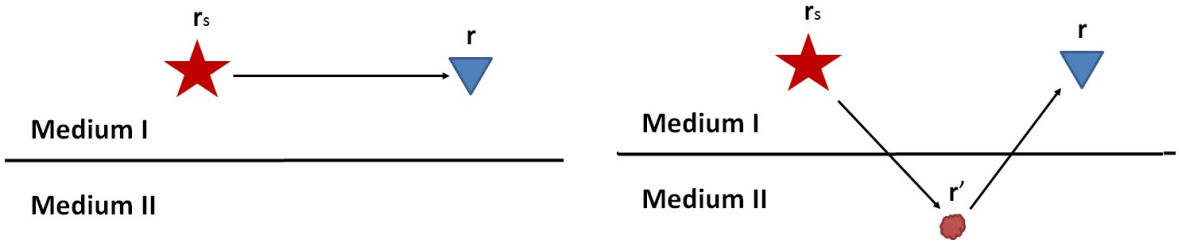

Figure 2.1: Physical interpretation of (a) P_0 and (b) P_1

Consider a one layer Earth model to describe the contribution of each term in equation 2.16. The first term in the Born approximation which is simply the Green's function, represents a direct wave propagating in the reference medium from the source at $\mathbf{r}_s$, to the measurement point at $\mathbf{r}$. The second term contains $k^2\alpha(\mathbf{r}')$ sandwiched between two Green's functions. The Green's function on the right represents a wave which propagates

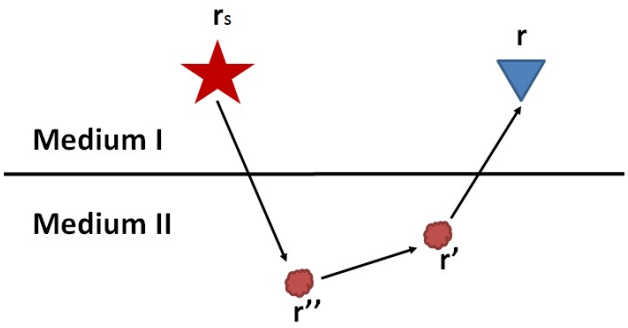

Figure 2.2: Physical interpretation of a wave with two scattering interactions in the medium.

from source at $\mathbf{r}_s$ to a point scatterer at $\mathbf{r}'$. The wave interacts with the scatterer at this point and propagates back to $\mathbf{r}$ via Green's function on the left. Therefore, the first order term is the integral over all possible single scattering interactions (Figure 2.1).

2.1.3 Non-linear terms

For larger values of perturbation larger subsets of Born series terms with higher order of perturbation are required (De Wolf, 1971, 1985). Higher order terms in Born series play an important role when the perturbation value is larger. The third term in equation 2.15 represents a wave which propagates in the reference medium and undergoes two scattering interactions (Figure 2.2).

Following this interpretation, each term in Born series involves a series of propagation in the reference medium and interactions with points within the scattering region.

2.2 Explicit calculation of terms in the Born series

The Born series have been described and derived in three dimensions in section 2.1. Here, we simplify these series into one dimension. The one dimensional constant density acoustic wave equation is:

$$\left[\frac{\partial^2}{\partial z^2} - \left(\frac{1}{c^2(z)}\right)\left(\frac{\partial^2}{\partial t^2}\right)\right] P(z, z_s, t) = \delta(z - z_s)\delta(t), \tag{2.17}$$

where $P(z, z_s, t)$ represents the pressure at point z and time t due to a one dimensional planar source at point z_s and time t = 0. The velocity c(z) can be characterized by a constant reference velocity c_0 and a perturbation $\alpha(z)$ so that

$$\frac{1}{c^2(z)} = \left(\frac{1}{c_0^2}\right)[1 - \alpha(z)],$$

or

$$\alpha(z) = 1 - \frac{c_0^2}{c^2(z)}. \tag{2.18}$$

Fourier transforming equation 2.17 with respect to time and substituting equation 2.18 into equation 2.17 gives

$$\left[\frac{\partial^2}{\partial z^2} + \left(\frac{\omega^2}{c_0^2}\right)\right] P(z, z_s, k) = \delta(z - z_s) + \left(\frac{\omega^2}{c_0^2}\right)\alpha(z)P(z, z_s, k), \tag{2.19}$$

where $k = \frac{\omega}{c_0}$ is the spatial wavenumber, and ω is the temporal frequency. To find a solution to equation 2.19, consider a causal free space Green's function $P_0(z, z_s, k)$ which satisfies the equation

$$\left[\frac{\partial^2}{\partial z^2} + k^2\right] G(z, z_s, k) = \delta(z - z_s). \tag{2.20}$$

Using this Green's function as a reference wavefield, an integral equation corresponding to equation 2.19 and its physical boundary conditions is (Weglein, 1985)

$$P(z, z_s, k) = G(z, z_s, k) + \int_{-\infty}^{\infty} G(z, z', k)k^2\alpha(z')P(z', z_s, k)dz'. \tag{2.21}$$

This is the Lippmann-Schwinger equation in one dimension. Based on this equation, the wavefield in a heterogeneous medium is the sum of the wavefield in a reference medium and an integral that represents the scattered field due to perturbation. Iterating the Lippmann-

Schwinger equation back into itself generates the Born series

$$
\begin{aligned}
P(z, z_s, k) = G(z, z_s, k) + \int_{-\infty}^{\infty} G(z, z', k) k^2 \alpha(z') G(z', z_s, k) dz' + \\
\int_{-\infty}^{\infty} G(z, z', k) k^2 \alpha(z') \left[\int_{-\infty}^{\infty} G(z', z'', k) k^2 \alpha(z'') G(z'', z_s, k) dz'' \right] dz' + \\
\int_{-\infty}^{\infty} G(z, z', k) k^2 \alpha(z') dz' \int_{-\infty}^{\infty} G(z', z'', k) k^2 \alpha(z'') \\
\int_{-\infty}^{\infty} G(z'', z''', k) k^2 \alpha(z''') G(z''', z_s, k) dz''' + ... \\
= P_0 + P_1 + P_2 + P_3 + ... \ .
\end{aligned}
\tag{2.22}
$$

All primary and multiple reflections due to the perturbation operator, α, are computed with this equation. The first three terms in this series are described in section 2.1. The zero-th order term in α, P_0 is the first term in the series and represents a direct wave propagating from the source in the reference medium to the measurement point or receiver. The first order term in α, P_1 , is the second term in the series and represents a wave propagating from source to a point scatterer at z'. This wave then undergoes a reflection at the scatterer, determined by $k^2\alpha(z')$, and propagate back to the measurement point. The third term is the second order term in α, P_2, and represents two scattering interactions. Similarly, the fourth term is the third order term in α, P_2, and represents three scattering interactions.

Truncating the Born series after the term including the first order in α, leads to the Born or linear approximation in one dimension.

2.3 Nonlinear scattering in time-lapse environment

Prior to utilizing a reservoir, a first seismic experiment called the baseline survey is acquired and after a particular interval of time following several geological/geophysical changes, another seismic survey, called monitor survey, is acquired. The difference data during the change in a reservoir from the baseline survey to monitor survey can be determined using the linear approximation of the Born series. The reference medium in time-lapse problem is the baseline survey and the perturbed medium is the monitor survey. Difference data, then

are formed by applying structural change in the baseline survey data and subtracting it from monitor survey data.

Because in the time-lapse scattering problems, the reference medium is as complicated as the perturbed medium, some difficulties such as spurious multiples in the difference data are encountered. It is necessary to extend the full version of the Born series to eliminate these unwanted events.

Seismic traces can differ in amplitude, frequency, polarity, or the location of the interfaces from the baseline survey to the monitor survey. The difference data between a baseline survey data and a monitor survey data is categorized as the change in either the amplitude or location of the boundary (Innanen et al., 2014). The study described here focuses on describing the difference data for amplitude changes in a reservoir with scattering theory.

2.3.1 An amplitude perturbed time-lapse problem

There are at least two seismic experiments involved in a time-lapse study, the baseline survey, followed by one or more monitoring survey. The difference data between the baseline and monitor survey are formed by subtracting the baseline data from the monitor data. We consider two acoustic semi-infinite half spaces with a single interface at Z_I. The density is constant but the acoustic impedance changes from the incident medium (above Z_I) to the target medium (below Z_I). The velocity also changes in the target medium from the time of the baseline survey (c_b) to the monitor survey (c_m), Figure 2.3. The study here is based on a single parameter acoustic medium varying in depth and is described by Innanen et al. (2014). In a time-lapse problem, the reference wavefield, or the Green's function, is the wavefield of the baseline survey and can be expressed from equation 2.11 as

$$\left[\frac{d^2}{dz^2} + \frac{\omega^2}{c_b^2(z)}\right] G(z, z_s; \omega) = \delta(z - z_s).$$

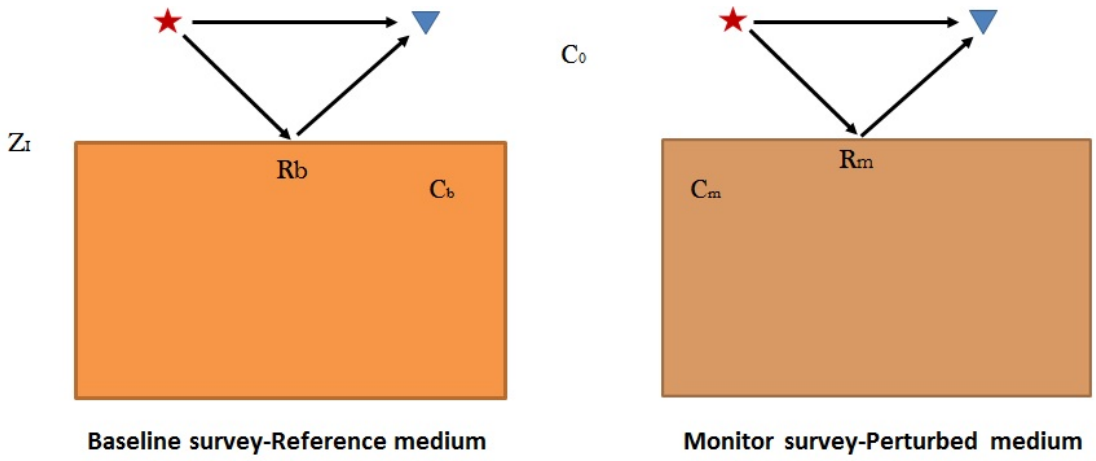

Figure 2.3: Illustration of an amplitude perturbed time-lapse problem.

For simplicity, the source is a pulse which is presented by a delta function at $z = z_s$, and the $1/c_b^2(z)$ is defined as

$$\frac{1}{c_b^2(z)} = \begin{cases} c_b^{-2}, & z > z_I \\ c_0^{-2}, & z < z_I \end{cases}, \tag{2.23}$$

c_0 and c_b are the incidence and target wavefield velocities at the time of the baseline survey. The perturbed medium has exactly the same structure but the target medium changed from c_b to c_m:

$$\left[\frac{d^2}{dz^2} + \frac{\omega^2}{c_m^2(z)}\right] P(z, z_s; \omega) = \delta(z - z_s), \tag{2.24}$$

where

$$\frac{1}{c_m^2(z)} = \begin{cases} c_m^{-2}, & z > z_I \\ c_0^{-2}, & z < z_I \end{cases}. \tag{2.25}$$

A dimensionless parameter is defined to model the time-lapse perturbation in velocity as:

$$a(z) = aH(z - z_I), \tag{2.26}$$

where H is step function and

$$a = 1 - \frac{c_b^2}{c_m^2}. \tag{2.27}$$

The baseline and monitor surveys consist of one spike wave at normal incidence on a single interface at each of two times. The Green's function for wave propagation in this medium for z_s , $z_g < z_I$, (z_g is the location of the receiver) consist of two possible wavefields, a direct wave from the source and measurement points, z_s and z_g, plus a primary reflection at the interface location z_I, Figure 2.3, and we label it with 00:

$$G_{00}(z_g, z_s) = \frac{e^{ik_0|z_g - z_s|}}{i2k_0} + R_b \frac{e^{ik_0(z_I - z_g)} e^{ik_0(z_I - z_s)}}{i2k_0}, \tag{2.28}$$

where $k_0 = \frac{\omega}{c_0}$, and $R_b = (c_b - c_0)/(c_b + c_0)$. The first term in this equation is the direct wavefield propagating from the source to the receiver, and the second term is the reflection from the interface location z_I. The Green's function when z_s , $z_g > z_I$, is

$$G_{11}(z_g, z_s) = \frac{e^{ik_b|z_g - z_s|}}{i2k_b} - R_b \frac{e^{ik_b(z_g - z_I)} e^{ik_b(z_s - z_I)}}{i2k_b}, \tag{2.29}$$

where $k_b = \frac{\omega}{c_b}$. The other possible locations of source and measurement points is when $z_g > z_I$, $z_s < z_I$, then the Green's function has the form of

$$G_{01}(z_g, z_s) = T_D e^{ik_0(z_I - z_s)} \frac{e^{ik_b(z_g - z_I)}}{i2k_b}, \tag{2.30}$$

where T_D in the transmission for the down going direction from the incident medium to the target medium

$$T_D = \frac{2c_b}{c_0 + c_b}. \tag{2.31}$$

The Green's function for the last possible locations of source and receiver is when $z_s > z_I$, $z_g < z_I$

$$G_{10}(z_g, z_s) = T_U e^{ik_b(z_s - z_I)} \frac{e^{ik_0(z_I - z_g)}}{i2k_b}, \tag{2.32}$$

where T_U in the transmission for the up going direction from the target medium to the incident medium

$$T_U = \frac{2c_0}{c_0 + c_b}. \tag{2.33}$$

Now, the first three terms in Born approximation can be calculated as

$$P(z_g, z_s) = P_0(z_s, z_g) + P_1(z_s, z_g) + P_2(z_s, z_g) + ..., \tag{2.34}$$

where

$$\begin{aligned} P_0(z_g, z_s) &= G_{00}(z_s, z_g) \\ P_1(z_g, z_s) &= \alpha k_0^2 \int_{z_I}^{\infty} G_{10}(z_s, z') G_{01}(z', z_g) dz' \\ P_2(z_g, z_s) &= \alpha^2 k_0^4 \int_{z_I}^{\infty} G_{10} \int_{z_I}^{\infty} G_{11}(z', z'') G_{01}(z'', z_g) dz''). \end{aligned}$$

Now we form the final result,

$$P(z_g, z_s) = \left[1 + e^{i2k_0 z_I} \left(R_b + \frac{a}{4} T_D T_U + \frac{a^2}{16} T_D T_U (2 - R_b) + ...\right)\right] \frac{1}{i2k_0}. \tag{2.35}$$

Knowing $T_D T_U = 1 - R_b^2$, we can form time-lapse difference field,

$$\begin{aligned} \Delta P(z_g, z_s) &= P(z_s, z_g) - P_0(z_s, z_g) \\ \Delta P(z_g, z_s) &= \left[\frac{a}{4}\left(1 - R_b^2\right) + \frac{a^2}{8}\left(1 - \frac{1}{2}R_b - R_b^2 - \frac{1}{2}R_b^3 ...\right)\right] \frac{e^{i2k_0 z_I}}{i2k_0}. \end{aligned} \tag{2.36}$$

2.3.2 Time-lapse interpretation

Equation 2.36 describes the scattered wavefield from the time of the baseline survey to the time of the monitor survey or time-lapse difference data. This equation includes the amplitude, the term in the bracket, and the phase of the wavefield. The phase of the scattered field is constant as the location of the interface between the incident target and the reservoir at the time of both baseline and monitor survey, z_I, remains unchanged. The amplitude of the scattered wavefield, ΔP, is the difference between the reflection coefficient between the baseline and monitor surveys and is acting in a way that to correct the reference or baseline reflection coefficient to produce the actual medium (monitor survey) reflection coefficient.

$$\begin{aligned} \Delta R &= R_m - R_b \\ R_m &= R_b + \left[\frac{a}{4}\left(1 - R_b^2\right) + \frac{a^2}{8}\left(1 - \frac{1}{2}R_b - R_b^2 - \frac{1}{2}R_b^3 ...\right)\right] \end{aligned} \tag{2.37}$$

Therefore, the property of the monitor survey can be calculated just by knowing the property of the baseline survey and the time-lapse perturbation.

Chapter 3

A theoretical analysis of linear and nonlinear time-lapse difference AVO

Time-lapse measurements provide a tool to monitor the dynamic changes in subsurface properties during the time of the exploitation of a reservoir. Time-lapse is a cost-effective approach for monitoring the changes in the fluid saturation and pressure over a period of time in a reservoir. The difference data during the change in a reservoir from the baseline survey to the monitor survey can be described through applying the scattering or perturbation theory. The perturbation theory is used as a framework to model these difference data in a seismic time-lapse study. The baseline survey is set to be the background medium which goes under perturbation by the time of the monitor survey. The perturbation presented here quantifies the changes in P-wave and S-wave velocities and density from the time of the baseline to the monitor survey.

Although P-wave seismic surveying is the primary survey method in seismology, using multicomponent recording can improve and support P-wave seismic data, specially for rocks with similar P-wave properties which may show a greater variation in S-wave properties. Multicomponent surveying has been developed rapidly in both land and marine acquisition and processing techniques, with many applications in structural imaging, lithologic estimation, anisotropy analysis, and reservoir monitoring. The elastic properties of a rock, as well as acoustic properties, change when the pressure and fluid flow is altered in a reservoir because of production. This raises the necessity of multicomponent 4D time-lapse analysis in a reservoir (Stewart et al., 2002, 2003).

Time-lapse AVO connotes the analysis of changes to the offset or angle dependence of reflection coefficients from the baseline to the monitor survey. The study described in this

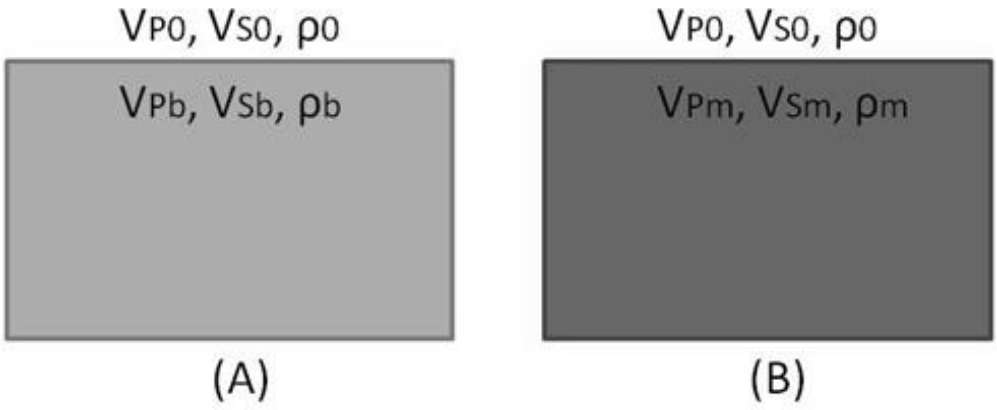

Figure 3.1: Rock properties of the model at the time of the baseline(A) and monitor (B) survey.

chapter focuses on applying the perturbation theory in time-lapse AVO method to model a framework to describe the difference data from a baseline survey to a monitor surveys in a reservoir. Reflection coefficients are derived for the baseline and monitor survey using Zoeppritz equations to calculate the reflection coefficient for difference data. Linear and nonlinear time-lapse difference data or $\Delta R_{PP}(\theta)$, $\Delta R_{PS}(\theta)$, $\Delta R_{SP}(\phi)$, and $\Delta R_{SS}(\phi)$, are defined in order of physical change or baseline interface contrast and time-lapse changes. The results of this chapter are published in Geophysics journal and presented at GeoConvention (Jabbari et al., 2015; Jabbari and Innanen, 2015, 2016).

3.1 Time-lapse difference data for P-P data

We will consider two seismic experiments involved in a time-lapse survey; a baseline survey followed by a monitoring survey. The P-wave and S-wave velocities and the density change from the time of the baseline survey relative to the monitoring survey (Figure 3.1). This pair of models is consistent with an unchanging cap rock overlying a porous target which is being produced. Let V_{P_0}, V_{S_0}, ρ_0 and V_{P_x}, V_{S_x}, ρ_x be the rock properties of the cap rock and reservoir (where x is substituted with b and m for the baseline and monitor surveys respectively) and a P-wave impinges on the boundary of a planar interface between these

two elastic media (Figure 3.2). Amplitudes of reflected and transmitted P and S waves are calculated through setting the boundary conditions in the Zoeppritz equations which can be rearranged in matrix form e.g. (Keys, 1989):

$$P \begin{bmatrix} R_{PP} \\ R_{PS} \\ T_{PP} \\ T_{PS} \end{bmatrix} = b_P, \tag{3.1}$$

where

$$P \equiv \begin{bmatrix} -\sin\theta & -\sqrt{1-B^2\sin^2\theta} \\ \sqrt{1-\sin^2\theta} & -B\sin\theta \\ 2B^2\sin\theta\sqrt{1-\sin^2\theta} & B(1-2B^2\sin^2\theta) \\ -1+2B^2\sin^2\theta & 2B^2\sin\theta\sqrt{1-B^2\sin^2\theta} \end{bmatrix}$$

$$\begin{bmatrix} C_x\sin\theta & \sqrt{1-D_x^2\sin^2\theta} \\ \sqrt{1-C_x^2\sin^2\theta} & -D_x\sin\theta \\ 2A_xD_x^2\sin\theta\sqrt{1-C_x^2\sin^2\theta} & A_xD_x(1-2D_x^2\sin^2\theta) \\ A_xC_x(1-2D_x^2\sin^2\theta) & -2A_xD_x^2\sin\theta\sqrt{1-D_x^2\sin^2\theta} \end{bmatrix}, \tag{3.2}$$

θ is the P-wave incident angle, and

$$b_P \equiv \begin{bmatrix} \sin\theta \\ \sqrt{1-\sin^2\theta} \\ 2B^2\sin\theta\sqrt{1-\sin^2\theta} \\ 1-2B^2\sin^2\theta \end{bmatrix}.$$

The ratio of elastic parameters are defined as:

$$A_x = \frac{\rho_x}{\rho_0}, \quad B = \frac{V_{S_0}}{V_{P_0}}, \quad B^{-1} \equiv \frac{V_{P_0}}{V_{S_0}}, \quad C_x = \frac{V_{P_x}}{V_{P_0}}, \quad D_x = \frac{V_{S_x}}{V_{P_0}}, \quad E \equiv \frac{V_{P_x}}{V_{S_0}}, \quad F \equiv \frac{V_{S_x}}{V_{S_0}}. \tag{3.3}$$

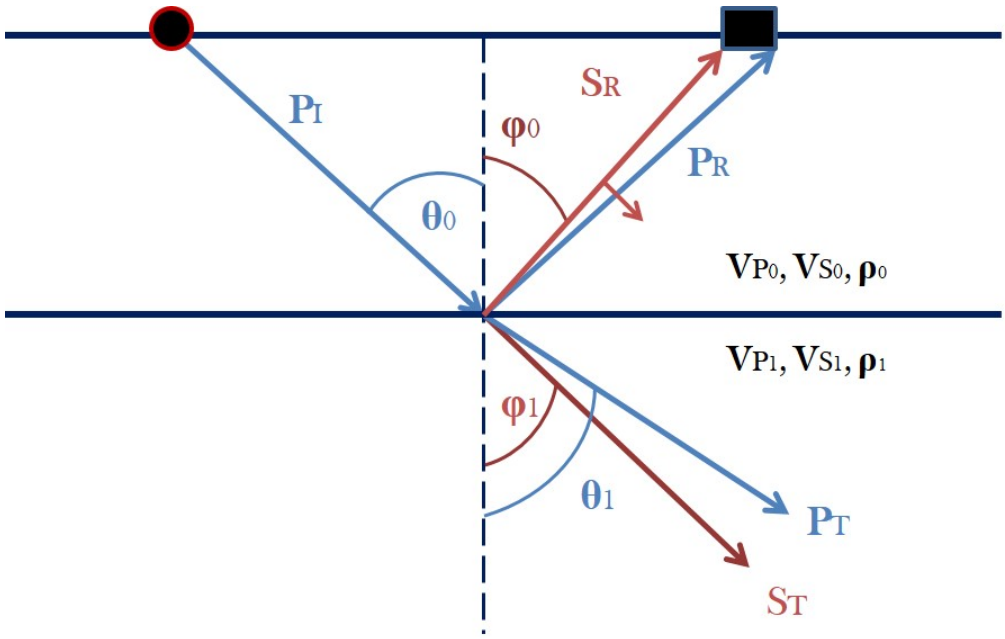

Figure 3.2: Displacement amplitude of an incident P-wave with related reflected and transmitted P-wave and S-waves.

We now form an auxiliary matrix P_P by replacing the first column in P with b_P. The reflection coefficient for an incident P-wave and reflected P-wave is determined by:

$$R_{PP}(\theta) = \frac{det(P_P)}{det(P)}. \tag{3.4}$$

R_{PP} for the baseline and monitor surveys are calculated using the method explained above, where rock properties for cap rock are the same, but reservoir properties change from V_{P_b}, V_{S_b}, ρ_b at the time of the baseline survey to V_{Pm}, V_{Sm}, ρ_m at the time of the monitor survey. If we replace $x = b$ for the baseline survey and $x = m$ for the monitor survey in equations 3.2 and equation 3.3, the reflection coefficients can be calculated for both.

In our time-lapse study we have considered two groups of perturbation parameters (Innanen et al., 2014; Stolt and Weglein, 2012). We use the same standard scattering nomenclature found in e.g. Stolt and Weglein (2012). The first group expresses the perturbation caused by propagating the wavefield from the first medium to the second medium in the baseline

survey:

$$b_{VP} = 1 - \frac{V_{P_0}^2}{V_{P_b}^2}, \;\; b_{VS} = 1 - \frac{V_{S_0}^2}{V_{S_b}^2}, \;\; b_\rho = 1 - \frac{\rho_0}{\rho_b}. \tag{3.5}$$

The second group expresses the time-lapse perturbation and accounts for the changes in the monitor survey relative to the baseline survey. We define:

$$a_{VP} = 1 - \frac{V_{P_b}^2}{V_{P_m}^2}, \;\; a_{VS} = 1 - \frac{V_{S_b}^2}{V_{S_m}^2}, \;\; a_\rho = 1 - \frac{\rho_b}{\rho_m}. \tag{3.6}$$

Applying equation 5.1.1 and equation 5.1.1, elastic parameters may be re-defined in terms of perturbations in P-wave and S-wave velocities and the densities as:

$$\begin{aligned}
A_b &= \frac{\rho_b}{\rho_0} = (1 - b_\rho)^{-1}, \\
C_b &= \frac{V_{P_b}}{V_{P_0}} = (1 - b_{VP})^{-\frac{1}{2}}, \\
D_b &= \frac{V_{S_b}}{V_{P_0}} = \frac{V_{S_0}}{V_{P_0}} \times \frac{V_{S_b}}{V_{S_0}} = B \times (1 - b_{VS})^{-\frac{1}{2}}, \\
E_b &= \frac{V_{P_b}}{V_{S_0}} = \frac{V_{P_0}}{V_{S_0}} \times \frac{V_{P_b}}{V_{P_0}} = B^{-1} \times (1 - b_{VP})^{-\frac{1}{2}}, \\
F_b &= \frac{V_{S_b}}{V_{S_0}} = (1 - b_{VS})^{-\frac{1}{2}}.
\end{aligned} \tag{3.7}$$

and

$$
\begin{aligned}
A_m &= \frac{\rho_m}{\rho_0} = \frac{\rho_m}{\rho_b} \times \frac{\rho_b}{\rho_0} \\
&= (1 - a_\rho)^{-1} \times (1 - b_\rho)^{-1}, \\
C_m &= \frac{V_{P_m}}{V_{P_0}} = \frac{V_{P_m}}{V_{P_b}} \times \frac{V_{P_b}}{V_{P_0}} \\
&= (1 - a_{VP})^{-\frac{1}{2}} \times (1 - b_{VP})^{-\frac{1}{2}}, \\
D_m &= \frac{V_{S_m}}{V_{P_0}} = \frac{V_{S_m}}{V_{S_0}} \times \frac{V_{S_0}}{V_{P_0}} = \frac{V_{S_0}}{V_{P_0}} \times \frac{V_{S_m}}{V_{S_b}} \times \frac{V_{S_b}}{V_{S_0}} \\
&= B \times (1 - a_{VS})^{-\frac{1}{2}} \times (1 - b_{VS})^{-\frac{1}{2}}, \\
E_m &= \frac{V_{P_m}}{V_{S_0}} = \frac{V_{P_m}}{V_{P_0}} \times \frac{V_{P_0}}{V_{S_0}} = \frac{V_{P_0}}{V_{S_0}} \times \frac{V_{P_m}}{V_{P_b}} \times \frac{V_{P_b}}{V_{P_0}} \\
&= B^{-1} \times (1 - a_{VP})^{-\frac{1}{2}} \times (1 - b_{VP})^{-\frac{1}{2}}, \\
F_m &= \frac{V_{S_m}}{V_{S_0}} = \frac{V_{S_m}}{V_{S_b}} \times \frac{V_{S_b}}{V_{S_0}} \\
&= (1 - a_{VS})^{-\frac{1}{2}} \times (1 - b_{VS})^{-\frac{1}{2}}.
\end{aligned}
\tag{3.8}
$$

These parameters are substituted into Zoeppritz matrix, P, in equation 3.2. The elements of this new matrix now, are functions of b_ρ, b_{VP}, b_{VS}, a_ρ, a_{VP}, a_{VS}, and $\sin\theta$. Using Taylor's series:

$$
\begin{aligned}
(1 - b_\rho)^{-1} &= 1 + b_\rho + b_\rho^2 + ... \\
(1 - b_{VP})^{-\frac{1}{2}} &= 1 + \frac{1}{2} b_{VP} + \frac{1 \times 3}{2 \times 4} b_{VP}^2 + ... \\
(1 - b_{VS})^{-\frac{1}{2}} &= 1 + \frac{1}{2} b_{VS} + \frac{1 \times 3}{2 \times 4} b_{VS}^2 + ... \\
(1 - a_\rho)^{-1} &= 1 + a_\rho + a_\rho^2 + ... \\
(1 - a_{VP})^{-\frac{1}{2}} &= 1 + \frac{1}{2} a_{VP} + \frac{1 \times 3}{2 \times 4} a_{VP}^2 + ... \\
(1 - a_{VS})^{-\frac{1}{2}} &= 1 + \frac{1}{2} a_{VS} + \frac{1 \times 3}{2 \times 4} a_{VS}^2 + ...
\end{aligned}
\tag{3.9}
$$

Zoeppritz matrix for the baseline and monitor surveys are then re-calculated. In the following section, we review calculating $R_{PP}(\theta)$ for the baseline survey.

3.1.1 Calculating reflection coefficients for the baseline survey

We now seek a way to expand the solutions for equation 3.4 about the contrasts across the interface in the baseline survey. Calculating elastic parameters in terms of perturbation parameters in the baseline by applying equation 3.7 and equation 3.8 into equation 3.2, the elements of the Zoeppritz matrices now are re-calculated as functions of b_ρ, b_{VP}, b_{VS}, and $\sin\theta$. Using Taylor's series and truncating the expansions of b_ρ, b_{VP}, b_{VS} after second order, and $\sin\theta$, after second order, Zoeppritz equation is re-calculated as:

$$P(:,1) = \begin{bmatrix} -\sin\theta \\ -1 + \frac{1}{2}B^2\sin^2\theta \\ \sin\theta + \frac{1}{2}\sin\theta b_{VB} + \frac{3}{8}\sin\theta b_{VB}^2 \\ 1 - \frac{1}{2}B^2\sin^2\theta(1 + b_{VS} + b_{VS}^2) \end{bmatrix},$$

$$P(:,2) = \begin{bmatrix} 1 - \frac{1}{2}\sin^2\theta \\ -B\sin\theta \\ 1 - \frac{1}{2}\sin^2\theta(1 + b_{VB} + b_{VB}^2) \\ -B\sin\theta(1 + \frac{1}{2}b_{VS} + \frac{3}{8}b_{VS}^2) \end{bmatrix},$$

$$P(:,3) = \begin{bmatrix} 2B^2\sin\theta \\ B(1 - 2B^2\sin^2\theta) \\ 2B^2\sin\theta(1 + a_\rho + b_{VS} + a_\rho^2 + b_\rho b_{VS} + b_{VS}^2 \\ [(B(1 - 2B^2\sin^2\theta)(1 + b_\rho + \frac{1}{2}b_{VS} + \frac{1}{2}b_\rho b_{VS} + b_\rho^2 + \frac{3}{8}b_{VS}^2) \\ -B^3\sin^2\theta(2b_{VS} + 2b_\rho b_{VS} + 3b_{VS}^2)] \end{bmatrix},$$

and

$$P(:,4) = \begin{bmatrix} -1 + 2B^2\sin^2\theta \\ 2B^2\sin\theta \\ [(1 - 2B^2\sin^2\theta)(1 + \frac{1}{2}b_{VB} + b_\rho + \frac{1}{2}b_\rho a_{VB} + b_\rho^2 + \frac{3}{8}b_{VB}^2) \\ -2B^2\sin^2\theta(b_{VS} + b_{VB}b_{VS} + b_\rho b_{VS} + b_{VS}^2)] \\ -2B^2\sin\theta(1 + b_{VS} + b_\rho + b_{VS}^2 + b_\rho b_{VS} + b_\rho^2) \end{bmatrix},$$

where B is the elastic parameter described in equation 3.3 and θ is the P-wave incident angle.

Exact $R_{PP}(\theta)$ is calculated using equation 3.4, and can be organized into terms that are first, second, etc. order in any of perturbation parameters, b_ρ, b_{VP} and b_{VS}:

$$R_{PP}(\theta) = R^{(1)}_{PP}(\theta) + R^{(2)}_{PP}(\theta) + ... \tag{3.10}$$

Having truncated exact R_{PP} beyond the first order and second order, $R^{(1)}_{PP}$ and $R^{(2)}_{PP}$ are calculated as:

$$\begin{aligned}
R^{(1)}_{PP}(\theta) &= (\frac{1}{4} + \frac{1}{4}\sin^2\theta)b_{VB} + (-2\left(\frac{V_{S_0}}{V_{B_0}}\right)^2\sin^2\theta)b_{VS} + (\frac{1}{2} - 2\left(\frac{V_{S_0}}{V_{B_0}}\right)^2\sin^2\theta)b_\rho. \\
R^{(2)}_{PP}(\theta) &= (\frac{1}{8} + \frac{1}{4}\sin^2\theta)b^2_{VB} + \left[\left(\frac{V_{S_0}}{V_{B_0}}\right)^3\sin^2\theta - 2\left(\frac{V_{S_0}}{V_{B_0}}\right)^2\sin^2\theta\right]b^2_{VS} \\
&\quad + \left[\frac{1}{4} - \frac{1}{4}B\sin^2\theta - \left(\frac{V_{S_0}}{V_{B_0}}\right)^2\sin^2\theta + \left(\frac{V_{S_0}}{V_{B_0}}\right)^3\sin^2\theta\right]b^2_\rho \\
&\quad + \left[2\left(\frac{V_{S_0}}{V_{B_0}}\right)^3\sin^2\theta - B^2\sin^2\theta\right]b_\rho b_{VS}.
\end{aligned} \tag{3.11}$$

3.1.2 Calculating reflection coefficients for time-lapse difference data

$R_{PP}(\theta)$ for the monitor survey is calculated exactly with the same method explained for the baseline survey in the previous section. The reflection coefficient for the difference data between the baseline survey data and monitor survey data are then calculated as:

$$\Delta R_{PP}(\theta) = R^m_{PP}(\theta) - R^b_{PP}(\theta). \tag{3.12}$$

The determinants and determinations in equation 3.4 are calculated for both surveys and the reflection coefficient for the difference data in equation 3.12 is expanded in orders of all six perturbations, and $\sin^2\theta$:

$$\Delta R_{PP}(\theta) = \Delta R^{(1)}_{PP}(\theta) + \Delta R^{(2)}_{PP}(\theta) + \Delta R^{(3)}_{PP}(\theta) + ... \ . \tag{3.13}$$

The linear and second order terms in the reflection coefficient for the difference data are as

follows:

$$\Delta R_{PP}^{(1)}(\theta) = \left[\frac{1}{4} + \frac{1}{4}\sin^2\theta\right] a_{VP} + \left[-2\left(\frac{V_{S_0}}{V_{P_0}}\right)^2 \sin^2\theta\right] a_{VS} + \left[\frac{1}{2} - 2\left(\frac{V_{S_0}}{V_{P_0}}\right)^2 \sin^2\theta\right] a_\rho$$

$$\begin{aligned}
\Delta R_{PP}^{(2)}(\theta) = &\left[\frac{1}{8} + \frac{1}{4}\sin^2\theta\right] a_{VP}^2 + \left[\left(\frac{V_{S_0}}{V_{P_0}}\right)^3 \sin^2\theta - 2\left(\frac{V_{S_0}}{V_{P_0}}\right)^2 \sin^2\theta\right] a_{VS}^2 \\
&+ \left[\frac{1}{4} - \frac{1}{4}\left(\frac{V_{S_0}}{V_{P_0}}\right)\sin^2\theta - \left(\frac{V_{S_0}}{V_{P_0}}\right)^2 \sin^2\theta + \left(\frac{V_{S_0}}{V_{P_0}}\right)^3 \sin^2\theta\right] a_\rho^2 \\
&+ \left[2\left(\frac{V_{S_0}}{V_{P_0}}\right)^3 \sin^2\theta - \left(\frac{V_{S_0}}{V_{P_0}}\right)^2 \sin^2\theta\right] a_\rho a_{VS} \\
&+ \left[2\left(\frac{V_{S_0}}{V_{P_0}}\right)^3 \sin^2\theta - 2\left(\frac{V_{S_0}}{V_{P_0}}\right)^2 \sin^2\theta\right] a_{VS} b_{VS} \\
&+ \left[\frac{1}{4}\sin^2\theta\right] a_{VP} b_{VP} + \left[2\left(\frac{V_{S_0}}{V_{P_0}}\right)^3 \sin^2\theta - \left(\frac{V_{S_0}}{V_{P_0}}\right)^2 \sin^2\theta\right] b_\rho a_{VS} \\
&+ \left[2\left(\frac{V_{S_0}}{V_{P_0}}\right)^3 \sin^2\theta - \left(\frac{V_{S_0}}{V_{P_0}}\right)^2 \sin^2\theta\right] a_\rho b_{VS} \\
&+ \left[2\left(\frac{V_{S_0}}{V_{P_0}}\right)^3 \sin^2\theta - \frac{1}{2}\left(\frac{V_{S_0}}{V_{P_0}}\right)\sin^2\theta\right] b_\rho a_\rho
\end{aligned} \tag{3.14}$$

This expansion in scalar form shown by Innanen et al. (2014) to be equivalent to a full wave, nonlinear scattering model of the time-lapse difference wavefield, for the special case of a single immobile interface. The third order terms in the difference data are provided in Appendix A.

3.1.3 Numerical examples for P-P data

In this section, we examine the derived linear and nonlinear difference time-lapse AVO terms qualitatively with numerical examples. In the first example, the data used by Landrø (2001) are used. The reflection coefficient curves are compared over the whole angle range using the exact solution with Zoeppritz matrix for the baseline survey, monitor survey and their differences or difference data in Figure 3.3 a. The focus of this study is in approximating the difference data (red curve) for small angles or near offset (as the expansion series are

a) b)

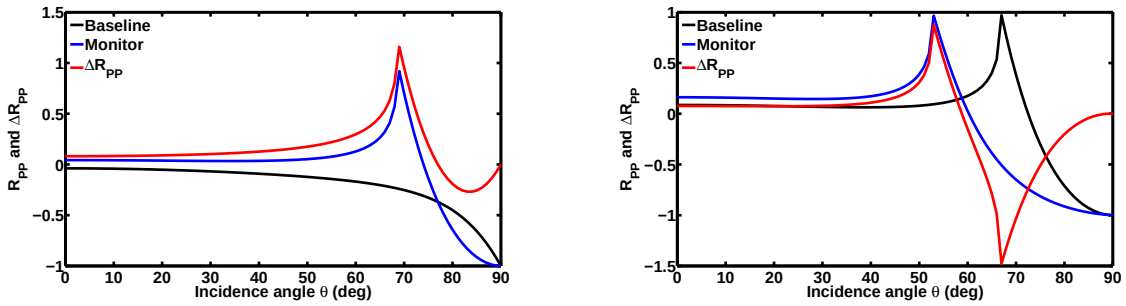

Figure 3.3: Reflection coefficient for the baseline survey, monitor survey, and their difference: a) Data used by Landrø (2001), Elastic incidence parameters: $V_{P0} = 2000m/s$, $V_{S0} = 1000m/s$ and $\rho_0 = 2.000g/cc$; baseline parameters:$V_{P_b} = 1900m/s$, $V_{S_b} = 1100m/s$ and $\rho_b = 1.950g/cc$; monitor parameters:$V_{P_m} = 2147m/s$, $V_{S_m} = 1078m/s$ and $\rho_m = 2.030g/cc$. b) Data used by Veire et al. (2006), Elastic incidence parameters: $V_{P0} = 1900m/s$, $V_{S0} = 995m/s$ and $\rho_0 = 1.95g/cc$; baseline parameters:$V_{P_b} = 2066m/s$, $V_{S_b} = 1075m/s$ and $\rho_b = 2.1300g/cc$; monitor parameters:$V_{P_m} = 2384m/s$, $V_{S_m} = 1193m/s$ and $\rho_m = 2.156g/cc$.

truncated after second order in $\sin\theta$). Typical values for P-wave and S-wave velocities and density for the cap rock and reservoir (preproduction and post production), which are the same as Gullfaks 4D project, are used. In the Gullfaks field, there are +13 %, -2 %, and +4 % changes in the reservoir in P-wave and S-wave velocities and density respectively due to the production.

The exact difference data are compared with our derived linear and higher order approximations in Figure 3.4. Results are also compared for the higher contrast in seismic parameters in the reservoir after the production. The second and third approximations are in better agreement with the exact difference data, especially for angles below the critical angle which correspond to the range used in this study.

For the second example, we used data by Veire et al. (2006). The reflection coefficient curves are compared over the whole angle range using the exact solution with Zoeppritz matrix for the baseline survey, monitor survey and their differences or difference data in Figure 3.3 b. Veire used two synthetic models for the reservoir: a baseline scenario with a

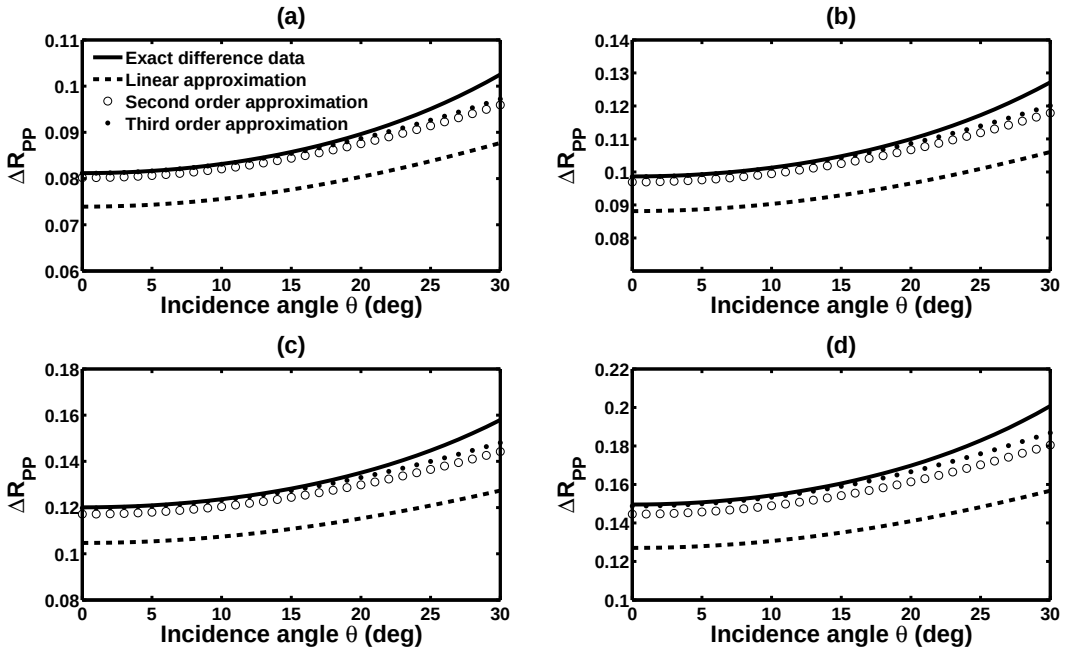

Figure 3.4: ΔR_{PP} for the exact, linear, second order, and third order approximation with elastic parameters as in Figure 3.3 a. Solid line: Exact difference data, - - -: Linear approximation, ooo: Second order approximation, and ...: Third order approximation.
a) +13 %, -2 %, and +4 % changes in P-wave and S-wave velocities and density respectively in the reservoir after production. b) +16 %, -3 %, and +5 % changes in P-wave and S-wave velocities and density respectively in the reservoir after production. c) +20 %, -4 %, and +6 % changes in P-wave and S-wave velocities and density respectively in the reservoir after production. d) +25 %, -6 %, and +8 % changes in P-wave and S-wave velocities and density respectively in the reservoir after production.

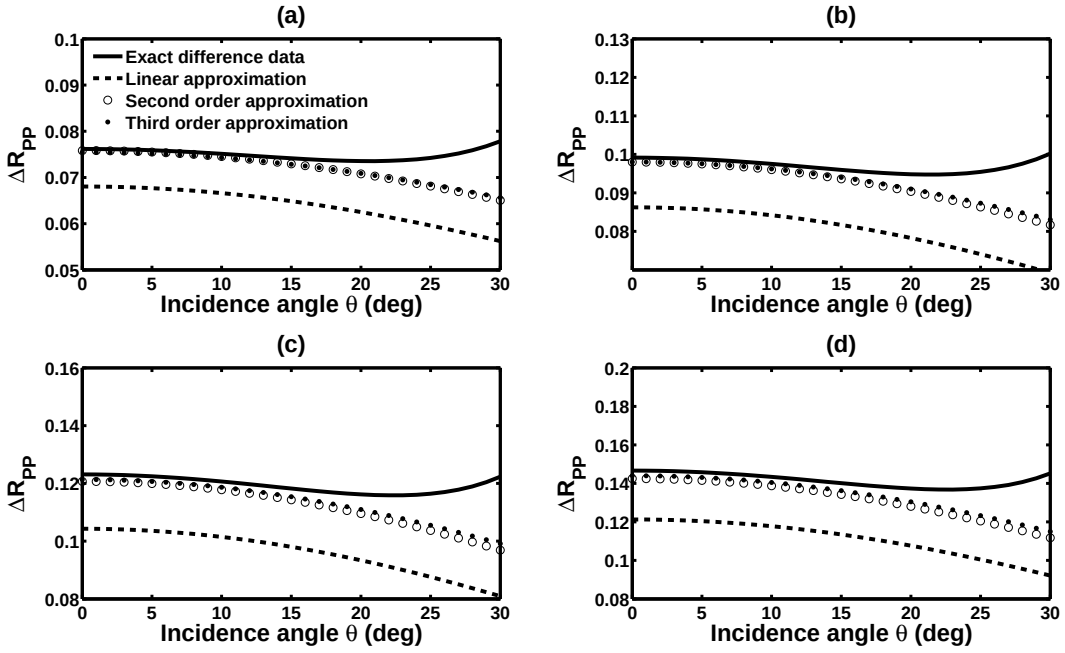

Figure 3.5: ΔR_{PP} for the exact, linear, second order, and third order approximation with elastic parameters as in Figure 3.3 b. Solid line: Exact difference data, - - -: Linear approximation, ooo: Second order approximation, and ...: Third order approximation.
a) +15 %, +11 %, and +1 % changes in P-wave and S-wave velocities and density respectively in the reservoir after production. b) +20 %, +15 %, and +2 % changes in P-wave and S-wave velocities and density respectively in the reservoir after production. c) +25 %, +20 %, and +3 % changes in P-wave and S-wave velocities and density respectively in the reservoir after production. d) +30 %, +25 %, and +4 % changes in P-wave and S-wave velocities and density respectively in the reservoir after production.

water saturation of 10 % and an effective pressure of 2 MPa . In the monitor survey, the water saturation and effective pressure are 50 % and 8 MPa respectively. These changes altered the seismic parameters and caused 15 %, 11 %, and 1 % increases, respectively in P-wave and S-wave velocities and density. We examined our formulation and compared them with the exact difference data not only for these changes, but also for higher contrasts for small angles or near offset (Figure 3.5). The second and third order time-lapse AVO approximations are in better agreement with the exact difference data, especially for higher contrasts in seismic parameters.

3.2 Time-lapse difference data for shear waves

We will again consider two seismic experiments involved in a time-lapse survey, a baseline survey followed by a monitoring survey, as in Figure 3.1. An S-wave is impinging on the boundary of a planar interface between the two elastic media (Figure 3.6). Amplitudes of reflected and transmitted S-waves are calculated through setting the boundary conditions in the Zoeppritz equations, which can be rearranged in matrix form e.g.:

$$S \equiv \begin{bmatrix} \sin\phi & -\sqrt{1-(B^{-1})^2\sin^2\phi} \\ -\sqrt{1-\sin^2\phi} & -B^{-1}\sin\phi \\ -2\sin\phi\sqrt{1-\sin^2\phi} & B^{-1}(1-2\sin^2\phi) \\ 1-2\sin^2\phi & 2\sin\phi\sqrt{1-(B^{-1})^2\sin^2\phi} \end{bmatrix}$$

$$\begin{bmatrix} F_x\sin\phi & -\sqrt{1-E_x^2\sin^2\phi} \\ \sqrt{1-F_x^2\sin^2\phi} & E_x\sin\phi \\ 2A_xF_x^2\sin\phi\sqrt{1-F_x^2\sin^2\phi} & -A_xE_x(1-2F_x^2\sin^2\phi) \\ A_xF_x(1-2F_x^2\sin^2\phi) & 2A_xF_x^2\sin\phi\sqrt{1-E_x^2\sin^2\phi} \end{bmatrix} \tag{3.15}$$

where ϕ is the S-wave incident angle; A_x, B^{-1}, E_x, F_x are the ratio of elastic parameters given in equation 3.3, and

$$c_S \equiv \begin{bmatrix} \sin\phi \\ \sqrt{1-\sin^2\phi} \\ 2\sin\phi\sqrt{1-\sin^2\phi} \\ 1-2\sin^2\phi \end{bmatrix}. \tag{3.16}$$

Reflection coefficients are determined through forming a further auxiliary matrices S_S by replacing the first column of S with c_S :

$$R_{SS}(\phi) = \frac{det(S_S)}{det(S)}. \tag{3.17}$$

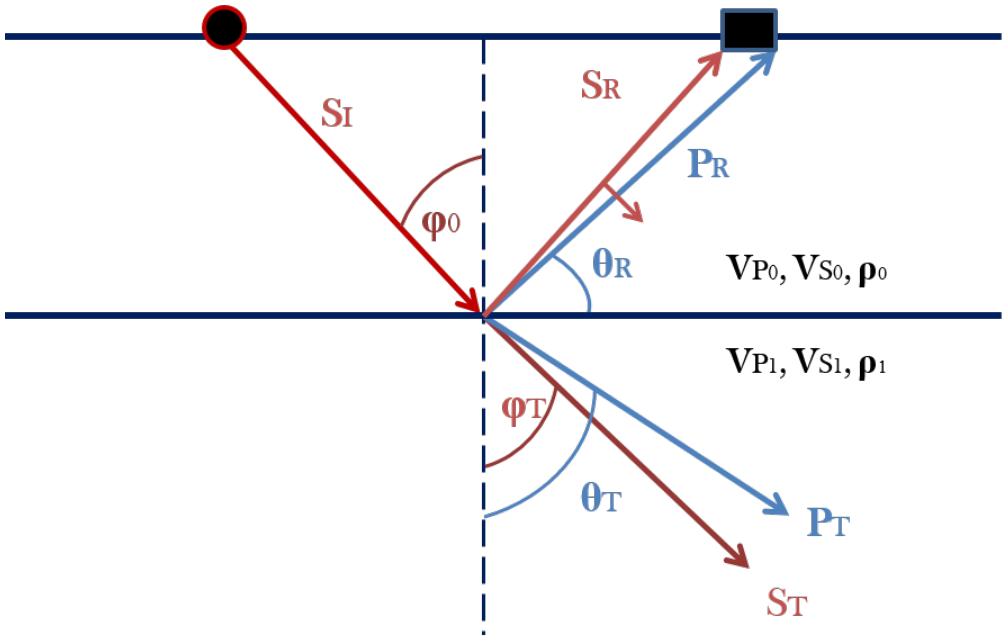

Figure 3.6: Displacement amplitude of an incident S-wave with related reflected and transmitted P and S waves.

R_{SS} for the baseline and monitor surveys are calculated using the same method. Rock properties for the cap rock are the same, but reservoir properties change to V_{Pm}, V_{Sm}, ρ_m from the time of the baseline survey to the monitor survey. The exact $R_{SS}(\theta)$ for both surveys are organized into terms which are the first, second, etc. order in any of perturbation parameters:

$$R_{SS}(\theta) = R_{SS}^{(1)}(\theta) + R_{SS}^{(2)}(\theta) + ... \tag{3.18}$$

The results for the baseline survey for shear waves, down going S-wave and upcoming S-wave, are:

$$\begin{aligned} R_{SS}^{(1)}(\phi) &= \left[\frac{1}{4}\left(7\sin^2\phi - 1\right)\right] b_{VS} + \left[\frac{1}{2}\left(4\sin^2\phi - 1\right)\right] b_\rho \\ R_{SS}^{(2)}(\phi) &= \left[\left(\frac{7}{4} - \frac{V_{S_0}}{V_{P_0}}\right)\sin^2\phi - \frac{1}{8}\right] b_{VS}^2 + \left[\left(1 + \left(\frac{1}{4}\right)\frac{V_{P_0}}{V_{S_0}} - \frac{V_{S_0}}{V_{P_0}}\right)\sin^2\phi - \frac{1}{4}\right] b_\rho^2 \\ &\quad + \left[\left(1 - 2\frac{V_{S_0}}{V_{P_0}}\right)\sin^2\phi\right] b_{VS} b_\rho. \end{aligned} \tag{3.19}$$

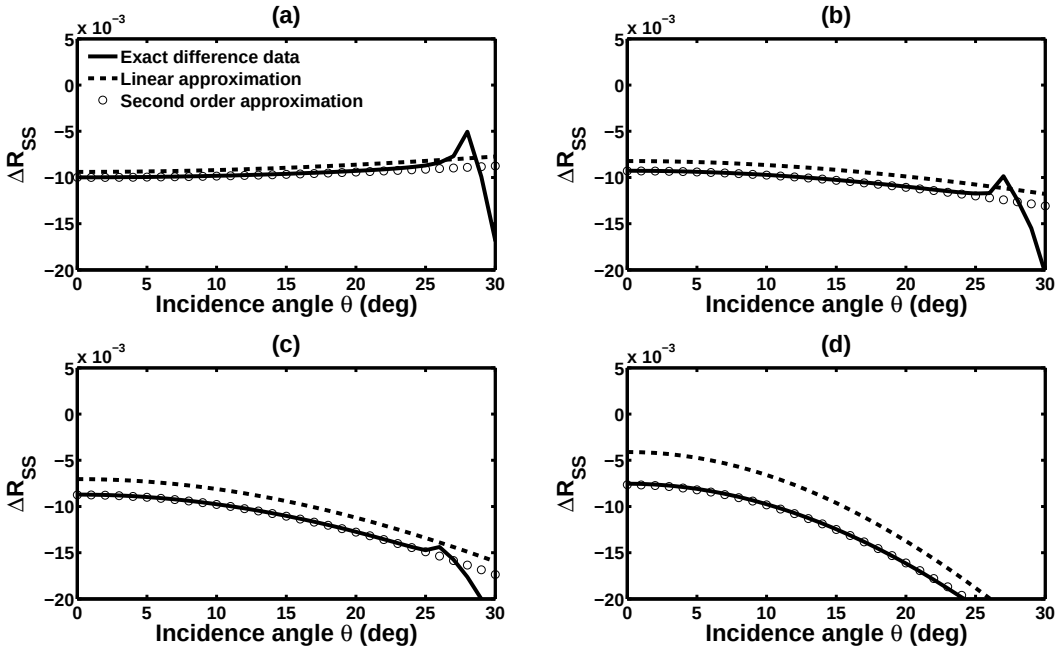

Figure 3.7: ΔR_{SS} for the exact, linear, and second order with elastic parameters as in Figure 3.3 a. Solid line: Exact difference data, - - -: Linear approximation, and ooo: Second order approximation.
a) +13 %, -2 %, and +4 % changes in P-wave and S-wave velocities and density respectively in the reservoir after production. b) +16 %, -3 %, and +5 % changes in P-wave and S-wave velocities and density respectively in the reservoir after production. c) +20 %, -4 %, and +6 % changes in P-wave and S-wave velocities and density respectively in the reservoir after production. d) +25 %, -6 %, and +8 % changes in P-wave and S-wave velocities and density respectively in the reservoir after production.

The difference data reflection coefficients between the baseline and monitor survey are then calculated as:

$$\Delta R_{SS}(\phi) = R^m_{SS}(\phi) - R^b_{SS}(\phi). \tag{3.20}$$

Elastic parameters may be re-defined in terms of perturbations in P-wave and S-wave velocities and the densities described in equation 3.7. These forms are substituted into matrix S and vector c_S; and the determinants and determinations in equation 3.17 are

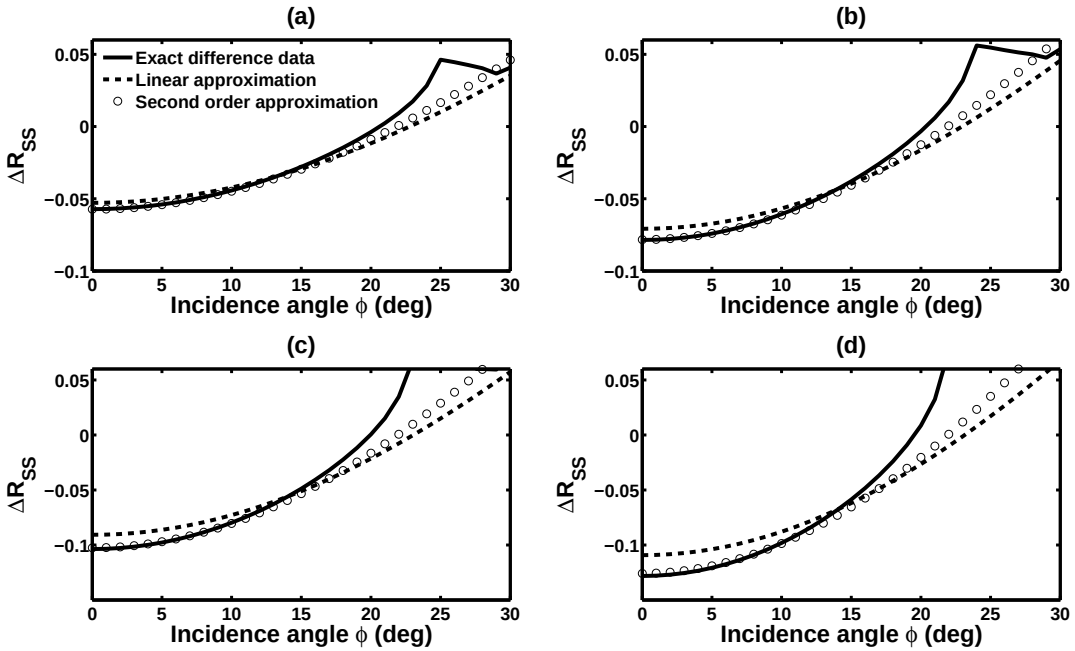

Figure 3.8: ΔR_{SS} for the exact, linear, and second order, with elastic parameters as in Figure 3.3 b. Solid line: Exact difference data, - - -: Linear approximation, and ooo: Second order approximation.
a) +15 %, +11 %, and +1 % changes in P-wave and S-wave velocities and density respectively in the reservoir after production. b) +20 %, +15 %, and +2 % changes in P-wave and S-wave velocities and density respectively in the reservoir after production. c) +25 %, +20 %, and +3 % changes in P-wave and S-wave velocities and density respectively in the reservoir after production. d) +30 %, +25 %, and +4 % changes in P-wave and S-wave velocities and density respectively in the reservoir after production.

expanded in orders of all six perturbation parameters and $\sin^2\phi$.

$$\Delta R_{SS}(\phi) = \Delta R_{SS}^{(1)}(\phi) + \Delta R_{SS}^{(2)}(\phi) + \Delta R_{SS}^{(3)}(\phi) + \dots \ . \tag{3.21}$$

$\Delta R_{SS}(\phi)$ for the first and second orders for shear waves are:

$$\begin{aligned}
\Delta R_{SS}^{(1)}(\phi) &= \left[\frac{1}{4}\left(7\sin^2\phi - 1\right)\right] a_{VS} + \left[\frac{1}{2}\left(4\sin^2\phi - 1\right)\right] a_{\rho} \\
\Delta R_{SS}^{(2)}(\phi) &= \left[\left(\frac{7}{4} - \frac{V_{S_0}}{V_{P_0}}\right)\sin^2\phi - \frac{1}{8}\right] a_{VS}^2 + \left[\left(1 + \left(\frac{1}{4}\right)\frac{V_{P_0}}{V_{S_0}} - \frac{V_{S_0}}{V_{P_0}}\right)\sin^2\phi - \frac{1}{4}\right] a_{\rho}^2 \\
&\quad + \left[\left(1 - 2\frac{V_{S_0}}{V_{P_0}}\right)\sin^2\phi\right](a_{VS}a_{\rho} + a_{VS}b_{\rho} + b_{VS}a_{\rho}) \\
&\quad + \left[\left(\frac{7}{4} - 2\frac{V_{S_0}}{V_{P_0}}\right)\sin^2\phi\right](a_{VS}b_{VS}) + \left[\left(\left(\frac{1}{2}\right)\frac{V_{P_0}}{V_{S_0}} - 2\frac{V_{S_0}}{V_{P_0}}\right)\sin^2\phi\right](a_{\rho}b_{\rho})
\end{aligned} \tag{3.22}$$

$\Delta R_{SS}(\phi)$ for the third order is presented in Appendix B.

3.2.1 Numerical examples for shear waves

We examine the derived linear and non linear difference time-lapse AVO terms for shear waves qualitatively with the same numerical examples used in section 3.1.3. We examined our formulation not only for these changes, but also for higher contrasts (Figure 3.7 and Figure 3.8). The second order time-lapse AVO approximation is in a better agreement with the exact difference data, especially for higher contrasts in seismic parameters. The convergence properties of ΔR_{SS} appear to be less straightforward than those of ΔR_{PP} approximations especially for the third order approximations, and the study of them is ongoing which will confirm after this thesis.

3.3 Time-lapse difference data for converted waves

We calculate reflection coefficient for both types of converted waves, either a reflected S-wave from an incident P-wave or a reflected P-wave from an incident S-wave. We use Matrix P in equation 3.2 to calculate R_{PS} and matrix S in equation 3.15 to calculate R_{SP}. Reflection coefficients then, are determined by forming an auxiliary matrix P_{PS} by

replacing the second columns of P with b_P , and then forming another auxiliary matrix S_{SP} by replacing the second columns of S with c_S:

$$R_{PS}(\theta) = \frac{det(P_{PS})}{det(P)} \quad R_{PS}(\phi) = \frac{det(S_{SP})}{det(S)}. \tag{3.23}$$

R_{PS} and R_{SP} for the baseline and monitor surveys are calculated using methods in section 3.1 and section 3.2. The difference data reflection coefficients between the baseline and monitor survey are calculated as:

$$\begin{aligned} \Delta R_{PS}(\theta) =& R^m_{PS}(\theta) - R^b_{PS}(\theta) \\ \Delta R_{SP}(\phi) =& R^m_{SP}(\phi) - R^b_{SP}(\phi). \end{aligned} \tag{3.24}$$

Organizing the solutions into terms which are the first, second, etc. order of any of perturbation parameters, p_ρ, p_{VP} and p_{VS} leads to:

$$\begin{aligned} R_{PS}(\theta) &= R^{(1)}_{PS}(\theta) + R^{(2)}_{PS}(\theta) + ... \\ R_{SP}(\theta) &= R^{(1)}_{SP}(\theta) + R^{(2)}_{SP}(\theta) + ... \ . \end{aligned} \tag{3.25}$$

The linear and second order terms for time-lapse difference data for a down going p-wave and upcoming S-wave are:

$$\begin{aligned} \Delta R^{(1)}_{PS}(\theta) =& \left[-\frac{V_{S_0}}{V_{P_0}}\sin\theta\right] a_{VS} + \left[-\frac{1}{2}\left(2\frac{V_{S_0}}{V_{P_0}} + 1\right)\sin\theta\right] a_\rho \\ \Delta R^{(2)}_{PS}(\theta) =& \left[-\frac{3}{4}\frac{V_{S_0}}{V_{P_0}}\sin\theta\right] a^2_{VS} + \left[-\frac{1}{2}\sin\theta\right] a^2_\rho + \left[\frac{1}{2}\left(2\frac{V_{S_0}}{V_{P_0}} - 1\right)\sin\theta\right] b_\rho a_\rho \\ &+ \left[-\frac{1}{2}\frac{V_{S_0}}{V_{P_0}}\sin\theta\right] b_{VS} a_{VS} + \left[\frac{1}{4}\frac{V_{S_0}}{V_{P_0}}\sin\theta\right] (a_{Vp} a_{VS} + a_{Vp} b_{VS} + b_{Vp} a_{VS}) \\ &+ \left[\frac{1}{8}\left(2\frac{V_{S_0}}{V_{P_0}} - 1\right)\sin\theta\right] (a_{Vp} a_\rho + b_\rho a_{Vp} + a_\rho b_{Vp} + a_\rho a_{VS} + a_\rho b_{VS} + b_\rho a_{VS}). \end{aligned} \tag{3.26}$$

The linear and second order terms for time-lapse difference data for a down going S-wave and upcoming P-wave are:

$$\begin{aligned}
\Delta R^{(1)}_{SP}(\phi) &= \left[-\frac{V_{S_0}}{V_{P_0}}\sin\phi\right] a_{VS} + \left[-\frac{1}{2}\left(2\frac{V_{S_0}}{V_{P_0}}+1\right)\sin\phi\right] a_\rho \\
\Delta R^{(2)}_{SP}(\phi) &= \left[-\left(\frac{3}{4}\right)\frac{V_{S_0}}{V_{P_0}}\sin\phi\right] a^2_{VS} + \left[-\frac{1}{2}\sin\phi\right] a^2_\rho + \left[\frac{1}{2}\left(2\frac{V_{S_0}}{V_{P_0}}-1\right)\sin\phi\right] b_\rho a_\rho \\
&\quad + \left[-\left(\frac{1}{2}\right)\frac{V_{S_0}}{V_{P_0}}\sin\phi\right] b_{VS} a_{VS} + \left[\left(\frac{1}{4}\right)\frac{V_{S_0}}{V_{P_0}}\sin\phi\right] (a_{VP}a_{VS} + a_{Vp}b_{VS} + b_{Vp}a_{VS}) \\
&\quad + \left[\frac{1}{8}\left(2\frac{V_{S_0}}{V_{P_0}}-1\right)\sin\phi\right] (a_{Vp}a_\rho + b_\rho a_{Vp} + a_\rho b_{Vp} + a_\rho a_{VS} + a_\rho b_{VS} + b_\rho a_{VS}).
\end{aligned} \tag{3.27}$$

$\Delta R_{PS}(\theta)$ and $\Delta R_{SP}(\phi)$ are similar as it can be seen from equation 3.26 and equation 3.27. $\Delta R_{PS}(\theta)$ and $\Delta R_{SP}(\phi)$ for the third order approximation are different as it is expected and they are presented in Appendix C.

3.3.1 Numerical examples for converted waves

We examine our linear and nonlinear time-lapse difference AVO terms for converted waves qualitatively with the same numerical examples used in this chapter (Figure 3.9 - Figure 3.12). For converted waves using these data set, all three approximation are following almost the same trend. The convergence properties of ΔR_{SP} appear to be less straightforward than those of ΔR_{PP} and ΔR_{PS} approximations especially for the third order approximations.

3.4 Reduction to Landrø

The result for the linear term are compared to the the difference data reflection coefficient derived by Landrø (2001). The difference data reflection coefficient in Landrø's paper is:

$$\Delta R_{PP}(\theta) = \frac{1}{2}\left(\frac{\Delta\rho}{\rho}+\frac{\Delta V_P}{V_P}\right) - 2\frac{V_S^2}{V_P^2}\left(\frac{\Delta\rho}{\rho}+2\frac{\Delta V_S}{V_S}\right)\sin^2\theta + \frac{\Delta V_P}{2V_P}\tan^2\theta. \tag{3.28}$$

This equation can be rearranged as:

$$\Delta R_{PP}(\theta) = \frac{1}{2}(1+\tan^2\theta)(\frac{\Delta V_P}{V_P}) + (-\frac{4V_S^2}{V_P^2})\sin^2\theta(\frac{\Delta V_S}{V_S}) + (\frac{1}{2} - \frac{2V_S^2}{V_P^2}\sin^2\theta)(\frac{\Delta\rho}{\rho}). \tag{3.29}$$

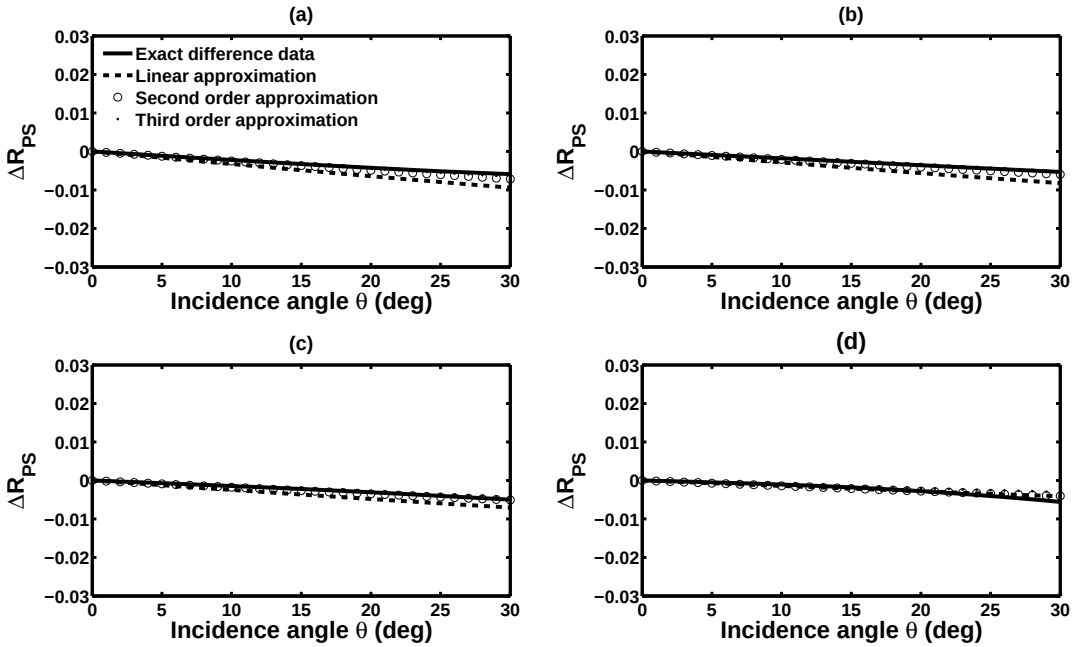

Figure 3.9: ΔR_{PS} for the exact, linear, second order, and third order approximation with elastic parameters as in Figure 3.3 a. Solid line: Exact difference data, - - -: Linear approximation, ooo: Second order approximation, and ...: Third order approximation.
a) +13 %, -2 %, and +4 % changes in P-wave and S-wave velocities and density respectively in the reservoir after production. b) +16 %, -3 %, and +5 % changes in P-wave and S-wave velocities and density respectively in the reservoir after production. c) +20 %, -4 %, and +6 % changes in P-wave and S-wave velocities and density respectively in the reservoir after production. d) +25 %, -6 %, and +8 % changes in P-wave and S-wave velocities and density respectively in the reservoir after production.

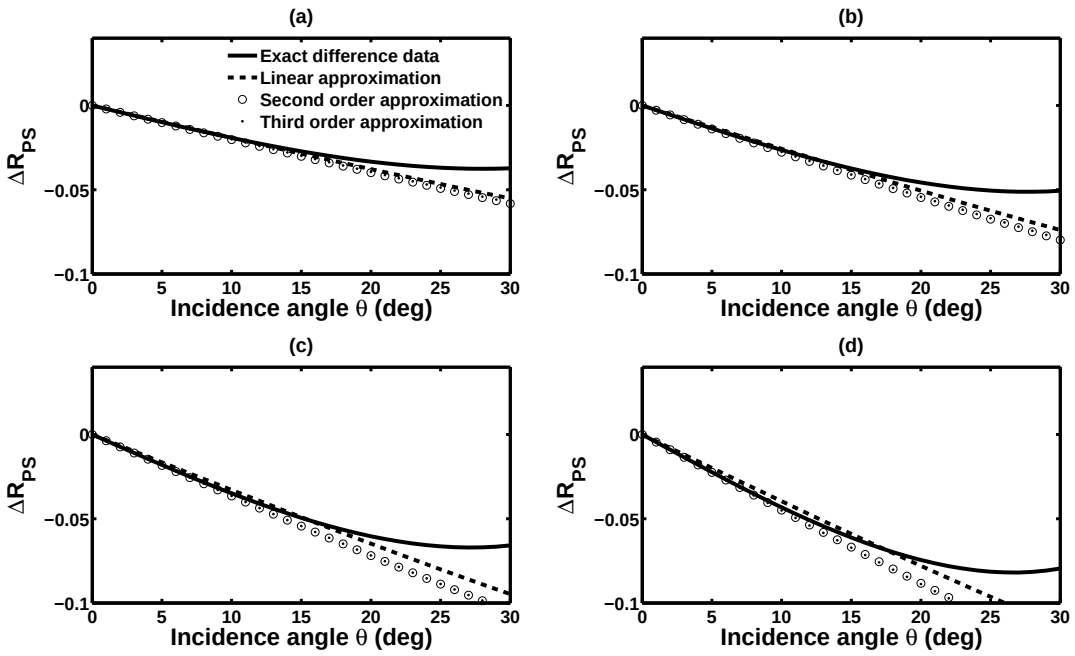

Figure 3.10: ΔR_{PS} for the exact, linear, second order, and third order approximation with elastic parameters as in Figure 3.3 b. Solid line: Exact difference data, - - -: Linear approximation, ooo: Second order approximation, and ...: Third order approximation.
a) +15 %, +11 %, and +1 % changes in P-wave and S-wave velocities and density respectively in the reservoir after production. b) +20 %, +15 %, and +2 % changes in P-wave and S-wave velocities and density respectively in the reservoir after production. c) +25 %, +20 %, and +3 % changes in P-wave and S-wave velocities and density respectively in the reservoir after production. d) +30 %, +25 %, and +4 % changes in P-wave and S-wave velocities and density respectively in the reservoir after production.

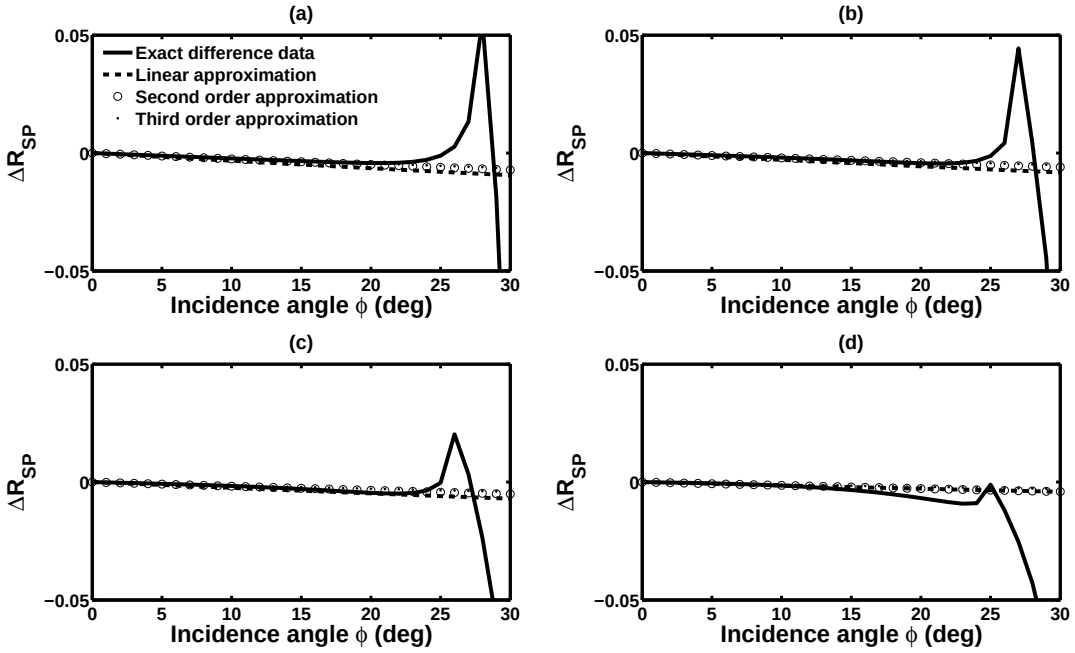

Figure 3.11: ΔR_{SP} for the exact, linear, second order, and third order approximation with elastic parameters as in Figure 3.3 a. Solid line: Exact difference data, - - -: Linear approximation, ooo: Second order approximation, and ...: Third order approximation.
a) +13 %, -2 %, and +4 % changes in P-wave and S-wave velocities and density respectively in the reservoir after production. b) +16 %, -3 %, and +5 % changes in P-wave and S-wave velocities and density respectively in the reservoir after production. c) +20 %, -4 %, and +6 % changes in P-wave and S-wave velocities and density respectively in the reservoir after production. d) +25 %, -6 %, and +8 % changes in P-wave and S-wave velocities and density respectively in the reservoir after production.

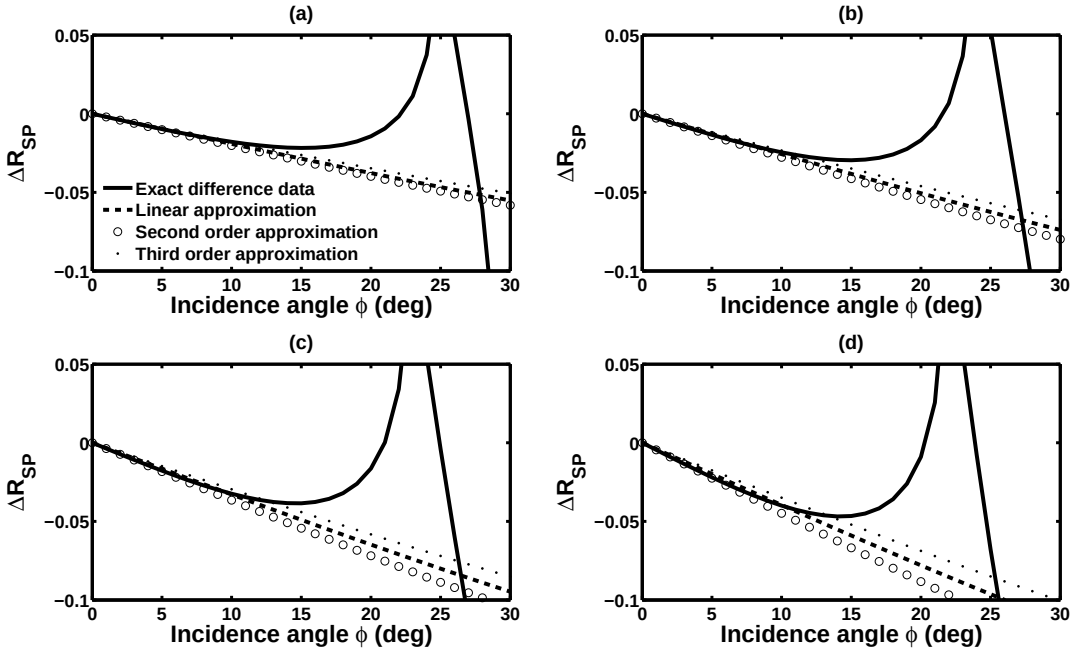

Figure 3.12: ΔR_{SP} for the exact, linear, second order, and third order approximation with elastic parameters as in Figure 3.3 b. Solid line: Exact difference data, - - -: Linear approximation, ooo: Second order approximation, and ...: Third order approximation.
a) +15 %, +11 %, and +1 % changes in P-wave and S-wave velocities and density respectively in the reservoir after production. b) +20 %, +15 %, and +2 % changes in P-wave and S-wave velocities and density respectively in the reservoir after production. c) +25 %, +20 %, and +3 % changes in P-wave and S-wave velocities and density respectively in the reservoir after production. d) +30 %, +25 %, and +4 % changes in P-wave and S-wave velocities and density respectively in the reservoir after production.

For small θ:

$$1+\sin^2\theta = 1+\sin^2\theta+\sin^4\theta = 1+\sin^2\theta(1+\sin^2\theta) \sim 1+\frac{\sin^2\theta}{\cos^2\theta} = 1+\tan^2\theta. \quad (3.30)$$

Here we used this approximation:

$$\frac{1}{\cos^2\theta} = \frac{1}{1-\sin^2\theta} \sim 1+\sin^2\theta. \quad (3.31)$$

Substituting $X=\sin\theta$ and $B=\frac{V_S^2}{V_P^2}$ leads to:

$$\Delta R_{PP}(\theta) = \frac{1}{2}(1+X^2)(\frac{\Delta V_P}{V_P}) + (-4B^2X^2)(\frac{\Delta V_S}{V_S}) + (\frac{1}{2}-2B^2X^2)(\frac{\Delta\rho}{\rho}). \quad (3.32)$$

Considering:

$$\begin{aligned}
a_{VP} &= 1-\frac{V_{P_{BL}}^2}{V_{P_M^2}} = \frac{V_{P_M}^2-V_{P_{BL}}^2}{V_{P_M}^2} = \left(\frac{V_{P_M}+V_{P_{BL}}}{V_{P_M}}\right)\times\left(\frac{V_{P_M}-V_{P_{BL}}}{V_{P_M}}\right) \\
&\sim 2\times\left(\frac{V_{P_M}-V_{P_{BL}}}{V_{P_M}}\right) \sim 2\times\frac{\Delta V_P}{V_P} \\
a_{VS} &= 1-\frac{V_{S_{BL}}^2}{V_{S_M^2}} = \frac{V_{S_M}^2-V_{S_{BL}}^2}{V_{S_M}^2} = \left(\frac{V_{S_M}+V_{S_{BL}}}{V_{S_M}}\right)\times\left(\frac{V_{S_M}-V_{S_{BL}}}{V_{S_M}}\right) \\
&\sim 2\times\left(\frac{V_{S_M}-V_{S_{BL}}}{V_{S_M}}\right) \sim 2\times\frac{\Delta V_S}{V_S} \\
a_\rho &= 1-\frac{\rho_{BL}}{\rho_M} = \frac{\rho_M-\rho_{BL}}{\rho_M} = \frac{\Delta\rho}{\rho}.
\end{aligned} \quad (3.33)$$

The first part of equation 3.14 is equivalent to the equation 3.29, which shows the agreement of our linear approximation for the difference data with the one derived by Landrø (2001):

$$\begin{aligned}
\Delta R_{PP}^{(1)}(\theta_0) &= (\frac{1}{4}+\frac{1}{4}X^2)a_{VP} + (-2B^2X^2)a_{VS} + (\frac{1}{2}-2B^2X^2)a_\rho \\
&= (\frac{1}{4}+\frac{1}{4}X^2)(2\times\frac{\Delta V_P}{V_P}) + (-2B^2X^2)(2\times\frac{\Delta V_S}{V_S}) + (\frac{1}{2}-2B^2X^2)\frac{\Delta\rho}{\rho} \\
&= \frac{1}{2}\left(\frac{\Delta\rho}{\rho}+\frac{\Delta V_P}{V_P}\right) - \frac{2V_S^2}{V_P^2}\left(\frac{\Delta\rho}{\rho}+2\frac{\Delta V_S}{V_S}\right)\sin^2\theta + \frac{\Delta V_P}{2V_P}\tan^2\theta.
\end{aligned} \quad (3.34)$$

3.5 Coupling between baseline and time-lapse relative changes

The linear and higher order approximation solutions for ΔR_{PP}, ΔR_{SS}, ΔR_{PS}, and ΔR_{SP} are presented as expansions of the perturbation parameters in the previous sections in this

chapter. Here, we will compute time-lapse difference data in terms of relative changes in seismic parameters, $\frac{\Delta V_P}{V_P}$, $\frac{\Delta V_S}{V_S}$, and $\frac{\Delta \rho}{\rho}$, because this choice permits quantitative comparison with other studies in the literature, and furthermore because expressing the AVO response in order of relative changes may improve convergence properties (Innanen, 2013). We designate the capital delta symbol to indicate the relative changes in seismic parameters for the physical contrast between the cap rock and reservoir in the baseline survey. To represent changes in the seismic parameters due to time-lapse variations in the reservoir, we use a small delta symbol. The relative changes in the baseline survey are defined as follows:

$$\begin{aligned}
\frac{\Delta V_P}{V_P} =& 2 \times \frac{V_{Pb} - V_{P0}}{V_{Pb} + V_{P0}}, \\
\frac{\Delta V_S}{V_S} =& 2 \times \frac{V_{Sb} - V_{S0}}{V_{Sb} + V_{S0}}, \\
\frac{\Delta \rho}{\rho} =& 2 \times \frac{\rho_b - \rho_0}{\rho_b + \rho_0},
\end{aligned} \tag{3.35}$$

while time-lapse perturbations are defined as :

$$\begin{aligned}
\frac{\delta V_P}{V_P} =& 2 \times \frac{V_{Pm} - V_{Pb}}{V_{Pm} + V_{Pb}}, \\
\frac{\delta V_S}{V_S} =& 2 \times \frac{V_{Sm} - V_{Sb}}{V_{Sm} + V_{Sb}}, \\
\frac{\delta \rho}{\rho} =& 2 \times \frac{\rho_m - \rho_b}{\rho_m + \rho_b}.
\end{aligned} \tag{3.36}$$

To express our linear and higher order time-lapse differences in terms of relative changes, we expand b_{VP}, b_{VS}, b_ρ, and a_{VP}, a_{VS}, a_ρ in terms of the appropriate series of relative changes as:

$$\begin{aligned}
b_{VP} =& 2\left(\frac{\Delta V_P}{V_P}\right) - 2\left(\frac{\Delta V_P}{V_P}\right)^2 + \frac{3}{2}\left(\frac{\Delta V_P}{V_P}\right)^3 - ... \\
b_{VS} =& 2\left(\frac{\Delta V_S}{V_S}\right) - 2\left(\frac{\Delta V_S}{V_S}\right)^2 + \frac{3}{2}\left(\frac{\Delta V_S}{V_S}\right)^3 - ... \\
b_\rho =& \left(\frac{\Delta \rho}{\rho}\right) - \frac{1}{2}\left(\frac{\Delta \rho}{\rho}\right)^2 + \frac{1}{4}\left(\frac{\Delta \rho}{\rho}\right)^3 + ...,
\end{aligned} \tag{3.37}$$

and

$$\begin{aligned} a_{VP} =& 2\left(\frac{\delta V_P}{V_P}\right) - 2\left(\frac{\delta V_P}{V_P}\right)^2 + \frac{3}{2}\left(\frac{\delta V_P}{V_P}\right)^3 - ... \\ a_{VS} =& 2\left(\frac{\delta V_S}{V_S}\right) - 2\left(\frac{\delta V_S}{V_S}\right)^2 + \frac{3}{2}\left(\frac{\delta V_S}{V_S}\right)^3 - ... \\ a_{\rho} =& \frac{\delta\rho}{\rho} - \frac{1}{2}\frac{\delta\rho}{\rho}^2 + \frac{1}{4}\frac{\delta\rho}{\rho}^3 + ... \ . \end{aligned} \tag{3.38}$$

Substituting equation 3.37 and equation 3.38 into equation 3.14 and linearizing, $\Delta R_{PP}(\theta) \sim \Delta R^{(1)}_{PP}(\theta)$, and assuming small angles $\sin^2\theta \ll 1$, we recover Landrø's equation for approximation of the difference reflection data (the process explained in section 3.4):

$$\Delta R_{PP}(\theta) \sim \Delta R^{(1)}_{PP}(\theta) = \frac{1}{2}\left(\frac{\delta\rho}{\rho} + \frac{\delta V_P}{V_P}\right) - \sin^2\theta \frac{2V_S^2}{V_P^2}\left(\frac{\delta\rho}{\rho} + 2\frac{\delta V_S}{V_S}\right) + \frac{\delta V_P}{2V_P}\sin^2\theta. \tag{3.39}$$

The second order term of the difference reflection data in terms of relative parameters is derived with small angles assumption. Substituting equation 3.37 and equation 3.38 into the second part in equation 3.14 and considering only second order terms, we have:

$$\begin{aligned} \Delta R^{(2)}_{PP}(\theta) =& \Gamma_{\delta V_P}\left(\frac{\delta V_P}{V_P}\right)^2 + \Gamma_{\delta V_S}\left(\frac{\delta V_S}{V_S}\right)^2 + \Gamma_{\delta\rho}\left(\frac{\delta\rho}{\rho}\right)^2 + \Gamma_{\delta\rho\delta V_S}\left(\frac{\delta\rho}{\rho}\right)\left(\frac{\delta V_S}{V_S}\right) \\ &+ \Gamma_{\Delta V_S\delta V_S}\left(\frac{\Delta V_S}{V_S}\right)\left(\frac{\delta V_S}{V_S}\right) + \Gamma_{\Delta V_P\delta V_P}\left(\frac{\Delta V_P}{V_P}\right)\left(\frac{\delta V_S}{V_S}\right) \\ &+ \Gamma_{\Delta\rho\delta V_S}\left(\frac{\Delta\rho}{\rho}\right)\left(\frac{\delta V_S}{V_S}\right) + \Gamma_{\Delta V_S\delta\rho}\left(\frac{\Delta V_S}{V_S}\right)\left(\frac{\delta\rho}{\rho}\right) + \Gamma_{\Delta\rho\delta\rho}\left(\frac{\Delta\rho}{\rho}\right)\left(\frac{\delta\rho}{\rho}\right), \end{aligned} \tag{3.40}$$

where

$$
\begin{aligned}
\Gamma_{\delta V_P} &= \frac{1}{2} + \sin^2\theta \\
\Gamma_{\delta V_S} &= 4\left[\left(\frac{V_{S_0}}{V_{P_0}}\right)^3 \sin^2\theta - 2\left(\frac{V_{S_0}}{V_{P_0}}\right)^2 \sin^2\theta\right] \\
\Gamma_{\delta\rho} &= \left(\frac{V_{S_0}}{V_{P_0}}\right)^3 \sin^2\theta - \left(\frac{V_{S_0}}{V_{P_0}}\right)^2 \sin^2\theta \\
&\quad - \frac{1}{4}\left(\frac{V_{S_0}}{V_{P_0}}\right) \sin^2\theta + \frac{1}{4} \\
\Gamma_{\delta\rho\delta V_S} &= 2\left[2\left(\frac{V_{S_0}}{V_{P_0}}\right)^3 \sin^2\theta - \left(\frac{V_{S_0}}{V_{P_0}}\right)^2 \sin^2\theta\right] \\
\Gamma_{\Delta V_S\delta V_S} &= 8\left[\left(\frac{V_{S_0}}{V_{P_0}}\right)^3 \sin^2\theta - \left(\frac{V_{S_0}}{V_{P_0}}\right)^2 \sin^2\theta\right] \\
\Gamma_{\Delta V_P\delta V_P} &= \sin^2\theta \\
\Gamma_{\Delta\rho\delta V_S} &= 2\left(\frac{V_{S_0}}{V_{P_0}}\right)^3 \sin^2\theta - \left(\frac{V_{S_0}}{V_{P_0}}\right)^2 \sin^2\theta \\
\Gamma_{\Delta V_S\delta\rho} &= 2\left[2\left(\frac{V_{S_0}}{V_{P_0}}\right)^3 \sin^2\theta - \left(\frac{V_{S_0}}{V_{P_0}}\right)^2 \sin^2\theta\right] \\
\Gamma_{\Delta\rho\delta\rho} &= 2\left(\frac{V_{S_0}}{V_{P_0}}\right)^3 \sin^2\theta - \frac{1}{2}\left(\frac{V_{S_0}}{V_{P_0}}\right) \sin^2\theta.
\end{aligned}
\tag{3.41}
$$

The third order term is also derived in terms of relative parameters in Appendix A. Higher order approximations not only add terms including higher order relative changes in the baseline and time-lapse, but also add terms which include coupling between the baseline and time-lapse relative changes as in equation 3.40.

The linear order term for ΔR_{SS}, ΔR_{PS}, and ΔR_{SP} in terms of relative changes in seismic parameters assuming small angles such that $\sin^2\theta \ll 1$ and $\sin^2\phi \ll 1$, can be derived using the same process explained for PP data. Substituting equation 3.37 and equation 3.38 into the first part in equations 3.22, 3.26, 3.27 respectively and truncating after the first order

in relative changes in P- and S- wave velocities and density, we have:

$$\begin{aligned}
\Delta R_{SS}(\phi) \sim \Delta R_{SS}^{(1)}(\phi) =& \frac{1}{2}\left(7\sin^2\phi - 1\right)\frac{\delta V_S}{V_S} + \frac{1}{2}\left(4\sin^2\phi - 1\right)\frac{\delta\rho}{\rho} \\
\Delta R_{PS}(\theta) \sim \Delta R_{PS}^{(1)}(\theta) =& \left(-2\frac{V_S}{V_P}\sin\theta\right)\frac{\delta V_S}{V_S} - \frac{1}{2}\left(2\frac{V_S}{V_P} + 1\right)\sin\theta\frac{\delta\rho}{\rho} \\
\Delta R_{SP}(\phi) \sim \Delta R_{SP}^{(1)}(\phi) =& \left(-2\frac{V_S}{V_P}\sin\phi\right)\frac{\delta V_S}{V_S} - \frac{1}{2}\left(2\frac{V_S}{V_P} + 1\right)\sin\phi\frac{\delta\rho}{\rho}.
\end{aligned} \tag{3.42}$$

Chapter 4

A physical modelling study of time-lapse AVO

Physical modelling can be used to validate the reflectivity predicted with different theoretical methods. Physical modelling of geophysical data provides physical property distributions of the Earth which are simpler than the real Earth, and the degree of simplification depends upon the geometry used for the data acquisition. In 1D models, the physical properties are assumed to vary only in depth. In 2D models, the physical properties vary in depth and the direction parallel to a survey line. In 3D modelling, properties vary in all three directions. Rods (for 1D) and elastic plates (for 2D and 3D), have been used to perform experiments. Recently, application of dynamic sandbox has provided experiments to simulate specific geologic problems (Berryman et al., 1958; Purnell, 1986; Wandler et al., 2006).

In this chapter, the validation of the linear and higher order terms calculated for difference time-lapse data for P-P data which are described in the previous chapter, are investigated on a physical model. A physical model experiment is acquired simulating two surveys in a time-lapse problem. 3D seismic surveys resembling baseline and monitor surveys are modelled with the University of Calgary Seismic Physical Modelling Facility. The baseline survey is modelled with plexiglas (acrylic) and PVC (Polyvinyl chloride) slabs resembling the cap rock and reservoir at the time of the baseline survey. The PVC slab is replaced with a phenolic slab for the monitor survey in which the reservoir had been undergone geological-geophysical changes during the time. Picked amplitudes from plexiglas-PVC and plexiglas-phenolic (along the direction of the isotropic plane for phenolic) interfaces are corrected for geometrical spreading, emergence angle, free surface, transmission loss, and radiation patterns. The results for the baseline survey data, the monitor survey data, and their

difference representing the difference data in time-lapse study are analyzed. The derived linear and higher order approximations for difference data are compared with the model data for validation. The results of this chapter are published in the Geophysics journal (Jabbari et al., 2015).

4.1 Data acquisition

The University of Calgary Seismic Physical Modelling Facility (Wong et al., 2009) was used to conduct the experiment. Elastic waves were generated and detected by arrays of small transducers which were mounted on a gantry. These transducers were moved with a six-axes positioning system using linear electric motors to accomplish a 2D seismic survey over a model with a volume of $1000 \times 800 \times 600$ mm^3 which scales up to a real-world survey with a volume of $10 \times 8 \times 6$ km^3. In our seismic physical modelling, we use a scale factor of 10,000, so that a modelling time of 0.1 microsecond represents a seismic-scale time of 1 millisecond, a modelling frequency 1 MHz represents a seismic frequency of 100Hz, and a modelling dimension of 1 millimeter represents a geological dimension of 10 m. The transducers produced dominant frequencies in the range of 100 kHz to 500 kHz that scaled down to real-world values of 10 to 50 Hz. Under this scaling, material velocities and densities remain the same for both the physical model and the geological world.

The model contains water and blocks of different material defining an Earth model. The C++ acquisition software runs on Java on an MS Windows PC. Dynasen CA-1136 piezoelectric transducers were used as sources and detectors to emit and detect P waves. Common midpoint (CMP) gathers are recorded as SEG-Y files (Figure 4.1).

Figure 4.2 shows the experimental setup for our measurements. Two seismic experiments which are involved in a time-lapse survey, the baseline survey, followed by a monitoring survey, were modelled. The baseline survey was run on a plexiglas (acrylic) block atop of a PVC (Polyvinyl chloride) block, both of which were immersed in water. The monitoring

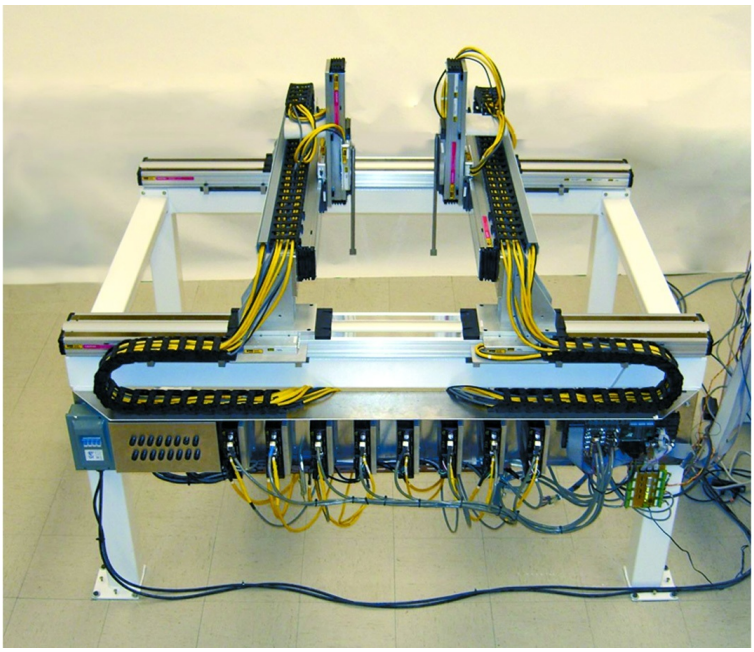

Figure 4.1: The six-axes 3D positioning system (-/+ X is left/right, -/+ Y is towards/away, -/+ Z is up/down). Gantry A is to the left; Gantry B is to the right (Wong et al., 2009)

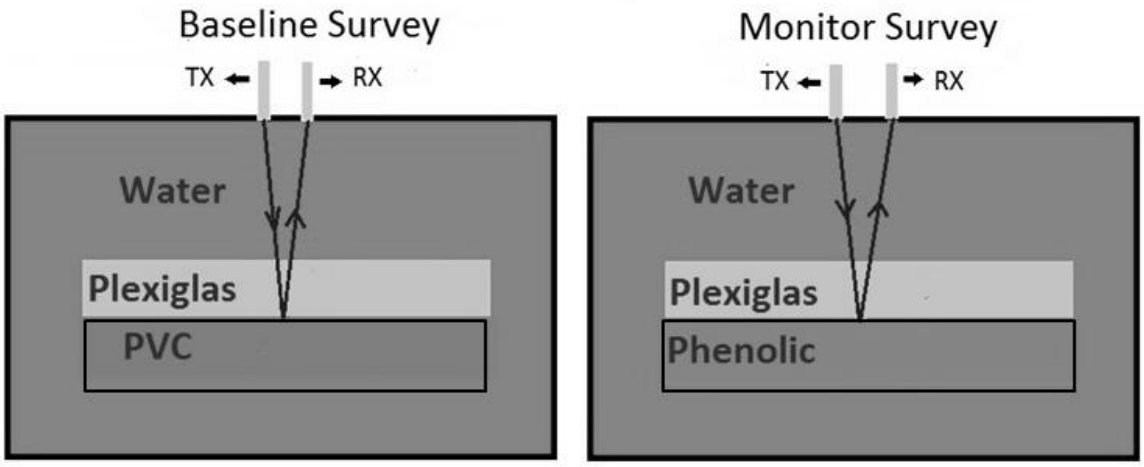

Figure 4.2: Acquiring CMP data over an plexiglas, PVC, and phenolic slabs for baseline and monitor surveys. Elastic incidence parameters; Plexiglas (acrylic): $V_P = 2745m/s$, $V_S = 1380m/s$ and $\rho = 1.19g/cc$; PVC: $V_P = 2350m/s$, $V_S = 1120m/s$ and $\rho = 1.30g/cc$; Phenolic: $V_P = 3570m/s$, $V_S = 1730m/s$ and $\rho = 1.39g/cc$.

survey was conducted with the PVC block replaced by a phenolic block. The plexiglas block represents the cap rock, and the PVC and phenolic blocks represent the reservoir rock in the baseline and monitor surveys. The thickness of water, plexiglas, and PVC in the baseline survey experiment are 80.0, 25.6, 24.5 mm which represent a real-world survey of 800, 256, 245 m respectively. The thickness of water, plexiglas, and Phenolic in the monitor survey experiment are 80.0, 50.8, 69.0 mm which represent a real-world survey of 800, 508, and 690 m respectively. Several common-mid-point (CMP) reflection gathers were acquired for several offsets. All the arrivals relevant to the AVO analysis occur before the arrival time of the first water bottom multiple. Diffractions from the edges of the model certainly do exist, as well as reflections from the sides of the water tank containing the model. However, the arrival times of these events are much later than the events of interest, and lie outside the range of recorded times. The PP amplitudes were picked at the plexiglas-PVC interface for the baseline survey and at the plexiglas-phenolic interface for the monitor survey.

To avoid surface waves, the measurement were done in water. The dominant wavelength in the experiment is about 2.86 mm (corresponding to a dominant frequency of about 520 kHz in water with velocity equal to 1485 m/s). In the experiment, water ripples on the surface of the water are much less than 0.1 mm in amplitude; only about three percent of the wavelength. Although these ripples are comparatively very small, concern has been raised that they may still create deviations in the water-air reflection coefficient from the ideal value of -1, and thus affect the amplitudes of the waves impinging on the targets below. However, the experimental data are recorded after vertically stacking 400 repeated firings of the source with a repetition rate of 500 per second. Any P-wave amplitude variations caused by ripples are unsynchronized to the source firings, and so are "random" and are greatly reduced by stacking and waveform averaging.

The CMP gather for the both experiments, the baseline and monitor surveys are presented in Figure 4.3.

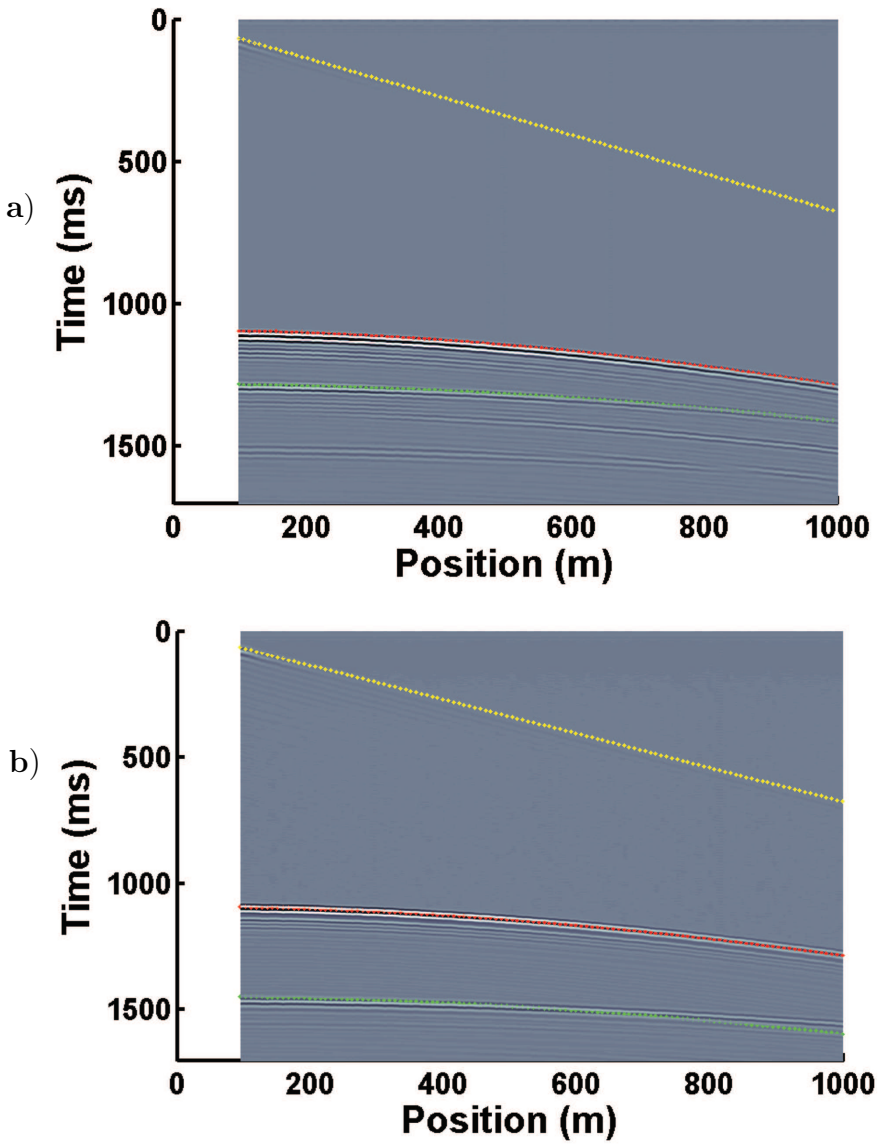

Figure 4.3: CMP gather for the measured simulated (**a**) baseline and (**b**) monitor experiments. Events indicated with "yellow" are the PP reflections from the top of the water, events "red" are the PP reflections from the top of plexiglas layer, and events "green" are the PP reflection from the top of the PVC for the baseline and the PP reflection from the top of phenolic along the direction of the isotropic plane for the monitor.

Figure 4.4 shows a CMP gathers of seismograms for the baseline and monitor experiments focused on the area of interest.

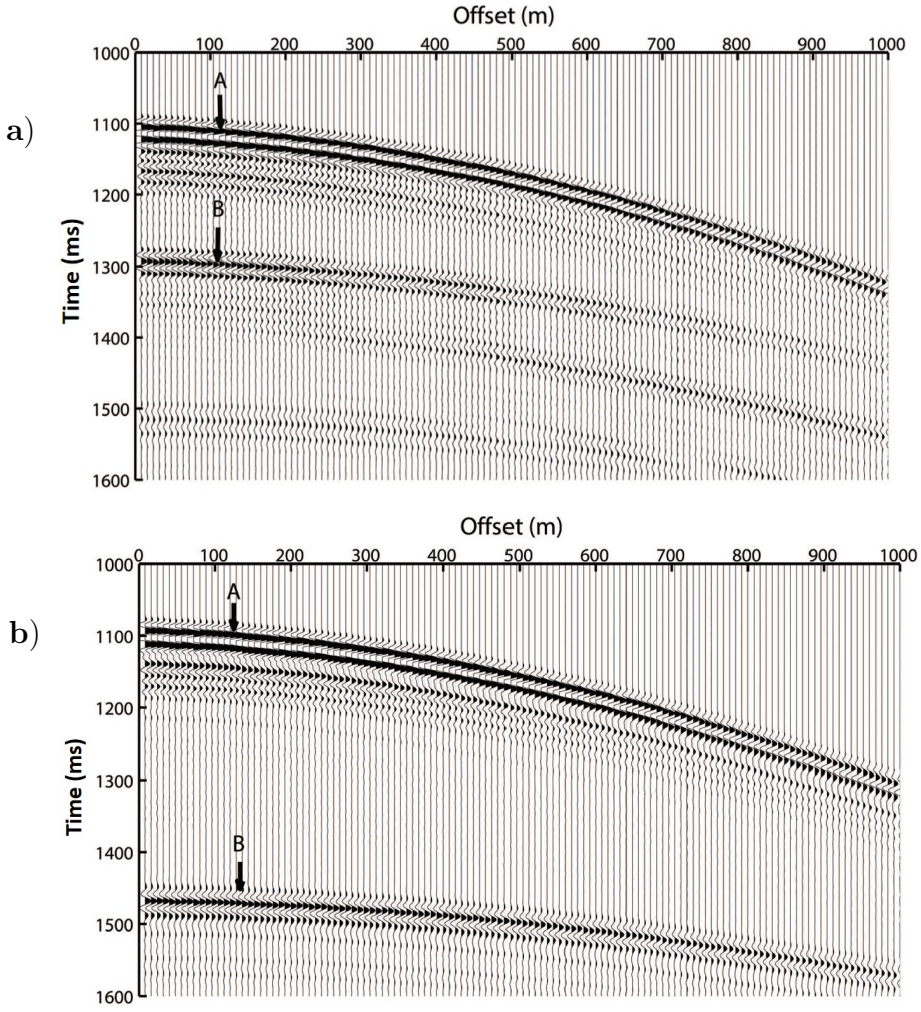

Figure 4.4: Trace-normalized plots for the measured simulated (**a**) baseline and (**b**) monitor experiments. Events indicated with "A" are the PP reflections from the top of plexiglas layer, and events "B" are the PP reflection from the top of the PVC for the baseline and the PP reflection from the top of phenolic along the direction of the isotropic plane for the monitor.

4.2 Amplitude pre-processing

Prior to any AVO analysis, amplitude information acquired by physical modelling must be corrected to compensate for various effects that can mask the AVO information. These effects

include geometrical spreading, transmission loss and overburden effects, multiple reflections, ground roll, source radiation pattern, and geophone response, and can be accounted for (Spratt et al., 1993).

Following the precessing procedure developed by Mahmoudian (2013), we corrected our measured reflected amplitude data for geometrical spreading, emergence angle, free surface, and transmission loss. The piezopin pin transducers produce vertical motion at the source and respond to vertical motion at the receiver. The vertically directed motion must be scaled to conform to the direction of plane wave propagation assumed in the Zoeppritz equations. This has been done by dividing measured amplitudes by the cosine of the propagation direction relative to vertical direction (Duren, 1992). The propagation direction at these locations is typically called the emergence angle. In the analysis of the physically- modelled data, the emergence angles are calculated via ray tracing from the source position to the receiver position through all the layers and using the angle final angle at the receiver. Accurate ray-tracing can be done since we know beforehand (within one or two percent) the P-wave velocities of all the materials used in the experiment. In industry practice, the emergence angle at the receiver is often approximated by using P-wave ray-tracing through only two layers, namely, an overlying layer based on an NMO P-wave velocity and the reflecting layer with a best estimate of its P-wave velocity. We also applied source-receiver directivity corrections to account for the radiation/reception patterns of disc-shaped piezoelectric transducers operating in an acoustic medium. Disc-shaped transducers of finite size do not act as point sources, but have a directivity given by:

$$D(\theta) = \frac{J_1(X)}{X}, \quad X = \frac{\pi d \sin(\theta) f_d}{V_W} \tag{4.1}$$

where θ is the angle between the perpendicular axis through the center of the disc, d is the disc diameter, f_d is the dominant frequency, V_W is the water velocity, J1 is the Bessel function of order 1 (Buddensiek et al., 2009). Figure 4.5 displays the directivity pattern common to both the source and receiver. By reciprocity, the source and receiver directivities

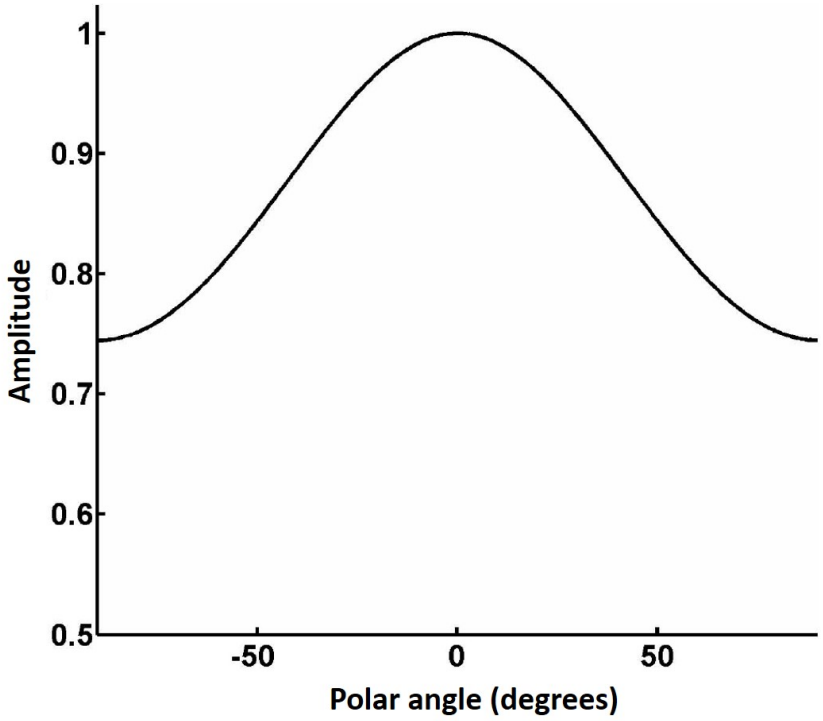

Figure 4.5: The directivity calculated using Equation 4.1, with d = 1.36 mm and $\lambda = \frac{f_d}{V_W}$ = 2.86 mm.

are identical, since the source and receiver transducers are physically identical. For our physical modelling, the disc diameter is 1.36 mm, the dominant frequency is 520 kHz, and the water velocity is 1485 m/s.

The reflection coefficient along the CMP at the interface of interest are derived applying the necessary corrections based on the following equation (Duren, 1992):

$$A(x,f) = \frac{SD(\theta_s,f)D(\theta_h,f)L(x)\cos\theta_h}{D_g(x)}R_T(\theta_T), \tag{4.2}$$

where f is the frequency, x is the source-receiver offset, θ_s is the source radiated ray direction, θ_h is the emergence angle at the receiver, θ_T is the incident angle at the target interface. A(x,f) is vertical-component recorded reflection amplitude, S is overall scalar related to source strength, $D(\theta_s, f)$ and $D(\theta_h, f)$ are source and receiver directivities respectively, $D_g(x)$ is geometrical spreading, $L(x)$ is transmission loss, and $R_T(\theta_T)$ is the reflection coefficient at the target interface.

4.2.1 Comparison of the formulated linear and higher order approximation difference data with physical model results

Figure 4.6 shows the physically-modelled reflection amplitude for the baseline and monitor surveys, corrected for geometrical spreading, emergence angle, free surface, transmission loss, and directivity. Also shown are the difference between the corrected baseline and monitor surveys. We note that the data in this figure indicate that an increase in amplitude occurs at about 50 degrees. This is consistent with expected critical angles based on Snell's Law with overlying Plexiglas velocity of 2745 m/s and underlying velocity of Phenolic of 3570 m/s.

Scaled-down physical modelling is done to provide "ground truth" for comparing with theoretical and numerical results. Field results from geological-scale measurements are often difficult to use for validating theoretical and numerical predictions because the variations in the geological-scale physical properties and geometry are uncontrolled and too complicated.

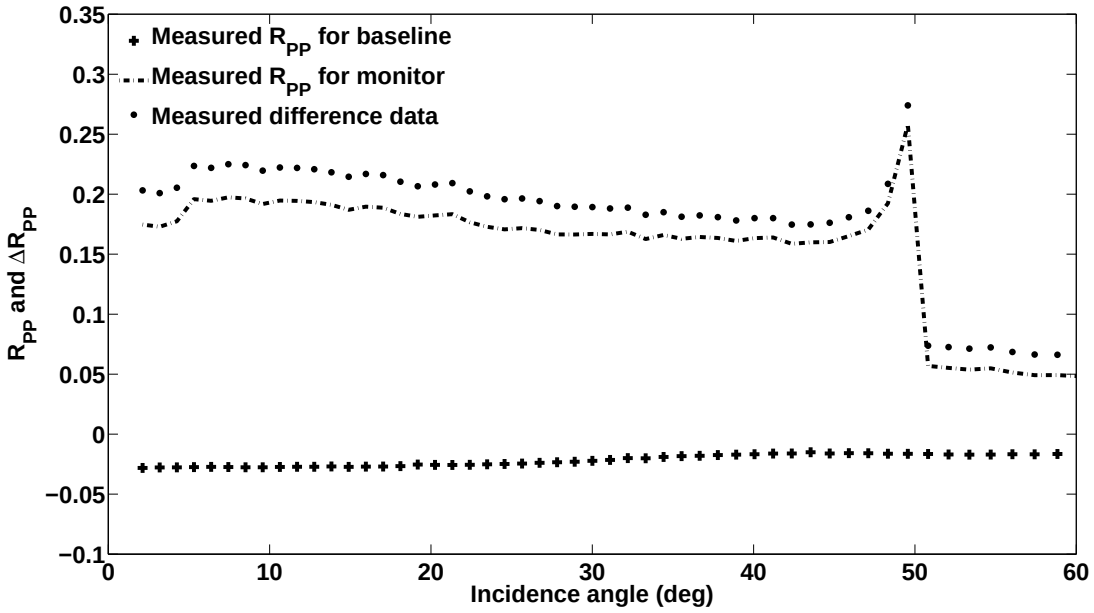

Figure 4.6: R_{PP} for the baseline (+), monitor (–), and ΔR_{PP} or difference data (dots) for the physical modelling data. Elastic incidence parameters: $V_{P0} = 2745m/s$, $V_{S0} = 1380m/s$ and $\rho_0 = 1.19g/cc$; baseline parameters:$V_{P_{BL}} = 2350m/s$, $V_{S_{BL}} = 1122m/s$ and $\rho_{BL} = 1.13g/cc$; monitor parameters:$V_{P_M} = 3570m/s$, $V_{S_M} = 1730m/s$ and $\rho_M = 1.39g/cc$.

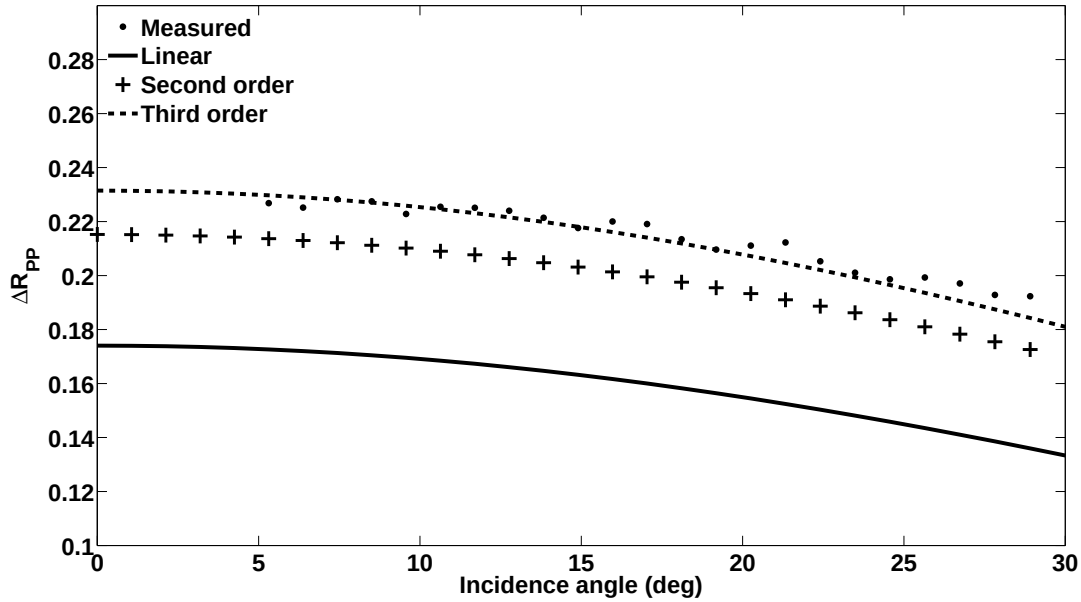

Figure 4.7: ΔR_{PP} for the physical modelling data (dots), linear (solid line), second order (+), and third order (–) approximation. Elastic incidence parameters: $V_{P0} = 2745m/s$, $V_{S0} = 1380m/s$ and $\rho_0 = 1.19g/cc$; baseline parameters:$V_{P_{BL}} = 2350m/s$, $V_{S_{BL}} = 1122m/s$ and $\rho_{BL} = 1.13g/cc$; monitor parameters:$V_{P_M} = 3570m/s$, $V_{S_M} = 1730m/s$ and $\rho_M = 1.39g/cc$.

Within limited ranges of property values and complexity of geometry, physical modelling, in which measurements are made on meter-scale models with known values of physical properties and simplified geometry, provides useful and meaningful data for validation. These data are in agreement with the exact reflection data for the baseline, monitor, and difference data calculated using Zoeppritz equations for angles smaller than the critical angle.

On Figure 4.7, the experimental ΔR_{PP} values are compared to calculated values based on the linear, second order, and third order expressions. The small fluctuations in the experimental ΔR_{PP} values from the physically-modelled seismograms are due to experimental errors associated with amplitude picking. In order to obtain an optimum fit to the experimental ΔR_{PP} values, the theoretical calculations on Figure 4.7 were done using small adjustments to the P and S velocity values for the plexiglas, PVC, and phenolic materials. These slight adjustments were kept within acceptable bounds (i.e., +/- 50 m/s), as established by independent measurements.

These results shows that the higher order approximations with the model data which emphasize including higher order terms for difference data calculations in time-lapse are more comparable.

Chapter 5

Field analysis of time-lapse AVO signatures

In this chapter, a multicomponent time-lapse seismic data set is used to validate the theoretical results for linear and nonlinear time-lapse AVO difference data for P-P data. This time-lapse data set was acquired during hydraulic fracturing of two horizontal wells in the unconventional Montney Reservoir at Pouce Coupe Field in the Peace River area by Talisman Energy Inc. part of Repsol Group.

5.1 Pouce Coupe time-lapse, Multicomponent Seismic Data

4D time-lapse, multicomponent seismic surveys were acquired by Talisman Energy Inc. at the Pouce Coupe Field, which is located on the border between Alberta and British Columbia in the Peace River area. The target formation in these seismic acquisitions was the Triassic Montney Siltstone reservoir (Figure 5.1).

The Montney Formation is composed of fine-grained, pseudo-turbidites proximal to shoreface deposition and is classified as an organic-rich argillaceous siltstone and sandstone package. Information obtained by Talisman Energy Inc. reports the Montney reservoir to have a matrix permeability of 0.01-.02 mD and porosity of 6-10 % within the Pouce Coupe Field. The unconventional Montney reservoir at Pouce Coupe contains tight gas siltstones and sandstones and produces both gas and liquid hydrocarbons. For economic production, enhanced permeability pathways of natural and induced fractures are required due to the tight nature of the Montney (Davies et al., 1997; Davey, 2012). The Montney Formation is subdivided, from its base, into units A, B, C, D, E and F. The Formation is overlain by the Doig Phosphate and underlain by the Permian Belloy (Figure 5.2).

The baseline survey, acquired in March 2008, was recorded after completion and stim-

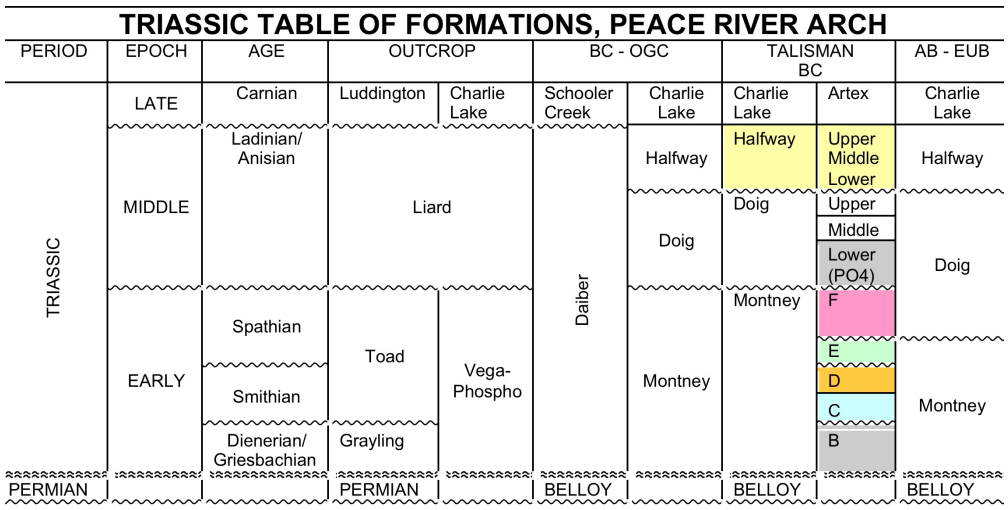

Figure 5.1: Triassic Montney Formation in the Peace River Arch region. Pouce Coupe Field is represented by the coloured Formations in the Repsol BC chart section (courtesy of Repsol S.A.).

ulation of the 102/07-07-78-10W6M well, but before production was initiated. The first monitor was acquired from December 8 to 10, 2008, after 8 months of Montney gas production from the 102/07-07-78-10W6M well. The purpose of acquiring this survey was to characterize the reservoir condition prior to hydraulically fracturing the two horizontal wells. For this reason we will refer to this survey as the baseline survey. The hydraulic fracture operations took place in two separate stages on the two horizontal wells, and another two subsequent monitor surveys were acquired after each fracture event. The second and third monitor surveys were acquired between December 13-14, after fracturing the horizontal well 102/02-07-078-10W6M (targeting the Lower Montney unit C) and between December 18-19, after fracturing the horizontal well 102/07-07-78-10W6M (targeting the lower Upper Montney unit D), respectively. We will consider these two monitors as monitor 1 and monitor 2 (Figure 5.3).

The seismic data were recorded by CGGVeritas with Megabin geometry on a patch of about 5 km^2 (1600 m by 3000 m) as in Figure 5.4.

The acquisition geometry consisted of a parallel Megabin arrangement with 9 East-West

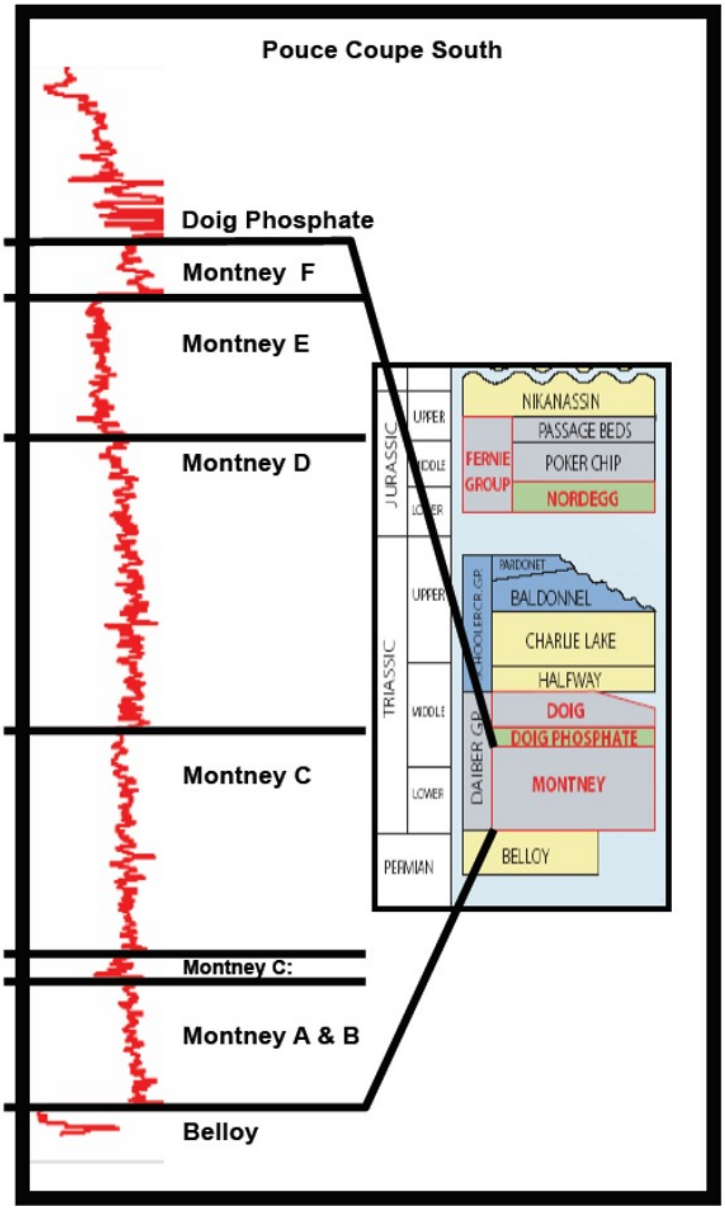

Figure 5.2: Type log of the Triassic Montney in the southern Pouce Coupe Field. Red curve is the gamma ray (Steinhoff, 2013).

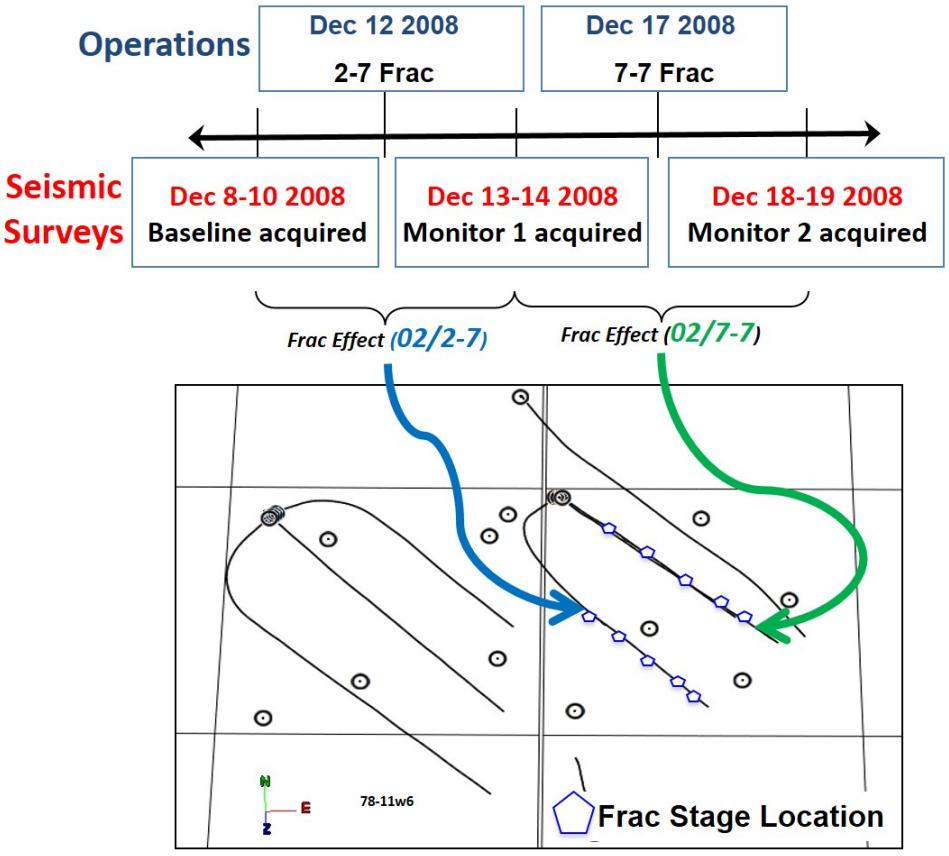

Figure 5.3: Pouce Coupe time-lapse seismic and field operations timeline. The map shows two horizontal wells hydraulically stimulated (2-07 well and 7-07 well) and the location of the vertical shear sonic log (13-12 well). Modified from Atkinson (2010).

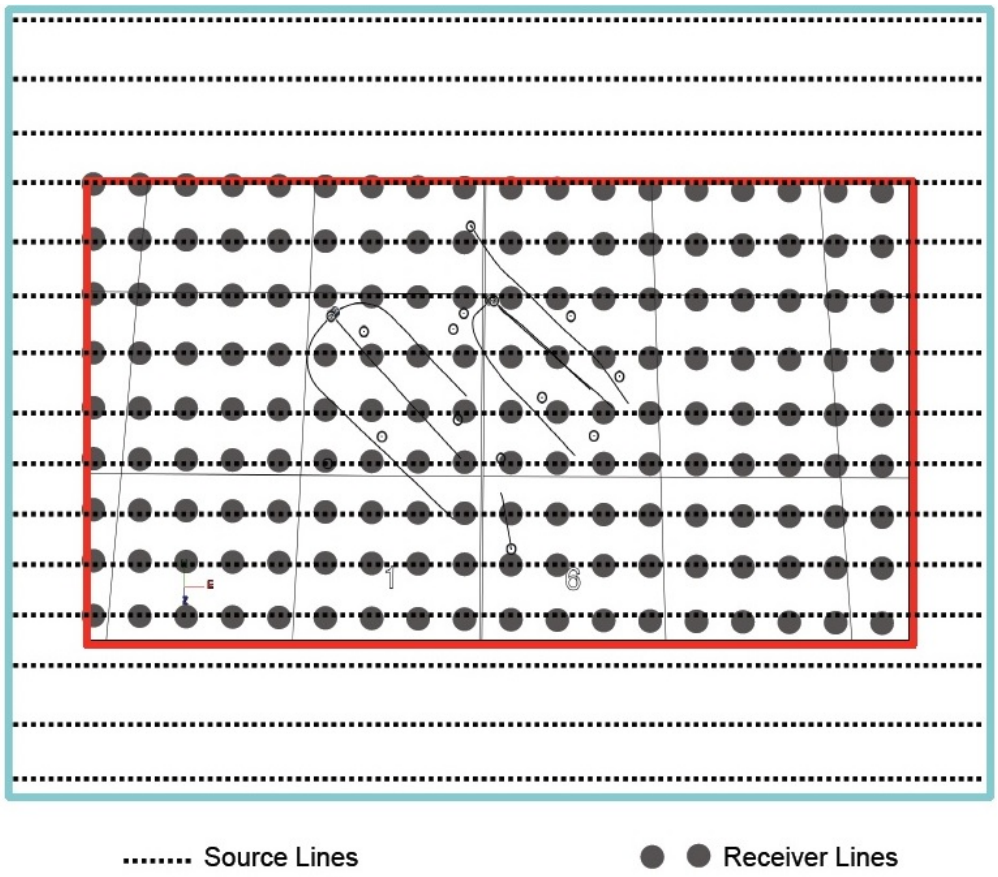

Figure 5.4: Pouce Coupe time-lapse, multicomponent seismic survey acquisition schematic layout. The resulting 1.6 km × 3 km patch is centered over horizontal wells 2-07 and 7-07. Modified from Atkinson (2010).

receiver lines at a line spacing of 200 m and a station spacing of 100 m for 31 three component receivers per line. These lines were collocated with source lines also in the East-West direction with the stations being interleaved, creating 50 m bin spacings in the East-West direction. The bin spacing in the North-South direction was 100 m; through f-x trace interpolation, the bin size was reduced to 50 m in the North-South direction. Two additional source lines were added to the North and South of the receiver layout at 400 m intervals. The source grid extended approximately 10 station intervals beyond the receiver layout. The recording length was 6 seconds with a sampling interval of 2 ms.

A result of the survey design was uniform 360° azimuth for different offset distribution which provides data for future AVO/AVAZ (amplitude variation with azimuth) analysis. The processing was completed by Sensor Geophysical Ltd. in July, 2013. The processing flow includes statics correction, prestack noise attenuation, surface consistent deconvolution, CMP (common mid point) stacking, f-k (frequency-wavenumber) filter, radon multiple and 2-term normal moveout. Subsequently, Sensor Geophysical Ltd reprocessed the data making use of a set of new methods to enhance time-lapse repeatability and improve prestack shear wave splitting analysis. Receiver Azimuth Detection and Rotation (RADAR) was utilized to detect and correct receiver azimuths, and this improved the quality of the subsequent steps of processing the horizontal receiver components (Grossman et al., 2013; Steinhoff, 2013). Further details of multicomponent processing are outlined in Steinhoff (2013).

To summarize the multicomponent surface Pouce Coupe seismic data set used in this study, includes a baseline survey with two subsequent monitor surveys, and the acquisition was designed to cover a full 360 degree azimuth and offset range from 50 to 4500 meters to a bin size of 50 m by 50 m.

5.1.1 Methodology

To correlate seismic character to subsurface geology and estimate the location of the horizons on the seismic sections, a synthetic seismogram was generated using a wavelet

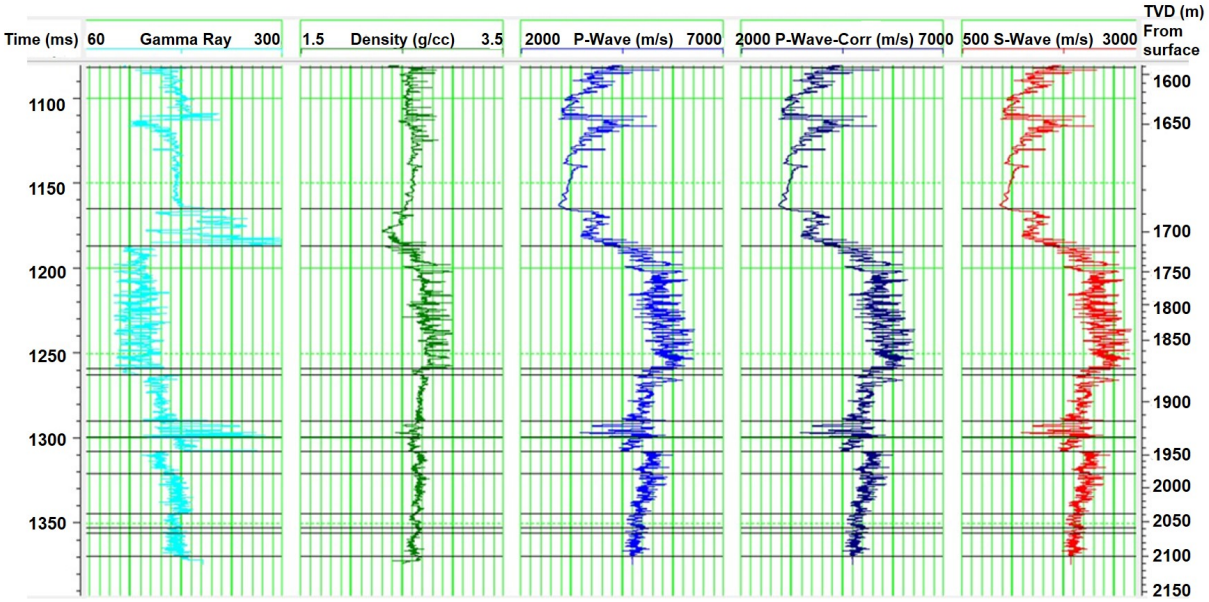

Figure 5.5: Gamma, P-wave, S-wave, and density logs for the horizontal well 102-02-07-078-10W6

extracted from the horizontal well, 102-02-07-078-10W6M, and reflectivity derived from P-wave sonic and density logs. The S-wave log is calculated using Castagna's Equation with parameters of $V_S = 0.8619V_P - 1172$ m/s (Castagna et al., 1985). Figure 5.5 shows different logs obtained by 102-02-07-078-10W6M well including the computed S-wave log and edited or corrected P-wave log used for the synthetic seismogram generation.

This synthetic seismic trace is aligned to the seismic section at the well location to relate horizon tops with specific reflections on the seismic section. Figure 5.6 shows the resultant well tie aligned with the baseline seismic section which allows us to correlate the Montney Formation to the seismic. From this estimation, amplitude versus offset analysis can be obtained.

The baseline seismic data were interpreted using the generated synthetic trace. The synthetic trace has been used to estimate the depth of different horizons, especially the target horizon, the tops of Montney C and D (Figure 5.7). The same method can be used

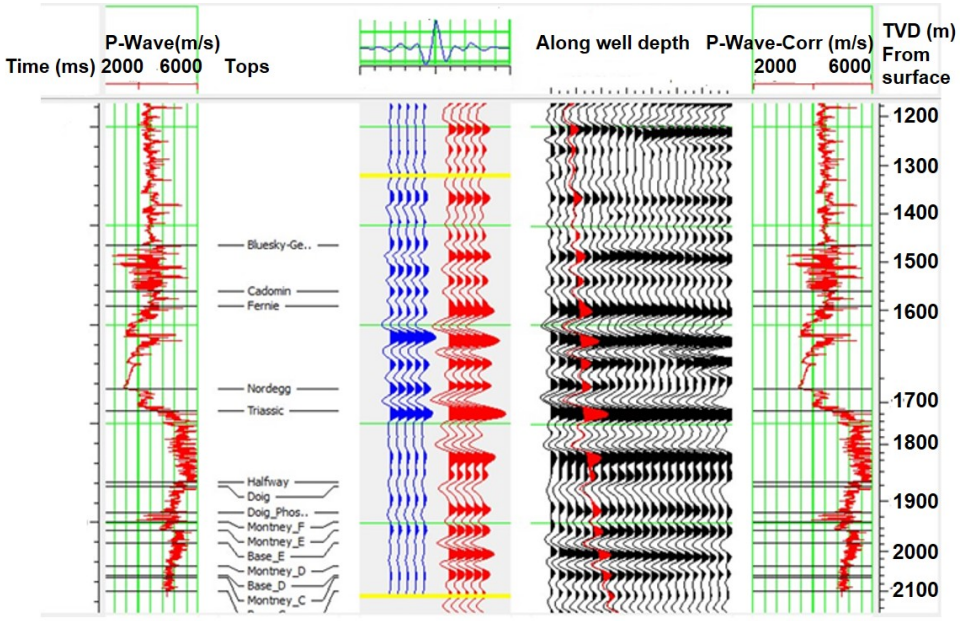

Figure 5.6: Vertical well tie with baseline P-wave seismic.

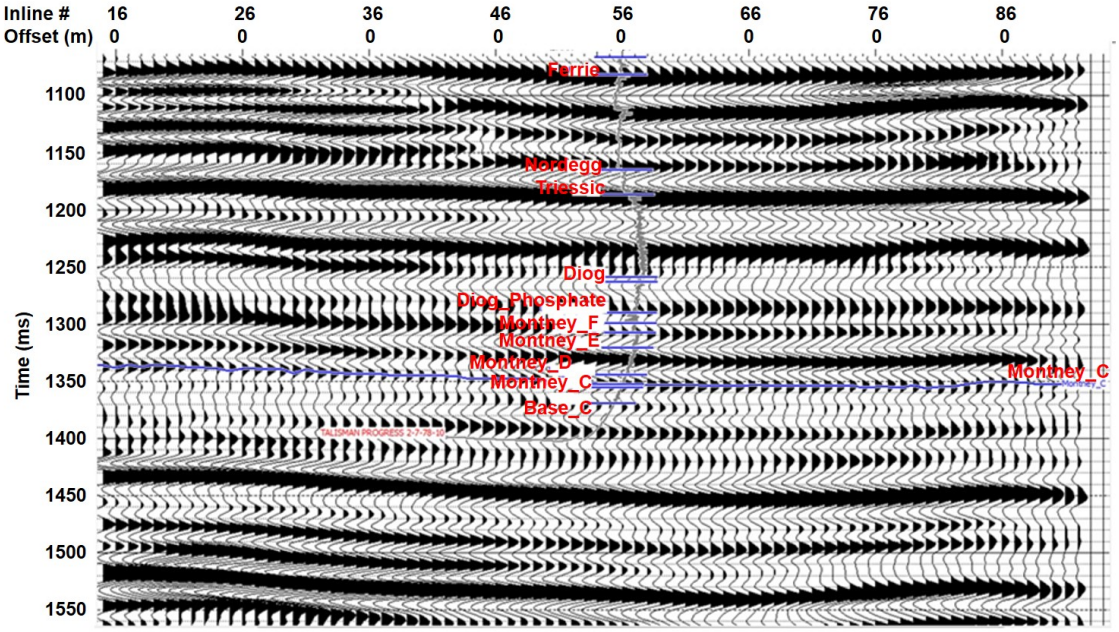

Figure 5.7: Estimating the horizon times on the seismic section by tying synthetic in Figure 5.6 to the baseline seismic data.

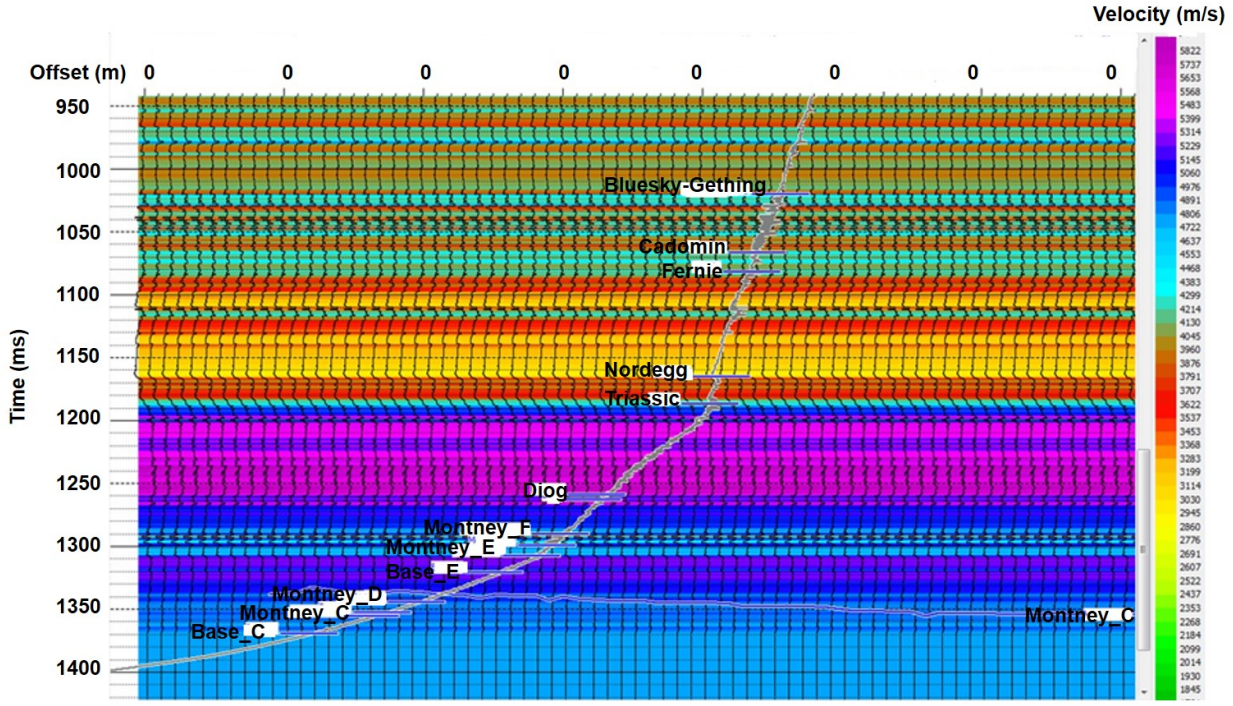

Figure 5.8: Synthetic P-wave log representing post-fracture condition created.

to interpret the seismic data for the monitor seismic sections. But prior to this, we need to derive log information at the time of the monitor surveys, as well logs were not acquired at the time of the monitor surveys. All log data were acquired at the time of the baseline survey and before inducing the fractures. The synthetic logs for the monitor survey are modelled by simulating the parameters in the systematic changes during the fracture operations. The input parameters include initial P-wave, S-wave, and density logs at the time of the baseline survey, reservoir parameters such as water saturation, gas saturation, temperature, pressure, salinity, and matrix before and after the fracture operations. Figure 5.8 shows the synthetic sonic log aligned on the monitor seismic section.

Perturbation parameters in equation and equation should be calculated in order to derive the reflection coefficient for time-lapse difference data or $\Delta R_{PP}(\theta)$. This is possible if the P-wave and S-wave velocities, and density information for the cap rock (layer just above the

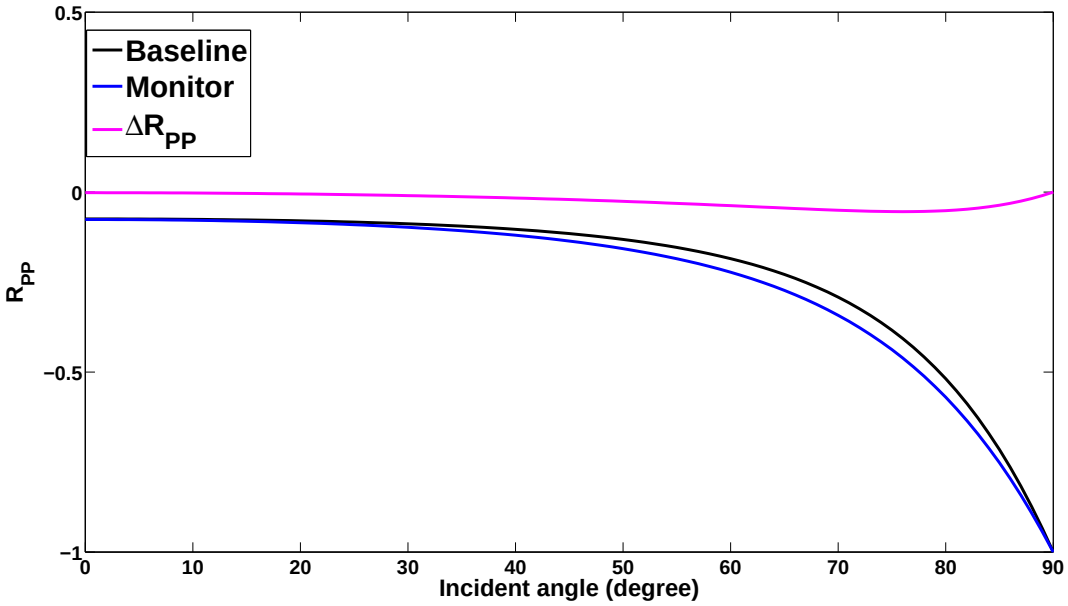

Figure 5.9: $R_{PP}(\theta)$ for the baseline (black) and monitor (blue) surveys and for their difference (red), $\Delta R_{PP}(\theta)$, for Pouce Coupe data set

reservoir), and reservoir at the time of the baseline and monitor surveys are available. The top of the Montney C and the top of the Montney D are the interfaces between the cap rock and the reservoir. V_{P_0}, V_{S_0}, ρ_0 and V_{P_b}, V_{S_b}, ρ_b are derived from the well logs obtained at the time of the baseline survey. We used synthetic logs at the time of the monitor survey to estimate V_{P_m}, V_{S_m}, ρ_m after the fracture operations.

5.1.2 Results

With three sets of the P-wave, S-wave velocities, and the density for the formation above the reservoir or target, and the reservoir itself before and after the fracture, exact $\Delta R_{PP}(\theta)$ for the baseline survey, monitor survey, and their difference are calculated using the Zoeppritz equations (Figure 5.9). The red curve representing the time-lapse difference reflection coefficient, is almost at zero for all offsets. The reason is because the reflection coefficient, R_{PP}, for the baseline and monitor surveys are almost identical. This can be

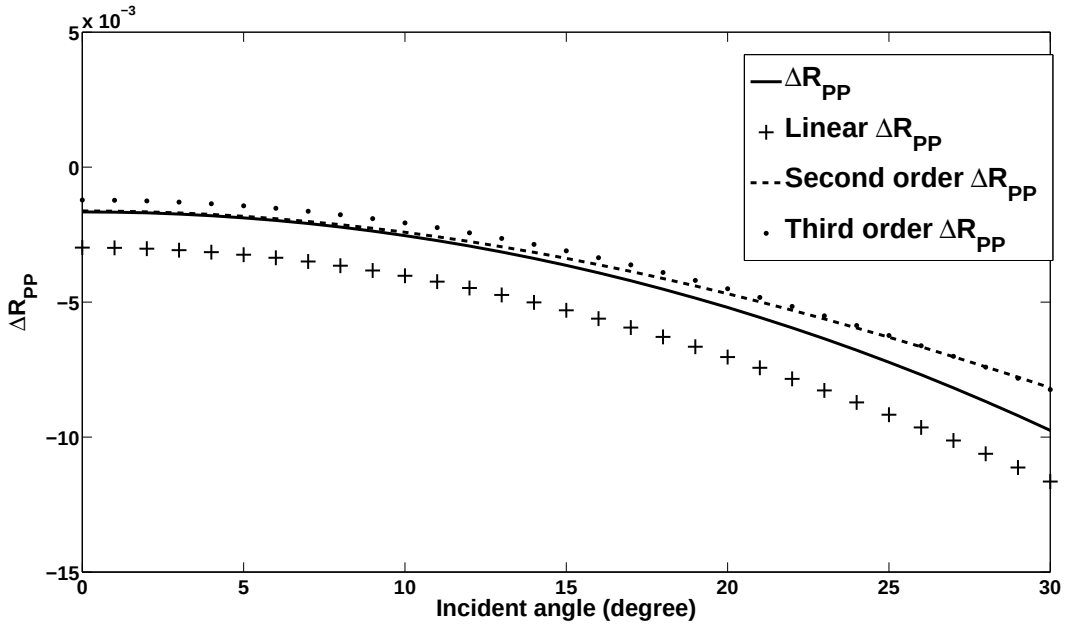

Figure 5.10: $\Delta R_{PP}(\theta)$ for the exact (solid line), linear (+++), second (—), and third order (...) approximation for Pouce Coupe data set

expected by investigating the well log information and seismic sections (as in Figure 5.6-5.8) at the interface of the tops of Montney C and Montney D (as the productive layers or reservoir layers). Investigating the difference in gamma, P-wave and S-wave velocities and density logs in Figure 5.5 in the area of interest at around 1350 ms time depth, we can see the low baseline contrast between the reservoir (Montney C) and the cap rock (layer above it by our definition). Also the seismic parameters, P-wave and S-wave velocities, and density for the reservoir formation at the time of the baseline survey relative to the monitor survey are similar. This explains the similarity of reflection coefficient for the baseline and monitor surveys. Choosing another interface such as the base of the Doig or the base of the Montney E may give a higher contrast in the baseline survey.

In Figure 5.10, the exact difference data are compared to the linear and nonlinear time-lapse AVO approximation derived from the results of Jabbari et al. (2015). These results does not show a significant difference between linear and higher order approximations in

$\Delta R_{PP}(\theta)$.

Chapter 6

Conclusions

Time-lapse studies monitor fluid flow and pressure changes over time in a reservoir caused by production or the employment of enhanced oil recovery techniques. Time-lapse measurements provide a tool to monitor the dynamic changes in subsurface properties throughout the development phase during the exploitation of a reservoir. Changes in geological and geophysical properties of a reservoir, such as fluid saturation and pore pressure, produce measurable changes in elastic parameters such as P-wave and S-wave velocities and density. These changes affect the reflection data from the interface between the cap rock and reservoir layers. Therefore changes in the pressure or fluid saturation, or both, in a reservoir can determine the difference data between the baseline survey data and monitor survey data.

Landrø (2001) provided a linear approximation for the time-lapse difference reflection data for fluid saturation- and pressure-related changes. He also concluded that a second order approximation for the relationship between the reservoir parameters (fluid saturation and pressure) and the seismic parameters (P-wave and S-wave velocity and density) may on occasion be important.

The accuracy of Landrø's linear difference equation diminishes when the contrast between the reservoir at the time of the baseline survey and monitor survey is relatively large. Also his linear equation is independent of the physical properties contrast between the cap rock and reservoir in the baseline survey. As changes in the elastic parameters such as P-wave and S-wave velocity, and density can be large in a time-lapse scenario Landrø (2001), adding the higher order approximation in the difference data reflection coefficient is highly recommended.

Perturbation theory can be used to pose time-lapse seismic monitoring problems in a

quantitative and interpretable and easily analyzable way. Forms for elastic difference reflection coefficients that closely resemble standard linearized AVO (amplitude versus offset) equations are derivable, with nonlinear corrections that include coupling terms between baseline and time-lapse changes.

6.1 Nonlinearity in Time-lapse difference data AVO

Changes in the fluid saturation and pressure will have an impact on elastic parameters of subsurface, such as P-wave and S-wave velocities and density, which can be approximated by applying time-lapse AVO analysis methods. Linearized P-P AVO modelling of time-lapse difference data was discussed by Landrø (2001). In Chapter 3, a framework is formulated for the difference in reflection amplitude between the baseline survey data and monitor survey data. This framework is expressed as an expansion in orders of both baseline interface properties and time-lapse changes from the time of the baseline survey to the time of the monitor survey. The difference data include linear and nonlinear terms in perturbation parameters, where these perturbation parameters quantify the changes in P- and S-wave velocities and density from the time of the baseline relative to the time of the monitor survey. Linear and nonlinear terms representing the relative changes in in elastic properties are derived in ΔR_{PP}. The linear term is in agreement with Landrø's equation. Nonlinear terms represent corrections appropriate for large contrasts. Including second- and third-order terms in ΔR_{PP} improves the accuracy of calculating time-lapse difference reflection data, particularly for large-contrast cases.

Numerical analyses are conducted to examine the derived linear and non linear difference time-lapse AVO terms. For this purpose, examples from real time-lapse cases used by Veire et al. (2006) and Landrø (2001) are applied. Numerical studies indicate that in geophysically plausible (though reasonably large-contrast) scenarios, these nonlinear terms can have significant impact in pre-critical regimes and improve the accuracy of approximating time-lapse

difference reflection data, particularly for large contrast cases. Therefore, the nonlinearity of the relationship between the difference data and perturbations in P- and S-wave velocities and density may be significant and non-negligible in geophysically plausible scenarios (Jabbari et al., 2015).

Multicomponent surveying has been developed rapidly in seismology, including time-lapse monitoring (Stewart et al., 2003). Multicomponent time-lapse amplitude variation with offset (AVO) may improve the accuracy of approximation of time-lapse difference data. A well-developed AVO regimes analyzes converted waves and shear waves AVO as well the P-wave AVO. This work, therefore, is extended to time-lapse difference data by formulating a framework for the difference reflection data for shear waves or ΔR_{SS} (Jabbari and Innanen, 2015). Also, the extension of this work is applied to converted waves to derive linear and nonlinear terms for ΔR_{PS} and ΔR_{SP} (Jabbari and Innanen, 2016).

In general, the results show that adding the higher order terms to the linear approximation in ΔR for P-P data, shear waves and converted waves for difference time-lapse data increases the accuracy of approximating time-lapse difference reflection data for ΔR_{PP}, ΔR_{SS}, ΔR_{PS}, and ΔR_{SP}, particularly for large contrast cases. This also corrects the error due to linearizing ΔR_{PP}, ΔR_{SS}, ΔR_{PS}, and ΔR_{SP}. Therefore, in many plausible time-lapse scenarios the increase in accuracy associated with higher order corrections is non-negligible for converted waves and shear waves as well as P-P data.

Comparing linear, second , and third order terms for ΔR_{PS} and ΔR_{SP} indicates that as we move toward higher order approximations, ΔR_{PS} and ΔR_{SP} are different. This confirms the difference between exact ΔR_{PS} and ΔR_{SP}, which does not show up in the linear approximation case.

In summary, the difference data during the change in a reservoir from the baseline survey relative to the monitor survey are described for shear waves, and converted waves. We defined a framework for the difference reflection data, $\Delta R_{SS}(\theta)$, $\Delta R_{PS}(\theta)$, and $\Delta R_{SP}(\theta)$, in

order of physical change or baseline interface contrast and time-lapse changes. A framework for linear and non linear time-lapse difference data are formulated using amplitude variation with offset (AVO) methods. The higher order terms represent corrections appropriate for large contrasts.

6.1.1 Validating the theoretical results with physical modelling

A physical model experiment is acquired, simulating a time lapse problem to investigate the theoretical results for linear and nonlinear ΔR_{PP}. Slabs of plexiglas, PVC, and phenolic are used to resemble the cap rock, the reservoir at the time of the baseline survey, and the reservoir at the time of the monitor survey.

The physically-modelled experimental data used for comparison with nonlinear expressions for time-lapse AVO are based on materials with large changes (greater than 10%) in reflectivity. This is atypical, since time-lapse changes in field data do not usually exceed two to three percent. However, though atypical, these relative changes are not impossible. In fact, we see them as being quite close to an end-member on the range of real geological changes possible, taking our cue from, e.g., the V_P vs. Effective stress model discussed by Landrø (2001). See for example Landrø's Figure 2. Thus, they are well-suited to our study of the role of coupling and nonlinearity, which are maximal in large contrast cases. Adding to less geologically atypical examples would of course be ideal, but available non-attenuating materials for physical modelling experiments that closely match those encountered in geological situations are limited. Real sandstones and shales cannot be used because of their significant attenuation at the modelling frequencies of 200 kHz to 1MHz. We emphasize that the physically-modelled data are used primarily to provide experimental validation of the nonlinear expressions. Laboratory validation of our expressions in the largest contrast cases allows us to apply them with confidence to lower contrast situations encountered in the field.

A comparison of the theoretical results for linear and higher order approximation with the physical model data indicated that including higher order terms in approximating the

difference data is highly recommended. Landrø (2001) showed the relationship between relative changes in P-wave velocity and pressure changes in the Gullfaks field. He suggests obtaining a second order approximation for these changes. In the same data set the relationship between seismic parameters and fluid saturation is not strongly nonlinear and can be approximated by a linear function between these parameters. As a conclusion, whenever nonlinear relationships exist between changes in seismic parameters and changes in reservoir parameters, higher-order terms in approximating the difference data should be included, particularly if large contrasts in cap rock and reservoir properties are involved.

As with the suggested framework, approximating the difference time-lapse data by including the linear and higher order terms, is straight forward and sufficient, it is strongly suggested to use this approach for approximating difference time-lapse for low and high contrast cases. It will be appropriate for lower contrasts in which linear approximation is good enough and for higher contrasts in which higher order approximation is definitely needed.

6.1.2 Validating the results with Pouce Coupe time-lapse data

A time-lapse data set is used to validate derived linear and nonlinear theoretical results for the time-lapse AVO difference data. This data set was acquired during hydraulic fracturing of two horizontal wells in the unconventional Montney Reservoir at Pouce Coupe Field in the Peace River area by Talisman Energy Inc. part of Repsol Group. An increase in pore pressure has been induced following the hydraulic fracture operations in the unconventional Montney shale reservoir. This will affect the seismic parameters including P-wave and S-wave velocities and density. Due to the tight nature and low permeability of the Montney reservoir, the injection of fluid into the reservoir during the fracture operations will affect only the close vicinity of the fractures. For this reason, the change in elastic parameters should be investigated in the vicinity of the hydraulic fractures in the horizontal wells. This is practically impossible with the present Pouce Coupe data set.

The Pouce Coupe data set shows low contrast between the cap rock and reservoir (the

tops of Montney C and the base of Montney D) in the baseline survey and also lower contrast in time-lapse changes from time of the baseline survey relative to the time of the monitor survey. Therefore, the contribution of the nonlinear terms in approximating the time-lapse difference data is not significant for the Pouce Coupe data set for the the Montney C or Montney D layers as the reservoir interfaces.

6.2 Future work

The validation of the nonlinear portion of the time-lapse difference AVO in addition to the linear portion with the field data is a matter of ongoing research and will be continued after this thesis. A processing flow has been established to pick events whose time-lapse AVO signatures may be analyzed for nonlinearity. The analysis investigated in this thesis, can be applied to another interface with a larger seismic signature in the baseline survey or larger time-lapse signature. For example the upper layer of Montney Formation, Montney F, is also a productive layer. The Doig Phosphate and Montney F interface has a larger contrast between the cap rock and the reservoir layers and can be analyzed in investigation of the nonlinearity of the time-lapse AVO difference.

The processing flow established and used on the Pouce Coupe data set needs to be applied to more horizons in this data set, and other data sets, to gauge the practical importance of the nonlinear time-lapse AVO difference terms.

Appendix A

Third order term in ΔR_{PP}

The third order term in difference data in time-lapse AVO in terms of the baseline and time-lapse perturbations is calculated as:

$$\begin{aligned}
\Delta R^{(3)}_{PP}(\theta) =&(\Gamma_{PPP})a^3_{VP} + (\Gamma_{SSS})a^3_{VS} + (\Gamma_{\rho\rho\rho})a^3_{\rho} + (\Gamma_{PS\rho})\left(b_{VP}b_{VS}a_{\rho} + b_{VS}b_{\rho}a_{VP}\right.\\
&\left.+b_{VS}a_{VP}a_{\rho} + b_{\rho}a_{VP}a_{VS} + a_{VP}a_{VS}a_{\rho} + b_{VP}a_{VS}a_{\rho} + b_{VP}b_{\rho}a_{VS}\right)\\
&+ (\Gamma_{SS\rho})\left(b_{VS}a_{VS}b_{\rho} + b_{VS}a_{VS}a_{\rho}\right) + (\Gamma_{S\rho\rho})\left(b_{VS}b_{\rho}a_{\rho} + b_{\rho}a_{\rho}a_{VS}\right)\\
&+ (\Gamma_{PPS})(b_{VP}a_{VP}a_{VS} + b_{VP}b_{VS}a_{VP}) + (\Gamma_{PP\rho})(b_{VP}a_{VP}a_{\rho} + b_{VP}b_{\rho}a_{VP})\\
&- (\Gamma_{PSS})(b_{VP}b_{VS}a_{VS} + b_{VS}a_{VS}a_{VP}) + (\Gamma_{P\rho\rho})(b_{\rho}a_{VP}a_{\rho}) - (\Gamma_{PS^2})b_{VP}a^2_{VS}\\
&+ (\Gamma_{PP^2})(b_{VP}a^2_{VP} + a_{VP}b^2_{VP}) + (\Gamma_{P\rho^2})(b_{VP}a^2_{\rho} + a_{VP}b^2_{\rho} + a_{VP}a^2_{\rho})\\
&+ (\Gamma_{\rho P^2})(b_{\rho}a^2_{VP} + a_{\rho}a^2_{VP} + a_{\rho}b^2_{VP}) + (\Gamma_{SS^2})(a_{VS}b^2_{VS} + b_{VS}a^2_{VS})\\
&+ (\Gamma_{\rho S^2})(b_{\rho}a^2_{VS} + a_{\rho}a^2_{VS} + a_{\rho}b^2_{VS}) + (\Gamma_{SP^2})(a_{VS}b^2_{VP})\\
&- (\Gamma_{PS^2})(a_{VP}b^2_{VS} + a_{VP}a^2_{VS}) + (\Gamma_{S\rho^2})(a_{VS}a^2_{\rho} + b_{VS}a^2_{\rho} + a_{VS}b^2_{\rho})\\
&+ (\Gamma_{\rho\rho^2})(b_{\rho}a^2_{\rho} + a_{\rho}b^2_{\rho}),
\end{aligned} \tag{A.1}$$

where 'Γ's are listed in Table 1.

Table A.1: Table of 'Γ's in Equation A.1

Symbol	Description
Γ_{PPP}	$\frac{15}{64}\left(\sin^2\theta\right)+\frac{5}{64}$
Γ_{SSS}	$\frac{7}{4}\left(\frac{V_{S_0}}{V_{P_0}}\right)^3\sin^2\theta-2\left(\frac{V_{S_0}}{V_{P_0}}\right)^2\sin^2\theta$
$\Gamma_{\rho\rho\rho}$	$\frac{1}{2}\left(\frac{V_{S_0}}{V_{P_0}}\right)^3\sin^2\theta-\frac{3}{8}\left(\frac{V_{S_0}}{V_{P_0}}\right)\sin^2\theta+\frac{1}{8}$
$\Gamma_{PS\rho}$	$\frac{1}{2}\left(\frac{V_{S_0}}{V_{P_0}}\right)^2\sin^2\theta-\left(\frac{V_{S_0}}{V_{P_0}}\right)^3\sin^2\theta$
$\Gamma_{SS\rho}$	$2\left(\frac{V_{S_0}}{V_{P_0}}\right)^3\sin^2\theta-\frac{1}{2}\left(\frac{V_{S_0}}{V_{P_0}}\right)^2\sin^2\theta$
$\Gamma_{S\rho\rho}$	$\frac{3}{2}\left(\frac{V_{S_0}}{V_{P_0}}\right)^2\sin^2\theta-\frac{1}{2}\left(\frac{V_{S_0}}{V_{P_0}}\right)^3\sin^2\theta$ $-\frac{1}{8}\left(\frac{V_{S_0}}{V_{P_0}}\right)\sin^2\theta$
Γ_{PPS}	$\frac{1}{4}\left(\frac{V_{S_0}}{V_{P_0}}\right)^2\sin^2\theta$
$\Gamma_{PP\rho}$	$\frac{1}{4}\left(\frac{V_{S_0}}{V_{P_0}}\right)^2\sin^2\theta-\frac{1}{8}\sin^2\theta-\frac{1}{16}$
Γ_{PSS}	$\left(\frac{V_{S_0}}{V_{P_0}}\right)^3\sin^2\theta$
$\Gamma_{P\rho\rho}$	$\left(\frac{V_{S_0}}{V_{P_0}}\right)^2\sin^2\theta-\left(\frac{V_{S_0}}{V_{P_0}}\right)^3\sin^2\theta-\frac{1}{4}\left(\frac{V_{S_0}}{V_{P_0}}\right)$ $\sin^2\theta-\left(\frac{1}{8}\right)\sin^2\theta$
Γ_{PP^2}	$\frac{13}{64}\sin^2\theta-\frac{1}{64}$
$\Gamma_{P\rho^2}$	$\frac{1}{2}\left(\frac{V_{S_0}}{V_{P_0}}\right)^2\sin^2\theta-\frac{1}{2}\left(\frac{V_{S_0}}{V_{P_0}}\right)^3\sin^2\theta$ $-\frac{1}{8}\left(\frac{V_{S_0}}{V_{P_0}}\right)\sin^2\theta-\left(\frac{1}{16}\right)\sin^2\theta-\frac{1}{16}$
Γ_{PS^2}	$\frac{1}{2}\left(\frac{V_{S_0}}{V_{P_0}}\right)^3\sin^2\theta$
$\Gamma_{\rho P^2}$	$\frac{1}{8}B^2\sin^2\theta-\frac{1}{16}\sin^2\theta-\frac{1}{32}$
Γ_{SS^2}	$\frac{13}{4}\left(\frac{V_{S_0}}{V_{P_0}}\right)^3\sin^2\theta-2\left(\frac{V_{S_0}}{V_{P_0}}\right)^2\sin^2\theta$
$\Gamma_{\rho S^2}$	$2\left(\frac{V_{S_0}}{V_{P_0}}\right)^3\sin^2\theta-\frac{3}{4}\left(\frac{V_{S_0}}{V_{P_0}}\right)^2\sin^2\theta$
Γ_{SP^2}	$\frac{1}{8}\left(\frac{V_{S_0}}{V_{P_0}}\right)^2\sin^2\theta$
$\Gamma_{S\rho^2}$	$\frac{3}{4}\left(\frac{V_{S_0}}{V_{P_0}}\right)^3\sin^2\theta+\frac{1}{4}\left(\frac{V_{S_0}}{V_{P_0}}\right)^2\sin^2\theta$ $-\frac{1}{16}\left(\frac{V_{S_0}}{V_{P_0}}\right)\sin^2\theta$
$\Gamma_{\rho\rho^2}$	$2\left(\frac{V_{S_0}}{V_{P_0}}\right)^2\sin^2\theta-\frac{1}{2}\left(\frac{V_{S_0}}{V_{P_0}}\right)^3\sin^2\theta$ $-\frac{5}{8}\left(\frac{V_{S_0}}{V_{P_0}}\right)\sin^2\theta-\frac{1}{8}$

This third order term in difference data in time-lapse AVO is also recalculated in terms of relative parameters as:

$$
\begin{aligned}
\Delta R_{PP}^{(3)}(\theta) =&(\kappa_{PPP})\left(\frac{\delta V_P}{V_P}\right)^3+(\kappa_{SSS})\left(\frac{\delta V_S}{V_S}\right)^3+(\kappa_{\rho\rho\rho})\left(\frac{\delta\rho}{\rho}\right)^3+(\kappa_{PS\rho})\\
&\left[\left(\frac{\Delta V_P}{V_P}\right)\left(\frac{\Delta\rho}{\rho}\right)\left(\frac{\delta V_S}{V_S}\right)+\left(\frac{\Delta V_S}{V_S}\right)\left(\frac{\delta\rho}{\rho}\right)\left(\frac{\delta V_P}{V_P}\right)\right.\\
&+\left(\frac{\Delta V_P}{V_P}\right)\left(\frac{\delta\rho}{\rho}\right)\left(\frac{\Delta V_S}{V_S}\right)+\left(\frac{\delta V_P}{V_P}\right)\left(\frac{\Delta\rho}{\rho}\right)\left(\frac{\delta V_S}{V_S}\right)\\
&+\left(\frac{\Delta\rho}{\rho}\right)\left(\frac{\delta V_P}{V_P}\right)\left(\frac{\delta V_S}{V_S}\right)+\left(\frac{\Delta V_P}{V_P}\right)\left(\frac{\Delta V_S}{V_S}\right)\left(\frac{\delta\rho}{\rho}\right)\\
&\left.+\left(\frac{\Delta V_S}{V_S}\right)\left(\frac{\Delta\rho}{\rho}\right)\left(\frac{\delta V_P}{V_P}\right)\right]\\
&+(\kappa_{SS\rho})\left[\left(\frac{\Delta V_S}{V_S}\right)\left(\frac{\delta\rho}{\rho}\right)\left(\frac{\delta V_S}{V_S}\right)+\left(\frac{\Delta V_S}{V_S}\right)\left(\frac{\Delta\rho}{\rho}\right)\left(\frac{\delta V_S}{V_S}\right)\right]\\
&+(\kappa_{PP\rho})\left[\left(\frac{\Delta V_P}{V_P}\right)\left(\frac{\Delta\rho}{\rho}\right)\left(\frac{\delta V_P}{V_P}\right)+\left(\frac{\Delta V_P}{V_P}\right)\left(\frac{\delta\rho}{\rho}\right)\left(\frac{\delta V_P}{V_P}\right)\right]\\
&+(\kappa_{P\rho\rho})\left[\left(\frac{\Delta\rho}{\rho}\right)\left(\frac{\delta V_P}{V_P}\right)\left(\frac{\delta\rho}{\rho}\right)\right]\\
&+(\kappa_{PSS})\left[\left(\frac{\Delta V_S}{V_S}\right)\left(\frac{\delta V_S}{V_S}\right)\left(\frac{\delta V_P}{V_P}\right)+\left(\frac{\Delta V_P}{V_P}\right)\left(\frac{\Delta V_S}{V_S}\right)\left(\frac{\delta V_S}{V_S}\right)\right] \qquad \text{(A.2)}\\
&+(\kappa_{PPS})\left[\left(\frac{\Delta V_P}{V_P}\right)\left(\frac{\delta V_S}{V_S}\right)\left(\frac{\delta V_P}{V_P}\right)+\left(\frac{\Delta V_P}{V_P}\right)\left(\frac{\Delta V_S}{V_S}\right)\left(\frac{\delta V_P}{V_P}\right)\right]\\
&+(\kappa_{S\rho\rho})\left[\left(\frac{\Delta V_S}{V_S}\right)\left(\frac{\Delta\rho}{\rho}\right)\left(\frac{\delta\rho}{\rho}\right)+\left(\frac{\Delta\rho}{\rho}\right)\left(\frac{\delta\rho}{\rho}\right)\left(\frac{\delta V_S}{V_S}\right)\right]\\
&+(\kappa_{SP^2})\left[\left(\frac{\delta V_S}{V_S}\right)\left(\frac{\delta V_P}{V_P}\right)^2+\left(\frac{\Delta V_S}{V_S}\right)\left(\frac{\delta V_P}{V_P}\right)^2+\left(\frac{\delta V_S}{V_S}\right)\left(\frac{\Delta V_P}{V_P}\right)^2\right]\\
&-(\kappa_{PS^2})\left[\left(\frac{\Delta V_P}{V_P}\right)\left(\frac{\delta V_S}{V_S}\right)^2+\left(\frac{\delta V_P}{V_P}\right)\left(\frac{\Delta V_S}{V_S}\right)^2+\left(\frac{\delta V_P}{V_P}\right)\left(\frac{\delta V_S}{V_S}\right)^2\right]\\
&+(\kappa_{SS^2})\left[\left(\frac{\Delta V_S}{V_S}\right)\left(\frac{\delta V_S}{V_S}\right)^2+\left(\frac{\delta V_S}{V_S}\right)\left(\frac{\Delta V_S}{V_S}\right)^2\right]\\
&+(\kappa_{S\rho^2})\left[\left(\frac{\delta V_S}{V_S}\right)\left(\frac{\delta\rho}{\rho}\right)^2+\left(\frac{\Delta V_S}{V_S}\right)\left(\frac{\delta\rho}{\rho}\right)^2+\left(\frac{\delta V_S}{V_S}\right)\left(\frac{\Delta\rho}{\rho}\right)^2\right]\\
&+(\kappa_{\rho S^2})\left[\left(\frac{\delta\rho}{\rho}\right)\left(\frac{\delta V_S}{V_S}\right)^2+\left(\frac{\delta\rho}{\rho}\right)\left(\frac{\Delta V_S}{V_S}\right)^2+\left(\frac{\Delta\rho}{\rho}\right)\left(\frac{\delta V_S}{V_S}\right)^2\right]
\end{aligned}
$$

$$
\begin{aligned}
&+ (\kappa_{PP^2}) \left[\left(\frac{\delta V_P}{V_P} \right) \left(\frac{\Delta V_P}{V_P} \right)^2 + \left(\frac{\Delta V_P}{V_P} \right) \left(\frac{\delta V_P}{V_P} \right)^2 \right] \\
&+ (\kappa_{\rho P^2}) \left[\left(\frac{\delta \rho}{\rho} \right) \left(\frac{\Delta V_P}{V_P} \right)^2 + \left(\frac{\delta \rho}{\rho} \right) \left(\frac{\delta V_P}{V_P} \right)^2 + \left(\frac{\Delta \rho}{\rho} \right) \left(\frac{\delta V_P}{V_P} \right)^2 \right] \\
&+ (\kappa_{P\rho^2}) \left[\left(\frac{\Delta V_P}{V_P} \right) \left(\frac{\delta \rho}{\rho} \right)^2 + \left(\frac{\delta V_P}{V_P} \right) \left(\frac{\delta \rho}{\rho} \right)^2 . + \left(\frac{\delta V_P}{V_P} \right) \left(\frac{\Delta \rho}{\rho} \right)^2 \right] \\
&+ (\kappa_{\rho\rho^2}) \left[\left(\frac{\Delta \rho}{\rho} \right) \left(\frac{\delta \rho}{\rho} \right)^2 + \left(\frac{\delta \rho}{\rho} \right) \left(\frac{\Delta \rho}{\rho} \right)^2 \right],
\end{aligned}
\tag{A.3}
$$

where 'κ's are listed in Table 2.

Table A.2: Table of 'κ's in Equation A.2

Symbol	Description
κ_{PPP}	$8\left(\frac{15}{64}\sin^2\theta+\frac{5}{64}\right)$
κ_{SSS}	$8\left(\frac{7}{4}\left(\frac{V_{S_0}}{V_{P_0}}\right)^3\sin^2\theta-2\left(\frac{V_{S_0}}{V_{P_0}}\right)^2\sin^2\theta\right)$
$\kappa_{\rho\rho\rho}$	$\frac{1}{2}\left(\frac{V_{S_0}}{V_{P_0}}\right)^3\sin^2\theta-\frac{3}{8}\left(\frac{V_{S_0}}{V_{P_0}}\right)\sin^2\theta+\frac{1}{8}$
$\kappa_{PS\rho}$	$4\left(\frac{1}{2}\left(\frac{V_{S_0}}{V_{P_0}}\right)^2\sin^2\theta-\left(\frac{V_{S_0}}{V_{P_0}}\right)^3\sin^2\theta\right)$
$\kappa_{SS\rho}$	$4\left(2B^3\sin^2\theta-\frac{1}{2}B^2\sin^2\theta\right)$
$\kappa_{S\rho\rho}$	$2\left[\frac{3}{2}\left(\frac{V_{S_0}}{V_{P_0}}\right)^2\sin^2\theta-\frac{1}{2}\left(\frac{V_{S_0}}{V_{P_0}}\right)^3\sin^2\theta-\frac{1}{8}\left(\frac{V_{S_0}}{V_{P_0}}\right)\sin^2\theta\right]$
κ_{PPS}	$2\left[\left(\frac{V_{S_0}}{V_{P_0}}\right)^2\sin^2\theta\right]$
$\kappa_{PP\rho}$	$4\left[\frac{1}{4}\left(\frac{V_{S_0}}{V_{P_0}}\right)^2\sin^2\theta-\frac{1}{8}\sin^2\theta-\frac{1}{16}\right]$
κ_{PSS}	$-8\left[\left(\frac{V_{S_0}}{V_{P_0}}\right)^3\sin^2\theta\right]$
$\kappa_{P\rho\rho}$	$2\left[\left(\frac{V_{S_0}}{V_{P_0}}\right)^2\sin^2\theta-\left(\frac{V_{S_0}}{V_{P_0}}\right)^3\sin^2\theta-\frac{1}{4}\left(\frac{V_{S_0}}{V_{P_0}}\right)\sin^2\theta-\frac{1}{8}\sin^2\theta-\frac{1}{8}\right]$
κ_{PP^2}	$8\left[\frac{13}{64}\sin^2\theta-\frac{1}{64}\right]$
$\kappa_{P\rho^2}$	$2\left[\frac{1}{2}\left(\frac{V_{S_0}}{V_{P_0}}\right)^2\sin^2\theta-\frac{1}{2}\left(\frac{V_{S_0}}{V_{P_0}}\right)^3\sin^2\theta-\frac{1}{8}\left(\frac{V_{S_0}}{V_{P_0}}\right)\sin^2\theta-\frac{1}{16}\sin^2\theta-\frac{1}{16}\right]$
κ_{PS^2}	$4\left[\left(\frac{V_{S_0}}{V_{P_0}}\right)^3\sin^2\theta\right]$
$\kappa_{\rho P^2}$	$4\left[\frac{1}{8}\left(\frac{V_{S_0}}{V_{P_0}}\right)^2\sin^2\theta-\frac{1}{16}\sin^2\theta-\frac{1}{32}\right]$
κ_{SS^2}	$8\left[\frac{13}{4}\left(\frac{V_{S_0}}{V_{P_0}}\right)^3\sin^2\theta-2\left(\frac{V_{S_0}}{V_{P_0}}\right)^2\sin^2\theta\right]$
$\kappa_{\rho S^2}$	$4\left[2\left(\frac{V_{S_0}}{V_{P_0}}\right)^3\sin^2\theta-\frac{3}{4}\left(\frac{V_{S_0}}{V_{P_0}}\right)^2\sin^2\theta\right]$
κ_{SP^2}	$\left[\left(\frac{V_{S_0}}{V_{P_0}}\right)^2\sin^2\theta\right]$
$\kappa_{S\rho^2}$	$2\left[\frac{3}{4}\left(\frac{V_{S_0}}{V_{P_0}}\right)^3\sin^2\theta+\frac{1}{4}\left(\frac{V_{S_0}}{V_{P_0}}\right)^2\sin^2\theta-\frac{1}{16}\left(\frac{V_{S_0}}{V_{P_0}}\right)\sin^2\theta\right]$
$\kappa_{\rho\rho^2}$	$2\left(\frac{V_{S_0}}{V_{P_0}}\right)^2\sin^2\theta-\frac{1}{2}\left(\frac{V_{S_0}}{V_{P_0}}\right)^3\sin^2\theta-\frac{5}{8}\left(\frac{V_{S_0}}{V_{P_0}}\right)\sin^2\theta-\frac{1}{8}$

Appendix B

Third order term in ΔR_{SS}

The third order term in difference data in time-lapse AVO in terms of the baseline and time-lapse perturbations is calculated as:

$$
\begin{aligned}
\Delta R^{(3)}_{SS}(\phi) =& \frac{1}{64}\left[5-\left(96\frac{V_{S_0}}{V_{P_0}}+63\right)\sin^2\phi\right]a^3_{VS}+\frac{1}{8}\left[\left(3\frac{V_{P_0}}{V_{S_0}}-4\frac{V_{S_0}}{V_{P_0}}-16\right)\right.\\
&\left.\sin^2\phi+3\right]a^3_{\rho}+\frac{1}{4}\sin^2\phi(a_{VP}a^2_{VS}+a_{VP}b^2_{VS}+b_{VP}a^2_{VS})\\
&+\frac{1}{32}\left[7-\left(48\frac{V_{S_0}}{V_{P_0}}+78\right)\sin^2\phi\right](b_{\rho}a^2_{VS}+a_{\rho}a^2_{VS}+a_{\rho}b^2_{VS})\\
&+\frac{1}{64}\left[7-\left(160\frac{V_{S_0}}{V_{P_0}}+125\right)\sin^2\phi\right](b_{VS}a^2_{VS}+a_{VS}b^2_{VS})\\
&+\frac{1}{8}\left[\left(2\frac{V_{P_0}}{V_{S_0}}+8\frac{V_{S_0}}{V_{P_0}}-35\right)\sin^2\phi+3\right](b_{VS}b_{\rho}a_{\rho}+a_{VS}b_{\rho}a_{\rho})\\
&+\frac{1}{4}\left[\left(2\frac{V_{S_0}}{V_{P_0}}-1\right)\sin^2\phi\right](b_{VS}b_{VP}a_{\rho}+b_{VS}a_{VP}b_{\rho}+a_{VP}a_{VS}a_{\rho}+a_{VS}a_{VP}b_{\rho}\\
&+a_{VS}b_{VP}a_{\rho}+b_{VP}a_{VS}b_{\rho}+b_{VS}a_{VP}a_{\rho})+\frac{1}{8}\left[\left(\frac{V_{P_0}}{V_{S_0}}+4\frac{V_{S_0}}{V_{P_0}}\right.\right.\\
&\left.\left.-4)\sin^2\phi\right](b_{VP}a_{\rho}b_{\rho}+a_{VP}a_{\rho}b_{\rho})+\frac{1}{16}\left[\left(\frac{V_{P_0}}{V_{S_0}}+4\frac{V_{S_0}}{V_{P_0}}-4\right)\sin^2\phi\right]\right.\\
&\left.(a_{VP}b^2_{\rho}+a_{VP}a^2_{\rho}+b_{VP}a^2_{\rho})+\frac{1}{2}\left[\frac{V_{S_0}}{V_{P_0}}\sin^2\phi\right](b_{VS}a_{VP}a_{VS}+b_{VP}b_{VS}a_{VS})\right.\\
&+\frac{1}{8}\left[\left(5\frac{V_{P_0}}{V_{S_0}}+4\frac{V_{S_0}}{V_{P_0}}-32\right)\sin^2\phi+5\right](a_{\rho}b^2_{\rho}+b_{\rho}a^2_{\rho})\\
&\frac{1}{16}\left[3-\left(16\frac{V_{S_0}}{V_{P_0}}+54\right)\sin^2\phi\right](b_{VS}a_{VS}a_{\rho}+b_{VS}a_{VS}b_{\rho})\\
&+\frac{1}{16}\left[\left(2\frac{V_{P_0}}{V_{S_0}}-8\frac{V_{S_0}}{V_{P_0}}-47\right)\sin^2\phi+5\right](a_{VS}b^2_{\rho}+a_{VS}a^2_{\rho}+b_{VS}a^2_{\rho})
\end{aligned}
\tag{B.1}
$$

Appendix C

Third order term in ΔR_{PS} and ΔR_{SP}

The third order term in difference data in time-lapse AVO in terms of the baseline and time-lapse perturbations for an incident P-wave and reflected S-wave is calculated as:

$$\begin{aligned}\Delta R_{PS}^{(3)}(\theta) = &\left[-\frac{5}{8}\frac{V_{S_0}}{V_{P_0}}\sin\theta\right]a_{VS}^3 + \left[\frac{1}{8}\left(2\frac{V_{S_0}}{V_{P_0}}-3\right)\sin\theta\right]a_\rho^3 + \left[-\frac{3}{8}\frac{V_{S_0}}{V_{P_0}}\sin\theta\right]\\ &(b_{VS}a_{VS}^2 + b_{VS}^2 a_{VS}) + \left[\frac{1}{16}\left(6\frac{V_{S_0}}{V_{P_0}}-1\right)\sin\theta\right](a_\rho^2 a_{VS} + b_\rho^2 a_{VS} + a_\rho^2 b_{VS}) +\\ &\left[\frac{1}{16}\left(4\frac{V_{S_0}}{V_{P_0}}-1\right)\sin\theta\right](a_\rho b_{VS}^2 + a_\rho a_{VS}^2 + b_\rho a_{VS}^2) + \left[\frac{1}{16}\left(2\frac{V_{S_0}}{V_{P_0}}-1\right)\right.\\ &\left.\sin\theta\right](b_\rho a_{VP}^2 + b_\rho^2 a_{VP} + a_\rho b_{VP}^2 + a_\rho^2 b_{VP} + a_\rho^2 a_{VP} + a_\rho a_{VP}^2) +\\ &\left[\frac{1}{8}\frac{V_{S_0}}{V_{P_0}}\sin\theta\right](b_{VP}^2 a_{VS} + a_{VP}^2 b_{VS} + a_{VP}^2 a_{VS} + b_{VP}b_{VS}a_{VS} + a_{VP}b_{VS}a_{VS})\\ &+ \left[\frac{1}{8}\left(6\frac{V_{S_0}}{V_{P_0}}-1\right)\sin\theta\right](b_\rho^2 a_\rho + b_\rho a_\rho^2) + \left[\frac{1}{32}\left(2\frac{V_{S_0}}{V_{P_0}}-1\right)\sin\theta\right](a_\rho b_{VP}a_{VS}\\ &+ a_\rho b_{VP}b_{VS} + b_\rho a_{VP}a_{VS} + b_\rho a_{VP}b_{VS} + a_\rho a_{VP}a_{VS} + a_\rho a_{VP}b_{VS} + b_\rho b_{VP}a_{VS})\\ &\left[\frac{1}{4}\frac{V_{S_0}}{V_{P_0}}\sin\theta\right](b_\rho b_{VS}a_{VS} + a_\rho b_{VS}a_{VS}) + \left[\frac{1}{2}\frac{V_{S_0}}{V_{P_0}}\sin\theta\right](b_\rho a_\rho a_{VS} + b_\rho a_\rho b_{VS})\\ &+ \left[\frac{3}{16}\frac{V_{S_0}}{V_{P_0}}\sin\theta\right](a_{VP}b_{VS}^2 + a_{VP}a_{VS}^2 + b_{VP}a_{VS}^2)\end{aligned} \tag{C.1}$$

The third order term in difference data in time-lapse AVO in terms of the baseline and time-lapse perturbations for an incident S-wave and reflected P-wave is calculated as:

$$\Delta R_{SP}^{(3)}(\phi) = \left[\left(\frac{3}{8}\right)\frac{V_{S_0}}{V_{P_0}}\sin\phi\right] a_{VS}^3 + \left[\frac{1}{8}\left(10\frac{V_{S_0}}{V_{P_0}}+1\right)\sin\phi\right](a_\rho^3 + b_{VS}b_\rho a_{VS} + b_{VS}a_\rho a_{VS}$$
$$+ b_\rho a_{VS}^2 + a_\rho a_{VS}^2 + a_\rho b_{VS}^2) + \left[\frac{1}{32}\left(2\frac{V_{S_0}}{V_{P_0}}-1\right)\sin\phi\right](b_{VP}b_\rho a_{VS} +$$
$$b_{VP}a_\rho a_{VS} + b_{VS}b_\rho a_{VP} + b_{VS}a_\rho a_{VP} + b_{VP}a_\rho b_{VS} + a_{VP}b_\rho a_{VS} + a_{VP}a_\rho a_{VS})$$
$$+ \left[\frac{1}{4}\left(6\frac{V_{S_0}}{V_{P_0}}+1\right)\sin\phi\right](a_\rho b_\rho a_{VS} + a_\rho b_\rho b_{VS}) + \left[\frac{1}{16}\left(22\frac{V_{S_0}}{V_{P_0}}+3\right)\sin\phi\right]$$
$$(a_{VS}a_\rho^2 + b_{VS}a_\rho^2 + a_{VS}b_\rho^2) + \left[\frac{1}{8}\left(14\frac{V_{S_0}}{V_{P_0}}+3\right)\sin\phi\right](b_\rho a_\rho^2 + a_\rho b_\rho^2)\left[\frac{1}{16} +\right.$$
$$\left.\left(2\frac{V_{S_0}}{V_{P_0}}-1\right)\sin\phi\right](b_{VP}a_\rho^2 + a_{VP}b_\rho^2 + a_{VP}a_\rho^2 + a_{VP}^2 b_\rho + a_{VP}^2 a_\rho + b_{VP}^2 a_\rho)$$
$$+ \left[\left(\frac{5}{8}\right)\frac{V_{S_0}}{V_{P_0}}\sin\phi\right](a_{VS}b_{VS}^2 + b_{VS}a_{VS}^2) + \left[\left(\frac{1}{8}\right)\frac{V_{S_0}}{V_{P_0}}\sin\phi\right](a_{VS}b_{VP}^2 + b_{VS}a_{VP}^2$$
$$+ a_{VS}a_{VP}^2 + a_{VS}b_{VS}a_{VP} + a_{VS}b_{VS}b_{VP}) + \left[\left(\frac{3}{16}\right)\frac{V_{S_0}}{V_{P_0}}\sin\phi\right]$$
$$(b_{VP}a_{VS}^2 + a_{VP}b_{VS}^2 + a_{VP}a_{VS}^2) \tag{C.2}$$

Bibliography

Aki, K., and Richards, P. G., 2002, Quantitative seismology, vol. 1: University Science Books.

Arts, R., Eiken, O., Chadwick, A., Zweigel, P., Van der Meer, L., and Zinszner, B., 2004, Monitoring of co 2 injected at sleipner using time-lapse seismic data: Energy, **29**, No. 9, 1383–1392.

Atkinson, J., 2010, Multicomponent time-lapse monitoring of two hydraulic fracture stimulations in an unconventional reservoir, Pouce Coupe Field, Canada: M.Sc. thesis, Colorado School of Mines.

Berryman, L., Goupillaud, P., and Waters, K., 1958, Reflections from multiple transition layers part ii-experimental investigation: Geophysics, **23**, No. 2, 244–252.

Bhakta, T., and Landrø, M., 2014, Estimation of pressure-saturation changes for unconsolidated reservoir rocks with high vp/vs ratio: Geophysics, **79**, No. 5, M35–M54.

Bjørlykke, K., 2010, Petroleum Geoscience: From Sedimentary Environments to Rock Physics., chap. Introduction to petroleum geology, Springer Science, 1–29.

Buddensiek, M. L., Krawczyk, C. M., Kukowski, N., and Oncken, O., 2009, Performance of piezoelectric transducers in terms of amplitude and waveform: Geophysics, **74**, No. 2, T33–T45.

Carvalho, F. M., Weglein, A. B., Stolt, R. H. et al., 1991, Examples of a nonlinear inversion method based on the t matrix of scattering theory: application to multiple suppression, *in* 61st Ann. Internat. Mtg., Soc. Expl. Geophys., Society of Exploration Geophysicists, 1319–1322.

Castagna, J., and Backus, M., 1994, Offset dependent reflectivity: Theory and practice of avo analysis: Investigations in geophysics, , No. 8.

Castagna, J. P., Batzle, M. L., and Eastwood, R. L., 1985, Relationships between compressional-wave and shear-wave velocities in clastic silicate rocks: Geophysics, **50**, No. 4, 571–581.

Cohen, J. K., and Bleistein, N., 1977, An inverse method for determining small variations in propagation speed: SIAM Journal on Applied Mathematics, **32**, No. 4, 784–799.

Davey, H., 2012, Geomechanical characterization of the Montney shale Northwest Alberta and Northeast British Columbia: M.Sc. thesis, Colorado School of Mines.

Davies, G. R., Moslow, T. F., and Sherwin, M. D., 1997, The lower triassic montney formation, west-central alberta: Bulletin of Canadian Petroleum Geology, **45**, No. 4, 474–505.

De Waal, H., and Calvert, R., 2003, Overview of global 4d seismic implementation strategy: Petroleum Geoscience, **9**, No. 1, 1–6.

De Wolf, D. A., 1971, Electromagnetic reflection from an extended turbulent medium: cumulative forward-scatter single-backscatter approximation: Antennas and Propagation, IEEE Transactions on, **19**, No. 2, 254–262.

De Wolf, D. A., 1985, Renormalization of em fields in application to large-angle scattering from randomly continuous media and sparse particle distributions: Antennas and Propagation, IEEE Transactions on, **33**, No. 6, 608–615.

Duren, R. E., 1992, Range-equation weights for avo: Geophysics, **57**, No. 9, 1203–1208.

Eastwood, J., Johnston, D. H., Shyeh, J., Huang, X., Craft, K., Vauthrin, R., Workman, R. et al., 1999, Time-lapse seismic processing and analysis: Gulf of mexico example, lena field, *in* Offshore Technology Conference, Offshore Technology Conference.

Ghaderi, A., and Landrø, M., 2009, Estimation of thickness and velocity changes of injected carbon dioxide layers from prestack time-lapse seismic data: Geophysics, **74**, No. 2, O17–O28.

Greaves, R. J., and Fulp, T. J., 1987, Three-dimensional seismic monitoring of an enhanced oil recovery process: Geophysics, **52**, No. 9, 1175–1187.

Grossman, J. P., Popov, G., and Steinhoff, C., 2013, Integration of multicomponent time-lapse processing and interpretation: Focus on shear-wave splitting analysis: The Leading Edge, **32**, No. 1, 32–38.

Innanen, K. A., 2008, A direct nonlinear inversion of primary wave data reflecting from extended, heterogeneous media: Inverse Problems, **24**, No. 3, 1–18.

Innanen, K. A., 2013, Coupling in amplitude variation with offset and the wiggins approximation: Geophysics, **78**, No. 4, N21–N33.

Innanen, K. A., 2015, Personal comunications.

Innanen, K. A., Naghizadeh, M., and Kaplan, S. T., 2014, Perturbation methods for two special cases of the time-lapse seismic inverse problem: Geophysical Prospecting, **62**, No. 3, 453–474.

Jabbari, S., and Innanen, K. A., 2015, A theoretical analysis of linear and nonlinear shear wave time-lapse difference avo, **CSEG Expanded Abstracts**.

Jabbari, S., and Innanen, K. A., 2016, Ps and sp converted wave reflection coefficients and their application to time-lapse difference avo, **CSEG Expanded Abstracts**.

Jabbari, S., Wong, J., and Innanen, K. A., 2015, A theoretical and physical modeling analysis of the coupling between baseline elastic properties and time-lapse changes in determining difference amplitude variation with offset: Geophysics, **80**, No. 6, N37–N48.

Johnston, D. H., 1997, A tutorial on time lapse seismic reservoir monitoring: Journal of Petroleum Technology, **49**, 473475.

Johnston, D. H., 2013, Practical applications of time-lapse seismic data: Distinguished Instructor Short Course, SEG, **16**, 270.

Keys, R. G., 1989, Polarity reversals in reflections from layered media: Geophysics, **54**, No. 7, 900–905.

Lailly, P., 1983, The seismic inverse problem as a sequence of before stack migrations, *in* Conference on inverse scattering: theory and application, Society for Industrial and Applied Mathematics, Philadelphia, PA, 206–220.

Landrø, M., 2001, Discrimination between pressure and fluid saturation changes from time-lapse seismic data: Geophysics, **66**, No. 3, 836–844.

Landrø, M., 2010, Petroleum Geoscience: From Sedimentary Environments to Rock Physics., chap. 4D Seismic, Springer Science, 489–514.

Landrø, M., Solheim, O. A., Hilde, E., Ekren, B. O., and Strønen, L. K., 1999, The gullfaks 4d seismic study: Petroleum Geoscience, **5**, No. 3, 213–226.

Lumley, D. E., 2001, Time-lapse seismic reservoir monitoring: Geophysics, **66**, No. 1, 50–53.

Mahmoudian, F., 2013, Physical modeling and analysis of seismic data from a simulated fractured medium: Ph.D. thesis, University of Calgary.

Matson, K., 1996, The relationship between scattering theory and the primaries and multiples of reflection seismic data: Journal of Seismic Exploration, **5**, No. 1, 63–78.

Morse, P. M., and H, F., 1953, Methods of theoretical physics, vol. I: McGraw-Hill.

Moses, H., 1956, Calculation of the scattering potential from reflection coefficients: Physical Review, **102**, No. 2, 559.

Nguyen, P. K., Nam, M. J., and Park, C., 2015, A review on time-lapse seismic data processing and interpretation: Geosciences Journal, **19**, No. 2, 375–392.

Oldham, R. D., 1906, The constitution of the interior of the earth, as revealed by earthquakes: Quarterly Journal of the Geological Society, **62**, No. 1-4, 456–475.

Purnell, G., 1986, Observations of wave velocity and attenuation in two-phase media: Geophysics, **51**, No. 12, 2193–2199.

Speight, J. G., 2013, Enhanced recovery methods for heavy oil and tar sands: Elsevier.

Spratt, R., Goins, N., and Fitch, T., 1993, Pseudo-shearthe analysis of avo: Investigation in Geophysics Series, **8**, 37–56.

Steinhoff, C., 2013, Multicomponent seismic monitoring of the effective stimulated volume associated with hydraulic fracture stimulations in a shale reservoir, Pouce Coupe Field, Alberta, Canada: M.Sc. thesis, Colorado School of Mines.

Stewart, R. R., Gaiser, J. E., Brown, R. J., and Lawton, D. C., 2002, Converted-wave seismic exploration: Methods: Geophysics, **67**, No. 5, 1348–1363.

Stewart, R. R., Gaiser, J. E., Brown, R. J., and Lawton, D. C., 2003, Converted-wave seismic exploration: Applications: Geophysics, **68**, No. 1, 40–57.

Stolt, R. H., and Weglein, A. B., 2012, Seismic imaging and inversion: Volume 1: Application of linear inverse theory, vol. 1: Cambridge University Press.

Tarantola, A., 1984, Inversion of seismic reflection data in the acoustic approximation: Geophysics, **49**, No. 8, 1259–1266.

Thore, P., and Hubans, C., 2012, 4d seismic-to-well tying, a key step towards 4d inversion: Geophysics, **77**, No. 6, R227–R238.

Trani, M., Arts, R., Leeuwenburgh, O., and Brouwer, J., 2011, Estimation of changes in saturation and pressure from 4d seismic avo and time-shift analysis: Geophysics, **76**, No. 2, C1–C17.

Tura, A., 2003, Time-lapse seismic: Are we there yet?: SEG Technical Program Expanded Abstracts, 2395–2398.

Tura, A., and Lumley, D. E., 1998, Subsurface fluid flow properties from time-lapse elastic wave reflection data, *in* SPIE's International Symposium on Optical Science, Engineering, and Instrumentation, International Society for Optics and Photonics, 125–138.

Vedanti, N., Pathak, A., Srivastava, R., and Dimri, V., 2009, Time lapse (4d) seismic: Some case studies: Earth Science India, **2**, 230–248.

Veire, H. H., Borgos, H. G., and Landrø, M., 2006, Stochastic inversion of pressure and saturation changes from time-lapse avo data: Geophysics, **71**, No. 5, C81–C92.

Virieux, J., and Operto, S., 2009, An overview of full-waveform inversion in exploration geophysics: Geophysics, **74**, No. 6, WCC1–WCC26.

Wandler, A., Evans, B., and Link, C., 2006, Avo as a fluid indicator: A physical modeling study: Geophysics, **72**, No. 1, C9–C17.

Weglein, A. B., 1985, The inverse scattering concept and its seismic application: Developments in geophysical exploration methods, **6**, 111–138.

Weglein, A. B., Araújo, F. V., Carvalho, P. M., Stolt, R. H., Matson, K. H., Coates, R. T., Corrigan, D., Foster, D. J., Shaw, S. A., and Zhang, H., 2002, Predicting the correct spatial location of reflectors without knowing or determining the precise medium and wave velocity: initial concept, algorithm and analytic and numerical example: Journal of Seismic Exploration, **10**, No. 4, 367–382.

Weglein, A. B., Araújo, F. V., Carvalho, P. M., Stolt, R. H., Matson, K. H., Coates, R. T., Corrigan, D., Foster, D. J., Shaw, S. A., and Zhang, H., 2003, Inverse scattering series and seismic exploration: Inverse problems, **19**, No. 6, R27–R83.

Weglein, A. B., Gasparotto, F. A., Carvalho, P. M., and Stolt, R. H., 1997, An inverse-scattering series method for attenuating multiples in seismic reflection data: Geophysics, **62**, No. 6, 1975–1989.

Weglein, A. B., Matson, K. H., Foster, D. J., Carvalho, P. M., Corrigan, D., and Shaw, S. A., 2000, Imaging and inversion at depth without a velocity model: theory, concepts and initial evaluation: Expanded Abstracts, 70th Ann. Int. Mtg., Soc. Expl. Geophys.

Williamson, P. R., Cherrett, A. J., and Sexton, P. A., 2007, A new approach to warping for quantitative time–lapse characterisation, *in* 69th EAGE Conference and Exhibition incorporating SPE EUROPEC 2007.

Wong, J., Hall, K. W., Gallant, E. V., Bertram, M. B., and Lawton, D. C., 2009, Seismic physical modeling at the university of calgary, *in* 2009 SEG Annual Meeting, Society of Exploration Geophysicists.

Yang, D., Malcolm, A., and Fehler, M., 2014, Using image warping for time-lapse image domain wavefield tomography: Geophysics, **79**, No. 3, WA141–WA151.

Yilmaz, Ö., 2001, Seismic data analysis: processing, inversion, and interpretation of seismic data, vol. 1: Society of exploration geophysicists Tulsa.

Zhang, H., 2006, Direct non-linear acoustic and elastic inversion: towards fundamentally new comprehensive and realistic target identification: Ph.D. thesis, University of Houston.